Coupled nonclassical systems for coherent backaction noise cancellation

Abstract

Since the introduction of the standard quantum limit of interferometry by C. Caves, quantum optomechanics has evolved into a high-technology research field. Quantum optomechanical position and force measurements, such as gravitational wave detection and experiments involving micromechanical oscillators are currently starting to be limited by quantum radiation pressure noise. To overcome the standard quantum limit several different quantum backaction evasion or cancellation schemes have been proposed in literature and some of them have been experimentally demonstrated.

In this thesis we investigate the experimental feasibility of a coherent quantum noise cancellation (CQNC) scheme proposed by M. Tsang and C. Caves. In this case a quantum optomechanical meter cavity limited by radiation pressure backaction noise is coupled to an ancilla cavity via a down-conversion and a beamsplitter process, leading to a cancellation of the backaction noise. If the optical coupling strengths match the optomechanical coupling strength of the oscillator to the meter cavity the radiation pressure noise will interfere destructively inside the coupled system. We provide a detailed analysis of the theoretical proposal by Tsang and Caves and examine its benefits, requirements and limitations. We investigate the case of nonideal matching conditions and calculate a set of parameters for an experimental demonstration of CQNC.

We present the first experiments towards the realization of CQNC. This includes the characterization of a two-mode squeezed light source and

coupled optical cavities which are nondegenerate in polarization. We characterize the behavior of the coupled cavities with regards to varying coupling strengths and investigate the stabilization of the coupled cavities with diffent relative detunings.

Keywords: quantum radiation pressure noise, coherent control, quantum control, nonclassical light, optomechanical cavities, coupled optical cavities

Kurzfassung

Seit der ersten Erwähnung des Standardquantenlimits durch C. Caves hat sich das Feld der Quantenoptomechanik zu einem hochtechnologischen Forschungsgebiet entwickelt. Quantenoptomechanische Orts- und Kraftmessungen, wie zum Beispiel interferometrische Gravitationswellendetektoren und Experimente mit mikromechanischen Oszillatoren werden in naher Zukunft durch Quantenstrahlungsdruckrauschen limitiert zu sein. Um das Standardquantenlimit zu unterbieten, wurden verschiedenste theoretische Verfahren entwickelt mit dem Ziel das Strahlungsdruckrauschen zu umgehen und einige davon auch experimentell gezeigt.

Diese Arbeit untersucht die experimentelle Machbarkeit eines theoretischen Vorschlags der kohärenten Quantenrauschunterdrückung (*coherent quantum noise cancellation*, CQNC) von M. Tsang und C. Caves. Hierbei wird ein optomechanischer Resonator, der durch Quantenstrahlungsdruckrauschen limitiert ist, mit einem Hilfsresonator gekoppelt. Die Kopplung geschieht hierbei durch parametrische Abwärtskonvertierung und einen Strahlteiler. Wenn die optischen Kopplungsstärken des Hilfsresonators und die optomechanische Kopplungsstärke des Hauptresonators übereinstimmen interferiert das Strahlungsdruckrauschen innerhalb des Resonators destruktiv mit der Wirkung des Hilfsresonators und ist signifikant reduziert. Wir führen eine detaillierte Analyse des theoretischen Vorschlags durch und untersuchen die Vorteile, Anforderungen und Limitierungen des Systems. Dabei betrachten wir den Fall nichtidealer Anpassung der Kopplungsstärken und

berechnen experimentelle Parameter für eine Realisierung eines CQNC-Experiments.

Dies beinhaltet die Charakterisierung einer nicht entarteten Quetschlichtquelle und die Untersuchung von gekoppelten und in der Polarisation nicht entarteten Resonatoren. Wir charakterisieren das Verhalten von gekoppelten Resonatoren auf variierende Kopplungsstärken des zentralen Spiegels und untersuchen die Stabilisierung auf unterschiedliche Punkte relativer Verstimmung der beiden gekoppelten Resonatoren zueinander.

Schlüsselwörter: Quantenstrahlungsdruckrauschen, kohärente Rauschunterdrückung, Quantenkontrolle, Nichtklassisches Licht, Optomechanische Resonatoren, gekoppelte optische Resonatoren

Contents

Constants

c	Speed of light
$\hbar$	Planck's constant
μ_0	Magnetic permeability in free space
ϵ_0	Electric permittivity in free space
k_B	Boltzmann constant

Symbols

h_i	Gravitational wave strain sensitivity
λ	Laser wavelength
L_D	Gravitational wave detector arm length
m	Mass (of mechanical oscillator)
P	Laser Power
Ω	Gravitational wave measurement frequency
$\mathbf{B}$	Magnetic field
$\mathbf{H}$	Magnetizing field
$\mathbf{E}$	Electric field
$\mathbf{D}$	Electric displacement
$\mathbf{A}$	Vector potential
ψ	Scalar potential

L	Macroscopic length
ω	Angular frequency
$\mathbf{k}$	Propagation vector of the electromagnetic field
$\hat{A}$	Generic operator
$|\phi\rangle$	Generic quantum mechanical state
ξ_{e}	Generic eigenvalue
$\hat{H}$	Hamilton operator
$\hat{a}, \hat{a}^{\dagger}$	Annihilation and creation operator
$\hat{n}$	Number operator
$\hat{x}$	Amplitude quadrature operator
$\hat{p}$	Phase quadrature operator
Δ_s	Standard deviation
$|0\rangle$	Vacuum state
$|n\rangle$	Number/Fock-state
n	Photon number
$\hat{X}(\theta_{\mathrm{q}})$	Generic quadrature operator
θ_{q}	Quadrature angle
$|\alpha\rangle$	Coherent state
$\hat{D}$	Displacement operator
$\hat{S}$	Squeeze operator
$\mathbf{r}$	Squeezing parameter
ϕ	Squeezing angle
$\chi^{(\mathrm{n})}$	n-th order susceptibility
n_{r}	Refractive index
Λ	Poling period of nonlinear crystal
$i(t)$	Photocurrent
ρ	Amplitude reflectivity
τ	Amplitude transmission
R	Power reflectivity
T	Power transmission
α, β	Coherent amplitudes
V_i	Variance of a measurement
Φ	Cavity tuning

x_{m}	Position of mechanical oscillator
γ_{m}	Mechanical linewidth
Q	Mechanical quality factor
ω_{m}	Mechanical resonance frequency
E_{zp}	Mechanical zero point energy
x_{zp}	Mechanical zero point fluctuation
g_0	Optomechanical coupling
κ_{c}	Cavity linewidth
S_{XX}^2	Noise spectral density
χ_{m}	Mechanical susceptibility
χ_{c}	Susceptibility of optical cavity
Δ	Cavity detuning
T	Temperature
Γ	Nonlinear gain parameter
d_{eff}	Nonlinear coefficient
θ_{in}	Incident angle

Abbreviations

SQL	Standard quantum limit
CQNC	Coherent quantum noise cancellation
SFG	Sum frequency generation
SHG	Second harmonic generation
PDC	Parametric down-conversion
HR-coating	High-reflective coating
AR-coating	Antireflective coating
FSR	Free spectral range
FWHM	Full width half maximum
$\mathcal{F}$	Finesse
PBS	Polarizing beamsplitter
OPO	Optical parametric oscillator
NDOPO	Nondegenerate optical paremetric oscillator
PPKTP	Periodically poled potassium titanyl phosphate
NPRO	Nonplanar ring oscillator

CAD   Computer-aided drafting

Introduction

1.1 Foundations of optomechanics

In recent years optomechanic interactions and in particular quantum optomechanics has become a very popular scientific topic. Since the first suggestions of the by Kepler who wondered why comet tails always point away from the sun ('The direct rays of the Sun strike upon it' [1]) optomechanic interactions have evolved into a high-technology research field.

The first classical description of radiation pressure was performed by Maxwell in 1973 [2] as a consequence of his electromagnetic description of light [3] and can be understood as the first theoretical calculation of optomechanical interaction. A thermodynamical description resulting from energy conservation laws in Doppler effects was presented shortly afterwards by Bartoli [4]. The results of these theoretical descriptions were experimentally demonstrated in the experiments by Lebedew in 1901 [5].

With the concept of photons his work on the photoelectric effect shown in 1887 by Hertz [6] Einstein set the basis for a quantum mechanical description of these effects [7]. For optomechanical interactions pho-

tons should have a momentum, which could be translated to particles in elastic scarttering processes. This theory was doubted by many scientists until Compton showed the effect of quantized momentum in 1922 with his experiments on scattered electrons under the influence of x-ray photons [8, 9].

With the first demonstration of laser light in 1960 by Maiman [10] light sources with unprecedented power density and spectral purity became available. Ashkin demonstrated radiation pressure effects of laser light on small latex spheres in 1970 [11] and built the foundation for magneto-optical atom cooling which was demonstrated by Hänsch and Schawlow in 1975 [12] and atom trapping which was first demonstrated in 1980 by Ashkin and Dziedzic [13].

In parallel with the rise of lasers Gertsenshtein suggested laser interferometers for the detection of gravtiational waves [14] which were predicted by Einstein's theory of general relativity [15, 16]. In the early 1970s Thorne, Drever and Weiss calculated the sensitivity of laser interferometric gravitational wave detectors [17] and first experiments demonstrated the already high sensitivity of such instruments [18]. Braginsky and Caves calculated the fundamental limits of the sensitivity of laser interferometric gravtiational wave detectors in the late 1970s [19, 20] and raised the topic of quantum radiation pressure noise limiting the sensitivity of the detectors.

Since the turn of the millenium the topic of experimental optomechanics has evolved into a field of broad and highly active research. Besides applications in gravitational wave detection, optomechanical oscillators are candidates for quantum memory in quantum computing [21] or transducers between optical and microwave frequencies [22]. Quantum optomechanical experiments have been done with oscillators with masses from the kg-scale down to light-atom interactions. An overview of these is given in [23].

The first experimental measurements of radiation pressure quantum noise were independently conducted by Purdy *et al.* and Painter *et al.* in 2012 with two different experimental setups using micromechanical oscillators [24, 25]. Also, the second generation of gravitational wave

(a) ALIGO sensitivity [26]

(b) Displacement spectrum measurements [24]
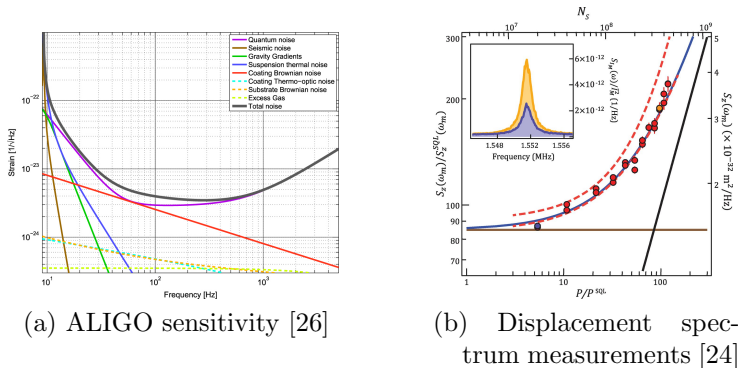
FIGURE 1.1: Radiation pressure noise limited experiments. (a) The calculated sensitivity of the advanced LIGO gravitational wave detector. In the frequency regime from 10 to 50 Hz the detector is limited by radiation pressure noise. (b) Displacement spectrum measurement by Purdy *et al.*: for increased light power the measurement shows an increased noise as a result of radiation pressure noise.

detectors, Advanced LIGO and Advanced VIRGO, will be limited by quantum radiation pressure noise in the low frequency range of their detection band [26, 27].

1.1.1 Quantum limits in optomechanical measurements

When all technical noise sources can be neglected every interferometric position or force measurement has a fundamental limit in sensitivity. This so called *standard quantum limit* (SQL) of laser interferometry arises from the quantum nature of light and the consequence of the Heisenberg limit [28]. The SQL is formed by two contributions, *quantum shot noise* and *quantum radiation pressure noise*, acting on the optomechanical measuring device. We give a brief introduction into the formulation of the SQL using the example of a laser interferometric gravitational wave detector. A detailed calculation of the SQL is presented in Sec. 6.1.

(a) Original photograph   (b) Darkened photograph with shot
                                  noise
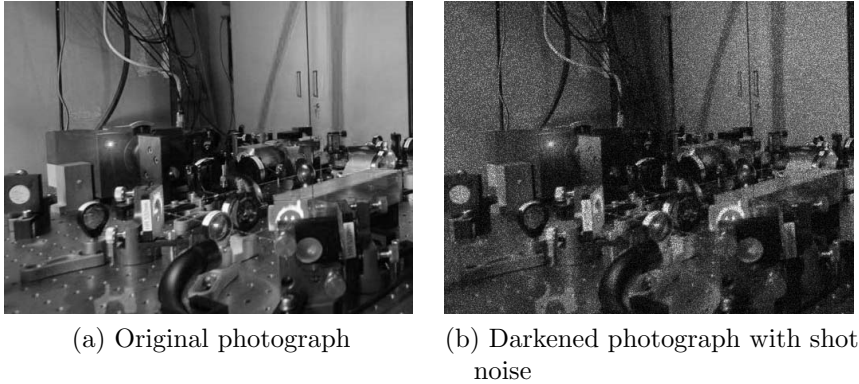
FIGURE 1.2: Shotnoise in photography. (a) the original photograph with suf-
ficient light. (b) With insufficient light the camera experiences shot noise in
the darker areas. This picture shows a snapshot of one of our optical tables.

Shot noise

The photon distribution of laser light at a detector is not constant but
fluctuates following a Poissonian statistic [29]. The fluctuations around
the median photon number n are given by $\Delta n = \sqrt{n}$. These fluctua-
tions are called photon shot noise, the same effect that is also observ-
able for photos taken with low light levels and long illumination times
(see Fig. 1.2). For the strain sensitivity of a gravitational wave detector
this noise contribution is given by [20]

$$h_{\text{shot}}(\Omega) = \frac{1}{L_{\text{D}}} \sqrt{\frac{\hbar c \lambda}{2\pi P}}, \tag{1.1}$$

where L_{D} is the detector armlength, λ the wavelength of the laser and
P the circulating light power. $\hbar$ is Planck's constant and c the speed of
light. We see that shot noise is a white noise process independent of
the measurement frequency Ω. The reduced noise contribution for the
interferometer strain sensitivity can be explained with the linear depen-
dency of the strain to the power [20]. As shot noise increases with the
square root of the power the relative shot noise contribution is reduced
with increased input power to the gravitational wave detector.

Radiation pressure noise

With increased power inside the interferometer, quantum radiation pressure noise will become a dominant noise source limiting the sensitivity of the measurement. The end mirrors of a gravitational wave detector are suspended pendula which are affected by radiation pressure forces. The amplitude noise of a light field changes the position of the endmirror which imprints phase changes on the light field via backaction of the restoring force towards the equilibrium of position of the pendulum. This noise contribution to the strain amplitude is given by [20]

$$h_{\mathrm{rpn}}(\Omega) = \frac{1}{2m\Omega^2 L_{\mathrm{D}}} \sqrt{\frac{8\pi\hbar P}{c\lambda}}, \tag{1.2}$$

where m is the mirror mass. The radiation pressure noise increases with increased light power P. This noise is not white in frequency because it depends on the noise transfer function of the pendulum. The noise is reduced with increasing frequency following a $1/\Omega^2$ characteristic and will limit the sensitivity in the low-to-medium frequency band of the detector.

Standard quantum limit

The total quantum noise of a gravitational wave detector is the root of the quadratic sum of shot noise and radiation pressure noise

$$h_{\mathrm{tot}} = \sqrt{h_{\mathrm{shot}}^2(\Omega) + h_{\mathrm{rpn}}^2(\Omega)} \tag{1.3}$$

When the quantum noise is minimized with respect to an optimal power for a certain measurement frequency such that

$$P_{\mathrm{opt}} = \frac{c\lambda m\Omega^2}{4\pi}, \tag{1.4}$$

we can find the SQL of interferometry as

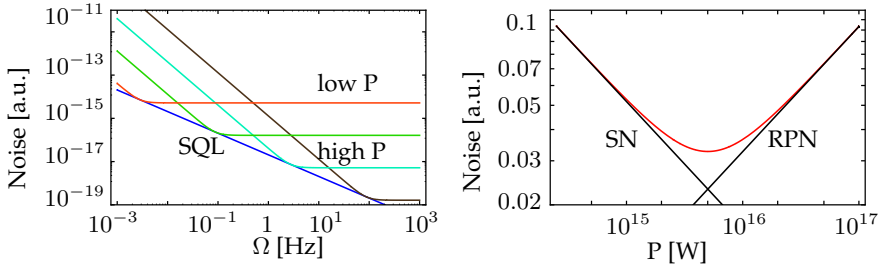$$h_{\mathrm{sql}} = \sqrt{\frac{4\hbar}{m\Omega^2 L^2}}. \tag{1.5}$$

FIGURE 1.3: Different ways to display the standard quantum limit of position and force measurements. (a) noise spectral density of an interferometric position measurement. We show the root of the quadratic sum of radiation pressure noise and shot noise for different power levels. Higher powers increase the radiation pressure noise and decrease the shot noise contribution. The standard quantum limit (blue line) is the set of all points where quantum shot noise and quantum radiation pressure noise have equal contribution to the noise at a given power. (b) noise density at a given measurement frequency as a function of light power: The minimum of the noise curve is reached for the optimal power when both uncorrelated noise curves add up equally.

The SQL can be displayed in two ways (see Fig. 1.3). The standard way in the gravitational wave community is the strain sensitivity as a function of the frequency. Here the SQL is the set of all points with optimal power at any given measurement frequency. The other plot is commonly used in quantum mechanical force measurements where one looks at one measurement frequency and plots the sensitivity as a function of power. Here we see that the relative shot noise decreases towards an optimal power at maximum sensitivity until radiation pressure noise effects take over and become the limiting noise source.

1.1.2 Techniques for backaction evasion

The experimental measurement of quantum radiation pressure noise has underlined that quantum noise will be limiting future measurements in gravitational wave detection and micromechanical position and force measurements. In recent decades various schemes have been proposed to overcome the SQL of interferometry. Without claiming completeness we mention frequency-dependent squeezed light input

[30], variational readout of the interferometer output [31, 32], Kerr media inside the detectors [33, 34] and the use of dual mechanical resonators or optical springs [35, 36, 37]. Another solution to overcome the SQL of interferometry is proposed by the use of speed meters [38, 39] which have a reduced quantum noise limit compared to the quantum noise of a Michelson interferometer. Some of the proposed schemes have been experimentally demonstrated [40, 41, 42] while others are still under investigation.

Another backaction evasion scheme based on a different principle was proposed by M.Tsang and C. Caves [43]. Here the coherent cancellation of backaction noise called *coherent quantum noise cancellation* (CQNC) is proposed. In contrast to other backaction-evading techniques this scheme destructively interferes the backaction noise with the use of an *antinoise* path within the detecting instrument. An analogous idea has been proposed for atomic spin measurements [44, 45] which has been demonstrated experimentally [46].

1.2 Structure of the thesis

This thesis concentrates on the experimental realization of the CQNC scheme proposed by Tsang and Caves [43]. We investigate the theoretical scheme under realistic assumptions and nonideal conditions and show the first experiments which have been done for the realization of CQNC.

For the theoretical background of our calculations for CQNC we give an introduction of the quantum mechanical description of light fields and their corresponding quantum states in Chapter 2.

Nonlinear optical effects inside optical cavities are a core element of the experiments in the experimental part. Therefore we discuss the generation and detection of squeezed light fields in Chapter 3 and describe optical cavities in Chapter 4. An introduction to optomechanical resonators and their quantum mechanical behavior is given in Chapter 5. With the theoretical background from the first chapters we recapitulate

the results from the proposal by Tsang and Caves and expand the description to mismatches from the ideal cancellation case. At the end of the chapter a set of possible experimental parameters is given. This work was published in Phys. Rev. A [64].

In Chapter 7 we present the experiments as the first steps towards the realization of CQNC. This includes the characterization of a two-mode squeezed light source and two polarization nondegenerate coupled cavities.

Chapter 8 gives some general conclusions and an outlook towards future experiments in the area of CQNC.

CHAPTER 2

Quantum mechanics of light

Planck's description of black body radiation in 1900 [47] bridged the gap between observations of the light spectrum of the sun and the classic theoretical description of light, thereby laying the foundations of quantum mechanics. In 1905 Einstein introduced the concept of the photon with his work on the photoelectric effect [7], which led to the considerations about quantum mechanical absorption and the stimulated emission of light in 1917 [48]. The concept of laser light is based on the stimulated emission of photons amplified with an optical resonator and was first demonstrated by Maiman in 1960 [10]. The quantum mechanical description of the coherent fields which are emitted by a laser was developed by Glauber in 1963 [49].

Lasers and their quantum mechanical effects have been developed into a basic and ubiquitous tool for modern quantum optical experiments. The effects we calculate and measure in this thesis make use of the coherent field and the quantum mechanical interactions with nonlinear media. Therefore we want to develop a theoretical description of light and its quantization in this chapter. With this we will introduce the concept of the vacuum state coherent fields and squeezed states. We follow the approach from [50] and [51] to develop a consistent nomenclature for

this thesis.

2.1 Electromagnetic fields

We start our description with Maxwell's equations [3] in free space

$$\nabla \mathbf{B} = 0, \qquad \nabla \times \mathbf{E} = -\frac{\partial \mathbf{B}}{\partial t}$$

$$\nabla \mathbf{D} = 0, \qquad \nabla \times \mathbf{H} = \frac{\partial \mathbf{D}}{\partial t}$$

where the magnetic field $\mathbf{B} = \mu_0 \mathbf{H}$ depends on the magnetizing field $\mathbf{H}$, and the electric displacement $\mathbf{D} = \epsilon_0 \mathbf{E}$, with the electric field $\mathbf{E}$. μ_0 and ϵ_0 are the magnetic permeability and the electric permittivity of free space which are related to the speed of light c via $\epsilon_0 \mu_0 = 1/c^2$. We can use these expressions to form the electromagnetic wave equation

$$\nabla^2 \mathbf{E} + \frac{1}{c^2}\frac{\partial^2}{\partial t^2}\mathbf{E} = -\mu_0 \frac{\partial^2}{\partial t^2}\mathbf{B} \tag{2.1}$$

2.1.1 Mode functions of the electromagnetic field

The quantization of physical systems is introduced in most quantum mechanics textbooks with the quantization of the harmonic oscillator such as the hydrogen atom [52, 53]. To follow this notation we formulate the electromagnetic field in mode functions inside a fixed volume with side length L. First we substitute $\mathbf{E}$ and $\mathbf{B}$ with the vector and scalar potentials $\mathbf{A}$ and ψ in free space using the Coulomb gauge $\nabla \mathbf{A} = 0, \psi = 0$ [50]

$$\mathbf{B} = \nabla \times \mathbf{A}, \tag{2.2}$$

$$\mathbf{E} = -\frac{\partial \mathbf{A}}{\partial t}. \tag{2.3}$$

The wave equation Eq. (2.1) then becomes

$$\nabla^2 \mathbf{A}(\mathbf{r},t) = \frac{1}{c^2}\frac{\partial^2 \mathbf{A}(\mathbf{r},t)}{\partial t^2}. \tag{2.4}$$

We do not know the exact form of the vector potential $\mathbf{A}$ so we expand the description with a general set of orthonormal vector modes which still fulfill the wave equation

$$\mathbf{A}(\mathbf{r},t) = \sum_k c_k \mathbf{u}_k(\mathbf{r}) e^{i\omega_k t} + \; c.c. \tag{2.5}$$

$\mathbf{u}_k(\mathbf{r})$ corresponds to the frequency ω_k and satisfies the wave equation and the Coulomb gauge. Within a fixed volume we consider periodic boundary conditions leading to a form of plane wave mode functions which can be written as

$$\mathbf{u}_k(\mathbf{r}) = \sqrt{\frac{1}{L^3}} \mathbf{e}_\xi e^{i\mathbf{kr}}, \tag{2.6}$$

with $\mathbf{e}_\xi$ being the polarization vector for the two polarizations $\lambda = 1,2$

$$\mathbf{k}\mathbf{e}_\xi = 0, \qquad \mathbf{e}_\lambda \cdot \mathbf{e}_{\lambda'} = \delta_{\lambda\lambda'}, \tag{2.7}$$

which are perpendicular to the propagation vector

$$\mathbf{k} = \frac{2\pi}{L}(n_x,n_y,n_z) \tag{2.8}$$

$$n_{x,y,z} = 0, \pm 1, \pm 2, \dots \tag{2.9}$$

The frequency of the individual mode is related to $\mathbf{k}$ by the dispersion relation

$$\omega_k = c|\mathbf{k}|. \tag{2.10}$$

Now we can write the vector potential in mode functions using the normalized dimensionless amplitudes $a_k = \sqrt{2\omega_\mathbf{k}\epsilon_0/\hbar}c_\mathbf{k}$ and their hermitian conjugates $a_k^\dagger$

$$\mathbf{A}(\mathbf{r},t) = \sum_k \sqrt{\frac{\hbar}{2\omega_k\epsilon_0}} \cdot (a_k\mathbf{u}_k(\mathbf{r})e^{-i\omega_k t} + a_k^\dagger \mathbf{u}_k^*(\mathbf{r})e^{i\omega_k t}). \tag{2.11}$$

Inserting Eq. (2.11) into Eq. (2.3) the electric field takes the corresponding form

$$\mathbf{E}(\mathbf{r},t) = i \sum_k \sqrt{\frac{\hbar\omega_k}{2\epsilon_0}} \cdot (a_k \mathbf{u}_k(\mathbf{r}) e^{-i\omega_k t} + a_k^\dagger \mathbf{u}_k^*(\mathbf{r}) e^{i\omega_k t}). \qquad (2.12)$$

Now that we have developed a multimode description for the electromagnetic field we can consider it as a harmonic oscillator in the fixed volume L. This enables us to perform the quantization of the harmonic oscillator for a quantum mechanical description of the electromagnetic field.

2.2 Quantization of the electromagnetic field

For the canonical quantization we use the Hamiltonian of the electromagnetic field [51]

$$H = \int \left(\frac{\epsilon_0 \mathbf{E}(\mathbf{r},t)^2}{2} + \frac{\mathbf{B}(\mathbf{r},t)^2}{2\mu_0} \right) d^3\mathbf{r} \qquad (2.13)$$

$$= \left(P^2 + \omega_k^2 Q^2 \right), \qquad (2.14)$$

with the canonical position Q and momentum $P = \dot{Q}$.

In the case of electromagnetic fields we replace the canonical position and momentum with operators $\hat{Q}$ and $\hat{P}$, for which the conditions

$$[\hat{Q},\hat{P}] = i\hbar \qquad (2.15)$$

$$[\hat{Q},\hat{Q}] = [\hat{P},\hat{P}] = 0. \qquad (2.16)$$

are valid. Here we used the commutator [50]

$$[\hat{A},\hat{B}] = \hat{A}\hat{B} - \hat{B}\hat{A}. \qquad (2.17)$$

which is commonly used in quantum mechanics to classify the measurement $\hat{A}|\psi\rangle = \xi|\psi\rangle$ of a state $|\psi\rangle$ with eigenvalue ξ_e. If the commutator of two operators is vanishing $[\hat{A},\hat{B}] = 0$ they are called commuting operators and share the same eigenvalue ξ_e. If the commutator is nonvanishing the operators are called noncommuting and the mea-

surements yields two orthogonal characteristics of the state $|\psi\rangle$.
Continuing with the quantization we define the dimensionless creation
and annihilation operators as corresponding to the dimensionless con-
stants a and $a^\dagger$ from Eq. (2.12)

$$\hat{a}_k = \frac{1}{\sqrt{2\hbar\omega_k}}(\omega_k\hat{Q} + i\hat{P}) \tag{2.18}$$

$$\hat{a}_k^\dagger = \frac{1}{\sqrt{2\hbar\omega_k}}(\omega_k\hat{Q} - i\hat{P}). \tag{2.19}$$

which satisfy the commutation relation

$$[\hat{a},\hat{a}^\dagger] = \hat{a}\hat{a}^\dagger - \hat{a}^\dagger\hat{a} = 1. \tag{2.20}$$

We substitute **E** and **B** using the Coulomb gauge Eq. (2.2) and the de-
scription for the vector potential and the E-field (Eq. (2.11), Eq. (2.12)).
The Hamiltonian then becomes

$$\hat{H} = \sum_k \frac{\hbar\omega_k}{2}\left(\hat{a}_k^\dagger\hat{a}_k + \hat{a}_k\hat{a}_k^\dagger\right) = \sum_k \hbar\omega_k\left(\hat{a}_k^\dagger\hat{a}_k + \frac{1}{2}\right). \tag{2.21}$$

Light emitted by a monochromatic laser source is a directed single beam.
Therefore it can be described adequately by the one-dimensional quan-
tum mechanical description of the electromagnetic field. Therefore we
reduce the Hamiltonian to a single-mode, one-dimensional description
[51]

$$\hat{H} = \hbar\omega\left(\hat{a}^\dagger\hat{a} + \frac{1}{2}\right). \tag{2.22}$$

For the description of the measurement of electromagnetic fields we in-
troduce the dimensionless quadrature operators $\hat{x}$ (amplitude quadra-
ture) and $\hat{p}$ (phase quadrature) which represent the amplitude and phase
of the electromagnetic field

$$\hat{x} = \frac{1}{\sqrt{2}}(\hat{a}^\dagger + \hat{a}) \tag{2.23}$$

$$\hat{p} = \frac{i}{\sqrt{2}}(\hat{a}^\dagger - \hat{a}). \tag{2.24}$$

The amplitude and phase quadratures are hermitian and therefore two observable quantities. These quantities are used for the characterization of squeezed light fields (see Sec. 3.1). They are noncommuting variables, satisfying

$$[\hat{x},\hat{p}] = i. \tag{2.25}$$

We introduce Heisenberg's uncertainty relation, which states, that two noncommuting variables $[\hat{A},\hat{B}] = \hat{C} \neq 0$ cannot be measured simultaneously with infinite precision for both measurements [28]. The precision of the simultaneous measurement is restricted by the product of the standard deviations of the individual measurements

$$\Delta_s \hat{A} \cdot \Delta_s B \geq \frac{1}{2}|\langle \hat{C} \rangle|, \tag{2.26}$$

where the expectation value $\langle \hat{A} \rangle = \langle n|\hat{A}|n \rangle$, and the definition of the standard deviation is

$$\Delta_s \hat{A} = \sqrt{\langle \hat{A}^2 \rangle - \langle \hat{A} \rangle^2}. \tag{2.27}$$

Following this we find that the accuracy of the simultaneous measurement of phase and amplitude is limited by

$$\Delta_s \hat{x} \cdot \Delta_s \hat{p} \geq \frac{1}{2}. \tag{2.28}$$

2.2.1 Eigenstates of the quantized field

To evaluate the quantized energy levels of the single-mode field we define an energy eigenstate $|n\rangle$ with the eigenvalue E_n

$$\hat{H}|n\rangle = \hbar\omega \left(\hat{a}^\dagger \hat{a} + \frac{1}{2} \right) |n\rangle = E_n|n\rangle. \tag{2.29}$$

$|n\rangle$ is called the *number state* or *Fock-state*. To examine the effect of the creation operator on this state, we let $\hat{a}^\dagger$ act on Eq. (2.29) from the left-

hand side and get the following result using Eq. (2.20)

$$
\begin{aligned}
\hat{H}(\hat{a}^\dagger|n\rangle) &= \hbar\omega\left(\hat{a}^\dagger\hat{a} + \frac{1}{2}\right)(\hat{a}^\dagger|n\rangle) \\
&= \hbar\omega\left((\hat{a}^\dagger\hat{a}\hat{a}^\dagger - \hat{a}^\dagger) + \frac{1}{2}\hat{a}^\dagger\right)|n\rangle \\
&= (E_n + \hbar\omega)(\hat{a}^\dagger|n\rangle).
\end{aligned}
\tag{2.30}
$$

The energy eigenvalue for the eigenstate $(\hat{a}^\dagger|n\rangle)$ is $E_n + \hbar\omega$ and one can see directly that $\hat{a}^\dagger$ creates an energy quantum $\hbar\omega$ which we call photon. The opposite result is obtained with the annihilation operator $\hat{a}$ which destroys a photon. The eigenenergies of the harmonic oscillator must always be positive $E_0 > 0$. With this in mind we must reach a state of minimal energy, the vacuum state $|0\rangle$, by repeated use of the annihilation operator on the eigenstates of the harmonic oscillator such that

$$
\hat{H}(\hat{a}|0\rangle) = (E_0 - \hbar\omega)(\hat{a}|0\rangle) = 0.
\tag{2.31}
$$

This is only possible when $\hat{a}|0\rangle = 0$ and the eigenvalue problem formulates as

$$
\hat{H}|0\rangle = \hbar\omega\left(\hat{a}^\dagger\hat{a} + \frac{1}{2}\right)|0\rangle = \frac{1}{2}\hbar\omega|0\rangle,
\tag{2.32}
$$

which gives the zero-point energy $E_0 = \hbar\omega/2$. All higher energy levels of the harmonic oscillator are defined from this level via

$$
E_n = \hbar\omega\left(n + \frac{1}{2}\right), n \in \mathbb{N}.
\tag{2.33}
$$

It is convenient to define the number operator $\hat{n} = \hat{a}^\dagger\hat{a}$ whose eigenvalues are the number of photons of a given number state

$$
\hat{n}|n\rangle = n|n\rangle.
\tag{2.34}
$$

As the number state must be normalized $\langle n|n\rangle = 1$ we determine the effect of $\hat{a}$ and $\hat{a}^\dagger$ on the number state

$$
\hat{a}|n\rangle = \sqrt{n}|n-1\rangle
\tag{2.35}
$$

$$
\hat{a}^\dagger|n\rangle = \sqrt{n-1}|n+1\rangle.
\tag{2.36}
$$

With the tools obtained we can now express an arbitrary state in the orthonormal basis of Fock states $|n\rangle$, by use of the creation $\hat{a}^\dagger$, annihilation $\hat{a}$ and number operator $\hat{n}$.

2.3 Quantum states of light

2.3.1 Vacuum state

We have introduced the vacuum $|0\rangle$ state from which we can create an arbitrary Fock-state using the creation operator. If we consider a generic quadrature using the quadrature operators from Eq. (2.23)

$$\hat{X}(\theta_{\mathrm{q}}) = \frac{1}{2}\left(\hat{a}e^{-i\theta_{\mathrm{q}}} + \hat{a}^\dagger e^{i\theta_{\mathrm{q}}}\right) = \hat{x}\cos\theta_{\mathrm{q}} + \hat{p}\sin\theta, \qquad (2.37)$$

the expectation value for any Fock-state vanishes

$$\langle n|\hat{X}(\theta)|n\rangle = 0. \qquad (2.38)$$

The variance of the squared operators however gives a fluctuation contribution to the standard deviation

$$\langle n|\hat{X}^2(\theta)|n\rangle = \frac{1}{4}(2n+1). \qquad (2.39)$$

The vacuum state is called a minimum uncertainty state as the uncertainty product in Eq. (2.26) of the two orthogonal quadratures with $\theta_{\mathrm{q1}} = \theta_{\mathrm{q2}} + \pi/2$ is minimized for $n = 0$.

2.3.2 Coherent states

The description of quantized fields in the Fock-basis has many advantages when considering single photon experiments and the associated quantum effects. In our experiments we are using continuous-wave laser light which has a nonvanishing expectation value in the amplitude and phase quadrature which we know from the classical description of laser light which sees sinusoidal oscillations in time at a fixed point in space [51]. Therefore it is not sufficient to just increase the

photon number of a Fock-state to generate coherent light fields (see Eq. (2.38)). We must expand our description from Sec. 2.2.1 with the concept of coherent states which was introduced by Roy Glauber in 1963 [49]. We assume the existence of a state $|\alpha\rangle$ which has a nonvanishing expectation value for the annihilation operator and fulfills the eigenvalue equation

$$\hat{a}|\alpha\rangle = \alpha|\alpha\rangle. \tag{2.40}$$

We stated earlier that the basis of Fock-states is complete. It is therefore possible to find a superposition of Fock-states which describes any coherent state $|\alpha\rangle$

$$|\alpha\rangle = \sum_{n=0}^{\infty} C_n |n\rangle. \tag{2.41}$$

The eigenvalue α is calculated by applying $\hat{a}$ on both sides of Eq. (2.41)

$$\hat{a}|\alpha\rangle = \sum_{n=1}^{\infty} C_n \sqrt{n}|n-1\rangle = \alpha \sum_{n=0}^{\infty} C_n |n\rangle. \tag{2.42}$$

We equate the coefficients of $|n\rangle$ and obtain

$$C_n \sqrt{n} = \alpha C_{n-1} \tag{2.43}$$

which, after dividing by $\sqrt{n}$, leads to

$$C_n = \frac{\alpha}{\sqrt{n}} C_{n-1} = \frac{\alpha^2}{\sqrt{n(n-1)}} C_{n-2} = \cdots = \frac{\alpha^n}{\sqrt{n!}} C_0. \tag{2.44}$$

Now we can write $|\alpha\rangle$ as

$$|\alpha\rangle = C_0 \sum_{n=0}^{\infty} \frac{\alpha^n}{\sqrt{n!}} |n\rangle. \tag{2.45}$$

We calculate the value of C_0 by normalization of $|\alpha\rangle$

$$\langle\alpha|\alpha\rangle = 1 = |C_0|^2 \sum_{n=0}^{\infty} \frac{|\alpha|^2}{n!} = |C_0|^2 e^{|\alpha|^2}. \tag{2.46}$$

Inserting this into Eq. (2.44), the coherent state yields

$$|\alpha\rangle = e^{-\frac{1}{2}|\alpha|^2} \sum_{n=0}^{\infty} \frac{\alpha^n}{\sqrt{n!}} |n\rangle. \tag{2.47}$$

We know that an arbitrary Fock-state can be generated from the creation operator acting on the vacuum state. We use this to get an operator $\hat{D}$ which is able to generate coherent states from the vacuum state. We expand Eq. (2.47) to

$$|\alpha\rangle = e^{-\frac{1}{2}|\alpha|^2} \sum_{n=0}^{\infty} \frac{\alpha^n}{n!} (\hat{a}^{\dagger})^n |0\rangle \tag{2.48}$$

$$= e^{-\frac{1}{2}|\alpha|^2} e^{-\alpha^* \hat{a}} \sum_{n=0}^{\infty} \frac{\alpha^n}{n!} (\hat{a}^{\dagger})^n |0\rangle, \tag{2.49}$$

since $e^{-\alpha^* \hat{a}} |0\rangle = |0\rangle$. If we write the sum in its exponential form we can reduce this equation to

$$
\begin{aligned}
|\alpha\rangle &= e^{-\frac{1}{2}|\alpha|^2} e^{-\alpha^* \hat{a}} e^{\alpha \hat{a}^{\dagger}} |0\rangle \\
&= e^{\alpha \hat{a}^{\dagger} - \alpha^* \hat{a}} |0\rangle \\
&= \hat{D} |0\rangle
\end{aligned}
\tag{2.50}
$$

where we used the theorem for the multiplication of exponential functions of operators which states that $e^{\hat{A}} e^{\hat{B}} = e^{(\hat{A} + \hat{B} + \frac{1}{2}[\hat{A}, \hat{B}])}$ [52]. Eq. (2.50) gives the expression for the *displacement operator* $\hat{D}$ which acts on the vacuum state to generate an arbitrary coherent state.

The displacement operator only adds a coherent amplitude α to a given vacuum state. The fluctuations of phase and amplitude quadrature of any coherent state $|\alpha\rangle$ are the same as they are for the vacuum state

$$\langle \hat{x} \rangle_{\alpha} = \frac{1}{4} = \langle \hat{p}^2 \rangle_{\alpha}. \tag{2.51}$$

Finally we must clarify the meaning of the complex eigenvalue α. To do this we look at the expectation value of the number operator

$$n = \langle \alpha | \hat{n} | \alpha \rangle = |\alpha|^2, \tag{2.52}$$

which is the mean photon number of the coherent state $|\alpha\rangle$. This photon number fluctuates with

$$\Delta_s \hat{n} = \sqrt{\langle \hat{n}^2 \rangle - \langle \hat{n} \rangle^2} = \sqrt{n} \tag{2.53}$$

which means that photon counting noise has the characteristics of a Poissonian process; this is called *shot noise*.

2.3.3 Squeezed states

Although the Heisenberg uncertainty relation places a limit on the precision of the simultaneous measurement of the phase and amplitude quadratures we are able to prepare a state $|s\rangle$ for which the generic quadrature operator from Eq. (2.37) has an angle θ_{q0} which satisfies

$$\langle \Delta_s \hat{X}(\theta_{q0}) \rangle < \frac{1}{4}. \tag{2.54}$$

This state is called a *squeezed state* [54]. To satisfy the Heisenberg uncertainty relation the orthogonal quadrature must have an increased uncertainty and is called *antisqueezed*. To generate squeezed states mathematically we introduce the *squeeze operator*

$$\hat{S}(\xi) = e^{\frac{1}{2}(\xi^* \hat{a}\hat{a} - \xi \hat{a}^\dagger \hat{a}^\dagger)}, \tag{2.55}$$

where $\xi = re^{i\phi}$. The amount of squeezing is set by the squeezing parameter r with $0 \leq r < \infty$. The squeezing angle $0 \leq \phi \leq 2\pi$ defines the quadrature that is squeezed. This becomes evident when applying $\hat{S}(\xi)$ to the vacuum state and calculating the variance for the amplitude

and phase quadratures

$$
\begin{aligned}
\langle \hat{x}^2 \rangle_{\xi 0} &= \langle 0|\hat{S}^\dagger(\xi)\hat{x}^2\hat{S}(\xi)|0\rangle \\
&= \frac{1}{4}\left[\cosh^2(r) + \sinh^2(r) - 2\sinh(r)\cosh(r)\cos(\phi)\right] \\
&= \frac{1}{4}\left[\cos^2\left(\frac{\phi}{2}\right)e^{2r} + \sin^2\left(\frac{\phi}{2}\right)e^{-2r}\right] \quad (2.56) \\
\langle \hat{p}^2 \rangle_{\xi 0} &= \langle 0|\hat{S}^\dagger(\xi)\hat{p}^2\hat{S}(\xi)|0\rangle \\
&= \frac{1}{4}\left[\cosh^2(r) + \sinh^2(r) + 2\sinh(r)\cosh(r)\cos(\phi)\right] \\
&= \frac{1}{4}\left[\sin^2\left(\frac{\phi}{2}\right)e^{2r} + \cos^2\left(\frac{\phi}{2}\right)e^{-2r}\right]. \quad (2.57)
\end{aligned}
$$

For $\phi = 0$ we get

$$
\langle \hat{x}^2 \rangle_{\xi,0} = \frac{1}{4}e^{-2r} \quad (2.58)
$$

$$
\langle \hat{p}^2 \rangle_{\xi,0} = \frac{1}{4}e^{2r} \quad (2.59)
$$

which results in a reduced variance in the amplitude quadrature, now referred to as *amplitude squeezing*. For $\phi = \pi$ the squeezing angle is rotated such that the state is squeezed in phase (*phase squeezing*). In the lossless case we have pure squeezed states, and the uncertainty product of the squeezed and antisqueezed quadrature is still minimal.

Squeezing is not limited to amplitude and phase quadrature. We introduce rotated quadrature operators which enable different choices for the angle ϕ

$$
\begin{pmatrix} \hat{Y}_1 \\ \hat{Y}_2 \end{pmatrix} = \begin{pmatrix} \cos(\phi/2) & \sin(\phi/2) \\ -\sin(\phi/2) & \cos(\phi/2) \end{pmatrix} \begin{pmatrix} \hat{x} \\ \hat{p} \end{pmatrix}. \quad (2.60)
$$

For a given angle ϕ we can always find a set of two orthogonal operators for which

$$
\langle \hat{Y}_1^2 \rangle_\xi = \frac{1}{4}e^{-2r}, \quad (2.61)
$$

$$
\langle \hat{Y}_2^2 \rangle_\xi = \frac{1}{4}e^{2r}. \quad (2.62)
$$

We have shown that the squeeze operator is able to lower the uncertainty for the measurement of one quadrature if applied to the vacuum state. As the displacement operator does not affect the uncertainty of a vacuum state we want to see if it affects the amount of squeezing if applied to a squeezed vacuum state

$$|\alpha,\xi\rangle = \hat{D}(\alpha)\hat{S}(\xi)|0\rangle \tag{2.63}$$

The eigenvalue of the annihilation operator is still $\langle \hat{a} \rangle_{\alpha,\xi} = \alpha$ because it is independent of the squeezing parameter. The photon number of the squeezed coherent state is (see Eq. (2.29))

$$\langle \hat{a}^\dagger \hat{a} \rangle_{\alpha,\xi} = |\alpha|^2 + \sinh^2 r, \tag{2.64}$$

so we get nonzero photons in addition to the coherent amplitude due to the $\sinh^2 r$ contribution. The expectation value of $|\alpha,\xi\rangle$ for an arbitrary quadrature is

$$\langle \hat{Y}_1 + i\hat{Y}_2 \rangle_{\alpha,\xi} = \alpha e^{-i\phi/2}, \tag{2.65}$$

and it can be shown [51] that

$$\langle \hat{Y}_1^2 \rangle_{\alpha,\xi} = \frac{1}{4}e^{-2r}, \tag{2.66}$$

$$\langle \hat{Y}_2^2 \rangle_{\alpha,\xi} = \frac{1}{4}e^{2r}. \tag{2.67}$$

Displacing the squeezed vacuum state by a coherent field amplitude does not affect the squeezing. Since the coherent state is a minimum uncertainty state we can produce a minimum uncertainty squeezed field with a coherent amplitude, so called *bright squeezed*, under the assumption that there are no losses.

2.3.4 Two-mode squeezed states

The quantum states we have calculated were considered to be states of a single-mode field. The experiments done in this work (see Ch. 7) use another kind of nonlinear state, the *two-mode squeezed* state. The

squeeze operator for the two-mode squeezed state is [51]

$$\hat{S}_2 \xi = e^{\xi^* \hat{a}\hat{b} - \xi \hat{a}^\dagger \hat{b}^\dagger} \tag{2.68}$$

where $\hat{a}$ and $\hat{b}$ are the annihilation operators for the two modes. With this the two-mode squeezed vacuum state of a two-mode vacuum $|0\rangle_a |0\rangle_b = |0,0\rangle$ is

$$|\xi_2\rangle = \hat{S}_2(\xi)|0,0\rangle. \tag{2.69}$$

The two-mode squeezed vacuum is not a product of two single-mode squeezed fields but an entangled state with strong correlations between the two modes $\hat{a}$ and $\hat{b}$. These correlations can be expressed as a superposition of the two modes. Therefore we define the superposition quadrature operators for the two-mode squeezed state [51]

$$\hat{x}_2 = \frac{1}{2^{3/2}}(\hat{a} + \hat{a}^\dagger + \hat{b} + \hat{b}^\dagger) \tag{2.70}$$

$$\hat{p}_2 = \frac{1}{i 2^{3/2}}(\hat{a} + \hat{a}^\dagger + \hat{b} + \hat{b}^\dagger). \tag{2.71}$$

The operators follow the commutation relation $[\hat{x},\hat{p}] = i/2$ and we can calculate the variance of the two-mode squeezed quadratures such as we have calculated the variance of the single-mode squeezed quadratures (see Eqs. (2.56), (2.57))

$$\begin{aligned}
\langle \hat{x}_2^2 \rangle_{\xi 2} &= \langle 0,0| \hat{S}^\dagger(\xi) \hat{x}^2 \hat{S}(\xi)|0,0\rangle \\
&= \frac{1}{4} \left[\cosh^2(r) + \sinh^2(r) - 2\sinh(r)\cosh(r)\cos(\phi) \right] \\
&= \frac{1}{4} \left[\cos^2\left(\frac{\phi}{2}\right) e^{2r} + \sin^2\left(\frac{\phi}{2}\right) e^{-2r} \right] \tag{2.72} \\
\langle \hat{p}_2^2 \rangle_{\xi 2} &= \langle 0,0| \hat{S}^\dagger(\xi) \hat{p}^2 \hat{S}(\xi)|0,0\rangle \\
&= \frac{1}{4} \left[\cosh^2(r) + \sinh^2(r) + 2\sinh(r)\cosh(r)\cos(\phi) \right] \\
&= \frac{1}{4} \left[\sin^2\left(\frac{\phi}{2}\right) e^{2r} + \cos^2\left(\frac{\phi}{2}\right) e^{-2r} \right]. \tag{2.73}
\end{aligned}$$

Again we get a reduced variance in the amplitude quadrature for $\phi = 0$

$$\langle \hat{x}_2^2 \rangle_{\xi,0} = \frac{1}{4} e^{-2r} \tag{2.74}$$

$$\langle \hat{p}_2^2 \rangle_{\xi,0} = \frac{1}{4} e^{2r}. \tag{2.75}$$

This result is the same as for the single-mode vacuum squeezed state.

CHAPTER 3

Generation and detection of squeezed states

In the previous chapter we have shown the prediction of squeezed states from the quantum mechanical description of light. In the first part of this chapter we want to introduce the nonlinear effects between light and matter which are necessary to generate squeezed light fields. The second part will give an introduction to the detection of the generated squeezed states.

3.1 Generation of squeezed light fields

Squeezed states can be generated through the nonlinear interaction of a light field with a dielectric material. We introduce the dielectric polarization in a simplified form describing this interaction of light with the valence electrons of the material

$$P = \epsilon_0 \left(\chi^{(1)} E + \chi^{(2)} E^2 + \chi^{(3)} E^3 + \cdots \right),$$ (3.1)

where E represents the driving electric field and $\chi^{(n)}$ the n-th order susceptibility of the medium (for a complete description see [55]). The linear dielectric susceptibility $\chi^{(1)}$ is related to the refractive index n_r of the medium via $n_\mathrm{r} = \sqrt{1 + \chi^{(1)}}$. The higher order susceptibilities

$\chi^{(2)}$, $\chi^{(3)}$ and so on are the nonlinear dielectric susceptibilities of the material. Their interaction strengths are much smaller than the linear interaction which is unity for condensed matter [55]. Commonly used dielectric media typically have interaction strengths of $\chi^{(2)}$ 10^{-10} – $10^{-13}mV^{-1}$ and $\chi^{(3)}$ is even smaller. Therefore nonlinear effects manifest themselves only for high intensities of the interacting light field.

The nonlinear media used for generating nonlinear interactions are in most cases dielectric crystals [56]. The effects in these nonlinear crystals can be divided into two classes. For the case of two strong monochromatic waves the second-order nonlinearity produces combinations of the two frequencies of the light fields $\omega_3 = \omega_1 \pm \omega_2$. This effect is called *sum/difference frequency generation* (SFG). For the special case that $\omega_1 = \omega_2$ SFG is called *second harmonic generation* (SHG). The second class is the opposite effect called *parametric down-conversion* (PDC) and occurs in the presence of a strong so-called *pump field* ω_3 which splits into two light fields with lower frequencies (*fundamental fields*) satisfying $\omega_3 = \omega_1 + \omega_2$. This effect is used for the generation of squeezing while the SHG process is used to generate the needed pump field. While SFG only generates light at the sum of the two fundamental frequencies within the frequency bandwidth of the fundamental light, the down-conversion effect is a broadband effect where any combination of generated photons is possible as long as energy conservation laws are fulfilled. Therefore other experimental parameters must be tuned to steer the effect to either degenerate squeezed fields or nondegenerate (e.g. frequency or polarization) fields. For frequency nondegenerate squeezed fields optical resonators are used to enhance the generation of squeezed fields at a given choice of frequencies. This technique is not used in the experimental part of this work, therefore we we focus on frequency degenerate squeezing in the following description.

The third-order nonlinear interaction is used for light fields with even higher intensities present in pulsed-laser experiments. Examples include the optical Kerr effect and Four Wave Mixing [55].

3.2 Phase matching

As the interaction strengths are fairly small, nonlinear effects can only be observed for high intensities, long interaction lengths and for the case that the phase-matching conditions (which result from momentum conservation laws) are fulfilled [55]. For ideal phase matching the wave vectors $\mathbf{k}_i$ must satisfy

$$\mathbf{k}_3 = \mathbf{k}_1 + \mathbf{k}_2, \tag{3.2}$$

with the wave vectors for the fundamental and pump field being defined as

$$|\mathbf{k}_i| = k_i = \frac{\omega_i}{c_i}. \tag{3.3}$$

The individual propagation velocity within the nonlinear crystal is

$$c_i = \frac{c}{n(\omega_i)}, \tag{3.4}$$

where c is the vacuum speed of light and $n(\omega_i)$ is the frequency dependent refractive index of the nonlinear crystal. In nonlinear crystals the refractive index is not only dependent on the frequency, but also on the polarization (vertical: *s-pol*, horizontal: *p-pol* see Eq. (2.7)) of the incident light. For three frequency interactions with degenerate fundamental frequency we can distinguish between two interaction types. The case where the fundamental field is fully degenerate in frequency and polarization is called *Type I* phase matching. If the two fundamental waves have orthogonal polarizations the interaction is called *Type II* phase matching. Typically, Type I interactions are stronger than Type II interactions in the same crystal [56]. Therefore the best values for quantum noise reduction and the best efficiencies for SHG have been shown with Type I interactions [57]. For our work Type II down-conversion processes and their corresponding crystals are of most interest because of the nondegeneracy in polarization of the resulting fields.

Phase matching can be achieved with different techniques [55]. The refractive index in anisotropic media is dependent on the direction of propagation. In uniaxial crystals we can define a reference called the

optical axis. The main plane of the crystal is spanned by the direction of propagation and the optical axis. Light polarized perpendicular to this main plane has the same refractive index for all incident angles θ_{in} between the optical axis and the direction of propagation. The refractive index of a parallel polarized beam has a dependency on the incident angle $n(\theta_{\mathrm{in}})$. For a proper choice of θ_{in} phase matching can be achieved for particular wavelengths and materials. Both Type I and Type II interactions can be phase matched this way, whereas Type II has more restrictions because three different refractive indices have to be matched. The technique using the incident angle θ_{in} for phase matching is called *angular* or *critical* phase matching. The main drawback with this method is the so-called *walk-off* between s- and p-polarized light fields for incident angles $\theta_{\mathrm{in}} \neq 90°$. Light fields with different polarization have different energy flux within the crystal and the effective interaction length is limited.

A second phase matching method that can be achieved is temperature tuning. Here the incident angle θ is fixed at $90°$ and the refractive indices are matched via temperature. With this technique no walk-off angles limit the geometry of the experiment. This so called *temperature* or *noncritical* phase matching is limited to a small set of materials and wavelengths as only one parameter can be addressed to tune the relative phase of the interacting wavelengths [56].

The third commonly used method is called *quasi-phase matching* [55]. This method allows any incident angle and temperature because the crystal structure is artificially changed to achieve phase matching. In most cases quasi-phase matching is used when the incident angle has to be $\theta_{\mathrm{in}} = 90°$ to circumvent walk-off and no temperature phase matching is possible. Assuming no phase matching present backconversion between fundamental and pump field will occur after a given interaction length. One can prevent this effect with periodic polarization of the crystal's domains which periodically inverts the sign of the effective nonlinear coefficient d_{eff}. The effective coupling strength d_{eff} for a given interaction is a crystal parameter dependent on the incident angle, interacting frequencies and the desired process and can be found
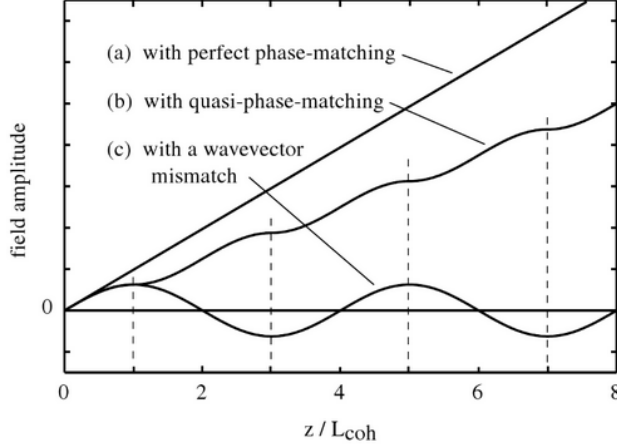
FIGURE 3.1: Compared amplitude of the generated field with different phase matchings as a function of traveled distance z inside the crystal [55]. The distance is normalized over the coherent length L_{coh} of the nonlinear interaction. For quasi-phase matching the field amplitude is reduced by a factor of $2/\pi$.

in [56] for the most nonlinear crystals. The optical phase accumulated over the optical path length through the crystal is

$$\Delta k = \frac{n_1\omega_1 + n_2\omega_2 - n_3\omega_3}{c} - \frac{2\pi}{\Lambda}, \qquad (3.5)$$

with the poling period Λ. As the phase mismatch is compensated by the periodic poling one can address couplings which are not accessible via angular or temperature phase matching. This broadens the range of usable materials and wavelengths. The major drawback of quasi-phase matching is illustrated in Fig. 3.1. For perfect noncritical phase matching the field amplitude of the generated field grows linearly. With quasi-phase matching the amplitude is reduced by a factor of $2/\pi$. Without any phase matching and a given wavevector mismatch the field amplitude oscillates periodically with the optical path length inside the crystal [55].

3.3 Quantum mechanical description of the generation of squeezed light

In the previous section we have stated that one can generate squeezed states with parametric down-conversion inside nonlinear media. The Hamiltonian describing the interaction of two light fields inside a nonlinear medium is given by [51]

$$\hat{H} = \hbar\omega\hat{a}^\dagger\hat{a} + \hbar\omega_{\mathrm{p}}\hat{b}^\dagger\hat{b} + i\hbar\chi^{(2)}\left(\hat{a}\hat{a}\hat{b}^\dagger - \hat{a}^\dagger\hat{a}^\dagger\hat{b}\right). \tag{3.6}$$

Here the fundamental field is denoted by $\hat{a}$ and the pump field is described by $\hat{b}$. The first two terms describe the carrier fields of the fundamental and the pump. The third term is the interaction term which describes the destruction of two fundamental photons to generate one pump photon and the generation of two fundamental photons by destroying one pump photon. The strength of the effect is set by the nonlinear susceptibility $\chi^{(2)}$. For an interaction where the pump field is not depleted and is in a coherent state $\hat{b} \to \beta e^{-i\omega_{\mathrm{p}}t}$ we can write the parametric approximation

$$\hat{H}_{\mathrm{app}} = \hbar\omega\hat{a}^\dagger\hat{a} + i\hbar\chi^{(2)}\left(\beta^*\hat{a}\hat{a}e^{i\omega_{\mathrm{p}}t} - \beta\hat{a}^\dagger\hat{a}^\dagger e^{-i\omega_{\mathrm{p}}t}\right). \tag{3.7}$$

In the rotating frame of the fundamental mode frequency ω this Hamiltonian reduces to

$$\hat{H}_{\mathrm{app}} = i\hbar\chi^{(2)}\left(\beta^*\hat{a}\hat{a}e^{i(\omega_{\mathrm{p}}-2\omega)t} - \beta\hat{a}^\dagger\hat{a}^\dagger e^{-i(\omega_{\mathrm{pump}}-2\omega)t}\right). \tag{3.8}$$

which, given the assumption that the pump frequency is twice the fundamental frequency, simplifies to the following form

$$\hat{H}_{\mathrm{app}} = i\hbar\chi^{(2)}\left(\beta^*\hat{a}\hat{a} - \beta\hat{a}^\dagger\hat{a}^\dagger\right). \tag{3.9}$$

The evolution operator of this parametric process is

$$\hat{U}(t) = e^{-i\hat{H}_{\mathrm{app}}t/\hbar} = e^{\chi^{(2)}\left(\beta^*\hat{a}\hat{a} - \beta\hat{a}^\dagger\hat{a}^\dagger\right)} \tag{3.10}$$

and has the same form as the squeeze operator in Eq. (2.55). With this shown we can see that squeezed light fields can be generated with a parametric down-conversion process inside a nonlinear medium using a $\chi^{(2)}$ interaction.

3.4 Detection of squeezed states

3.4.1 Direct detection

The main tool for the characterization of light fields is the photo detector. Ideally it converts any incident photon into an electrical current which can be read out by signal analyzers. The resulting current $i(t)$ is proportional to the number of photons in the incoming optical field [58]

$$
\begin{aligned}
i(t) \sim \hat{n}(t) &= \hat{a}^{\dagger}(t)\hat{a}(t) \\
&\approx \alpha^2 + \alpha\delta\hat{x}
\end{aligned}
\tag{3.11}
$$

where we used the linearized form of the annihilation operator $\hat{a} = \alpha + \delta\hat{a}$ [59]. We can see that the photocurrent is a combination of a large direct current proportional to the intensity of the light and a fluctuating term originating from the fluctuations of the amplitude quadrature multiplied by the mean field amplitude. This result shows that we are only able to measure the fluctuations of the amplitude quadrature with a single detector. If we have no coherent field, which is the case for vacuum states, a single detector is not able to measure any quadrature fluctuations. If we are interested in other quadratures or vacuum squeezed states we must use a more elaborate detection scheme.

3.4.2 Balanced homodyne detection

To have access to the measurement of any quadrature of the light field we can use the *balanced homodyne detection* scheme [60]. Instead of using one single detector we interfere the signal field $\hat{a}$ with a strong local oscillator $\hat{b}$ on a beamsplitter with equal power reflectivity R and transmission T. The two corresponding output fields of the beamsplitter are

detected on two individual photodetectors. The differential signal of these detections is then measured with a spectrum analyzer. Given that the optical frequencies of the interfering beams are equal and we have no resulting beat frequencies in the mean amplitudes, the interaction at the beamsplitter can be calculated with [61]

$$
\begin{pmatrix} \hat{c} \\ \hat{d} \end{pmatrix} = \begin{pmatrix} \rho & \tau \\ -\tau & \rho \end{pmatrix} \begin{pmatrix} \hat{a} \\ \hat{b} \end{pmatrix},
\tag{3.12}
$$

where $\rho = \sqrt{R}$ and $\tau = \sqrt{T}$ are the amplitude reflectivity and transmissivity of the beamsplitter, respectively. For a balanced homodyne detection scheme we need a beamsplitter ratio of $50/50$ which yields

$$
\begin{pmatrix} \hat{c} \\ \hat{d} \end{pmatrix} = \frac{1}{\sqrt{2}} \begin{pmatrix} 1 & 1 \\ -1 & 1 \end{pmatrix} \begin{pmatrix} \hat{a} \\ \hat{b} \end{pmatrix},
\tag{3.13}
$$

for the coupling of the input and output fields using the asymmetric beamsplitter convention [61]. As we have shown in Eq. (3.11) the photocurrent of a photodetector $i_j(t)$ is proportional to the number state of the detected field which results in the output fields $\hat{c}, \hat{d}$

$$
i_1 \sim \hat{c}^\dagger \hat{c} = \frac{1}{2}(\hat{a}^\dagger + \hat{b}^\dagger)(\hat{a} + \hat{b})
\tag{3.14}
$$

$$
i_2 \sim \hat{d}^\dagger \hat{d} = \frac{1}{2}(-\hat{a}^\dagger + \hat{b}^\dagger)(-\hat{a} + \hat{b}).
\tag{3.15}
$$

By linearizing the operators into their real steady state and fluctuation terms, and adding the differential phase $e^{i\theta}$ between the interfering beams to the local oscillator field such that

$$
\hat{a} = \alpha + \delta\hat{a}
\tag{3.16}
$$

$$
\hat{b} = \hat{b}_0 e^{i\theta} = \beta_0 e^{i\theta} + \delta\hat{b}_0 e^{i\theta},
\tag{3.17}
$$

the photocurrents from Eq. (3.14) and Eq. (3.15) become

$$
\begin{aligned}
i_1 &= \frac{1}{2} \left(\alpha + \delta\hat{a}^\dagger + \beta_0 e^{-i\theta} + \delta\hat{b}^\dagger e^{-i\theta} \right) \left(\alpha + \delta\hat{a} + \beta_0 e^{i\theta} + \delta\hat{b} e^{i\theta} \right) \\
&= \frac{1}{2} \left[\alpha^2 + \beta_0^2 + 2\alpha\beta_0 \cos\theta + \alpha(\delta\hat{x}_a + \delta\hat{X}_b(-\theta)) + \beta_0(\delta\hat{x}_b + \delta\hat{X}_a(\theta)) \right],
\end{aligned}
$$
(3.18)

and

$$
\begin{aligned}
i_2 &= \frac{1}{2} \left(-\alpha - \delta\hat{a}^\dagger + \beta_0 e^{-i\theta} + \delta\hat{b}^\dagger e^{-i\theta} \right) \left(-\alpha - \delta\hat{a} + \beta_0 e^{i\theta} + \delta\hat{b} e^{i\theta} \right) \\
&= \frac{1}{2} \left[\alpha^2 + \beta_0^2 - 2\alpha\beta_0 \cos\theta + \alpha(\delta\hat{x}_a - \delta\hat{X}_b(-\theta)) + \beta_0(\delta\hat{x}_b - \delta\hat{X}_a(\theta)) \right],
\end{aligned}
$$
(3.19)

where $\hat{x}_a$ and $\hat{x}_b$ are the amplitude quadratures of the input fields and the generic quadrature operators $\delta\hat{X}_a(\theta)$ and $\delta\hat{X}_b(\theta)$ are specified in Eq. (2.37). The fluctuation terms are assumed to be small and we neglect terms of order δ^2. The differential current is then

$$
i_- = i_1 - i_2 \sim \hat{c}^\dagger\hat{c} - \hat{d}^\dagger\hat{d} \tag{3.20}
$$
$$
= 2\alpha\beta_0 \cos\theta + \alpha\delta\hat{X}_b(-\theta) + \beta_0\delta\hat{X}_a(\theta). \tag{3.21}
$$

We calculate the variance of this current to be

$$
V_{i_-} = \alpha^2 V(\delta\hat{X}_b(-\theta)) + \beta_0^2 V(\delta\hat{X}_a(\theta)). \tag{3.22}
$$

For the measurement of vacuum squeezing we consider the coherent field of the signal to be small with respect to the local oscillator field ($\alpha^2 \ll \beta_0^2$) and the contribution of the term containing α^2 vanishes. The measurement of the variance then yields

$$
V_{i_-} = \beta_0^2 V(\delta\hat{X}_a(\theta)). \tag{3.23}
$$

We can see that with balanced homodyne detection it is possible to measure the fluctuations of a signal field scaling with the coherent power of the local oscillator. The measurement phase can be tuned arbitrarily by shifting the local oscillator phase. If the measurement has no noise

input and the splitting ratio of the beamsplitter is ideally set to $50/50$ the measurement contains neglectable noise contributions from the local oscillator field in the first-order approximation.

3.4.3 Detection of two-mode squeezed states

We have shown that we can measure the quadrature fluctuations of a single-mode squeezed field with the homodyne detection scheme. The detection of two-mode squeezed states is more complex because we must measure the superposition of two states to gain information about the amount of two-mode squeezing. If we insert the amplitude and phase quadrature operators into the superposition quadrature operators for the two-mode squeezed state from Eq. (2.70) we get

$$\hat{x}_2 = \frac{1}{2}(\hat{x}_a + \hat{x}_b) \tag{3.24}$$

$$\hat{p}_2 = \frac{1}{2}(\hat{p}_a + \hat{p}_b). \tag{3.25}$$

To measure two-mode squeezed states in the amplitude quadrature we set the squeezing angle $\phi = 0$ (see Eq. (2.74)). For the measurement this means that we must separate the two-mode squeezed fields into the two individual modes and measure their amplitude quadratures. The addition of the phase quadratures gives the antisqueezed states.

For phase squeezing the squeezing angle is set to $\phi = \pi$. The superposition quadratures then become

$$\hat{x}_2 = \frac{1}{2}(\hat{x}_a - \hat{x}_b) \tag{3.26}$$

$$\hat{p}_2 = \frac{1}{2}(\hat{p}_a - \hat{p}_b). \tag{3.27}$$

The difference of the two individual phase quadratures yields two-mode squeezing in the phase quadrature and antisqueezing in the amplitude quadrature. For the actual measurement of two-mode squeezing in an experiment (see Ch. 7) we must set up two equal homodyne detectors to measure the individual quadratures of the two-modes $\hat{a}$ and $\hat{b}$ and add or subtract the photocurrents to measure the superposi-

tion quadratures.

3.5 Influence of loss on squeezed fields

The calculations thus far have assumed an ideal lossless environment. For the experimental detection of squeezing we have to assume incoupling loss channels at imperfect high reflection (HR) or antireflection (AR) coatings, nonideal spatial overlap of local oscillator and signal field at the detection, nonideal beamsplitting ratios at the homodyne detector and the quantum efficiency of the photodetectors. A first complete calculation of squeezed light including losses was given in [62]. These loss channels can be modeled with a beamsplitter with a certain power reflectivity $R = 1 - \eta$ where the signal field $\hat{a}$ is interfered with an incoupling vacuum field $\hat{v}$. We assume the light to be detected in transmission of the beamsplitter. With the formalism used in Eq. (3.12) we get the resulting signal field including loss

$$\hat{c} = \sqrt{\eta}\hat{a} + \sqrt{1 - \eta}\hat{v}. \tag{3.28}$$

The variance V_η of the squeezed field including losses measured with the balanced homodyne detection scheme then becomes

$$V_\eta = \eta V_0 + (1 - \eta). \tag{3.29}$$

We see the effect of incoupled loss on light fields with a certain amount of squeezing (in dB) in Fig. 3.2

$$V[dB] = -10\log_{10}\left(\eta 10^{V_0/10} + (1 - \eta)\right). \tag{3.30}$$

Squeezing is affected more by losses than antisqueezing, and larger squeezing values are more vulnerable to losses than smaller ones. We can see that for an infinite initial squeezing value with 10 % loss the detectable squeezing is limited to 10 dB. For loss values of 50 % the squeezing value is reduced further down to 3 dB.

This result has a direct consequence for the design of an experiment using squeezed states. Every part of the experiment which interacts with
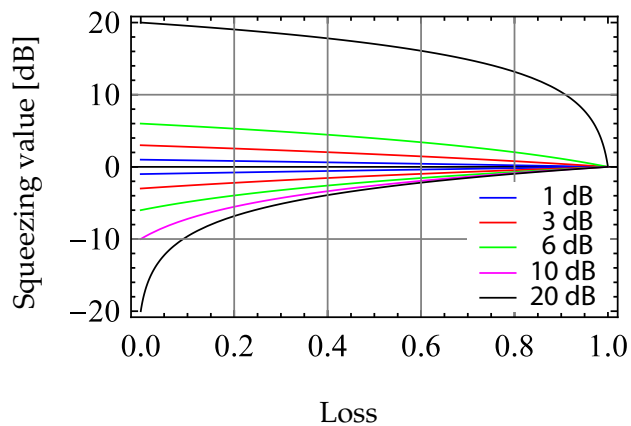
FIGURE 3.2: Influence of loss on squeezed and antisqueezed states with squeezing values from $\pm 1\,$dB up to $\pm 20\,$dB. States with a larger squeezing value are more vulnerable to loss than weakly squeezed states.

the squeezed field must be perfectly aligned and must be of the highest optical quality to reduce any loss contribution which would destroy the squeezed field.

Optical resonators

Optical resonators are used frequently in many parts of this work. This includes the resonant enhancement of the laser mode in the fundamental light source and the use of modecleaning cavities. Also, since the effects in nonlinear crystals are very small we use optical resonators to enhance the effects of second harmonic generation and parametric down-conversion. The general resonance behavior of these resonators is described in Sec. 4.1. The CQNC scheme by M.Tsang [43] calls for a coupled resonator topology which we investigate in Sec. 4.2.

4.1 Two mirror cavity

A Fabry-Perot resonator in its original description is formed by two mirrors at a distance L (see Fig. 4.1). The resonance feature of a light field with angular frequency $\omega_0 = 2\pi/\lambda \cdot c$ is defined by the input and output fields a,b, the reflectivities of the mirrors ρ_i and the phaseshift $\phi = kL$ induced by the light traveling the resonator length L.
We describe the cavity by use of the scattering matrix formalism [61] with the matrix $\mathbf{M}$ for a single mirror with amplitude reflection ρ_i,
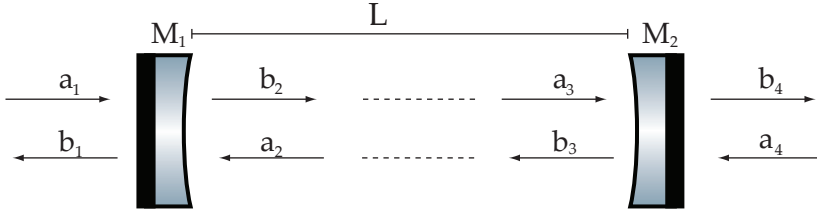
FIGURE 4.1: Model of a two-mirror Fabry-Perot cavity.

transmission coefficients τ_i and the propagation matrix $\mathbf{L}$

$$\mathbf{M_i} = \begin{pmatrix} \rho_i & i\tau_i \\ i\tau_i & \rho_i \end{pmatrix}, \quad \mathbf{L} = \begin{pmatrix} 0 & e^{ikL} \\ e^{ikL} & 0 \end{pmatrix}. \tag{4.1}$$

We connect these matrices with the input a_i and output b_i amplitudes to obtain the full description for the coupling of light fields with the cavity:

$$\begin{pmatrix} b_1 \\ b_2 \end{pmatrix} = \begin{pmatrix} \rho_1 & i\tau_1 \\ i\tau_1 & \rho_1 \end{pmatrix} \begin{pmatrix} a_1 \\ a_2 \end{pmatrix} \tag{4.2}$$

$$\begin{pmatrix} a_2 \\ a_3 \end{pmatrix} = \begin{pmatrix} 0 & e^{ikL} \\ e^{ikl} & 0 \end{pmatrix} \begin{pmatrix} b_2 \\ b_3 \end{pmatrix} \tag{4.3}$$

$$\begin{pmatrix} b_3 \\ b_4 \end{pmatrix} = \begin{pmatrix} \rho_2 & i\tau_2 \\ i\tau_2 & \rho_2 \end{pmatrix} \begin{pmatrix} a_3 \\ a_4 \end{pmatrix}. \tag{4.4}$$

With only one input field at $a_1 = a_{\text{in}}$ and $a_4 = 0$ we determine the output amplitudes b_1 and b_4 and the intracavity field b_2

$$b_1 = a_{\text{in}} \left[\rho_1 - \rho_2(\rho_1^2 + \tau_1^2)e^{ikL} \right] d$$
$$b_2 = ia_{\text{in}}\tau_1 d \tag{4.5}$$
$$b_4 = -a_{\text{in}}\tau_1\tau_2 e^{ikL} d$$

where the resonance factor d of the cavity is

$$d = \frac{1}{1 - \rho_1\rho_2 e^{i\Phi}}. \tag{4.6}$$

The detuning parameter $\Phi = 2\omega L/c$ describes the phase which is obtained by the light traveling through the cavity. For $\Phi = \mathrm{mod}(\pi)$ the squared absolute value of the resonance factor $|d|^2$ has a maximum which is called resonance. The resonance frequencies are the frequencies which fulfill this condition

$$\omega_j^{\mathrm{res}} = \frac{2\pi c}{2L} j \tag{4.7}$$

where j is an integer. The frequency distance between two adjacent resonances is called the *free spectral range* (FSR) [61] and is given by

$$\mathrm{FSR} = \frac{1}{2\pi} \left(\omega_{j+1}^{\mathrm{res}} - \omega_j^{\mathrm{res}} \right) = \frac{c}{2L}. \tag{4.8}$$

We have calculated the expressions for a linear Fabry-Perot cavity in Eq. (4.5) because the input and output mechanisms can be expressed with 2×2 scattering matrices. For traveling wave ring-cavities the scattering matrices for the mirrors expand to 4×4-matrices which results in a more complicated calculation whereas the main formalism and the behavior of the cavity resonance does not change. The only difference is the resulting FSR, which is in this case $\mathrm{FSR} = c/L_{\mathrm{rc}}$, where L_{rc} is the ring cavity roundtrip length.

Another important quantity describing the behavior of a cavity is the *full width at half maximum* (FWHM) linewidth. For the detuning at half maximum Φ_{HM} we must solve the following equation

$$\frac{1}{2}|d|^2(0) = |d|^2(\Phi_{\mathrm{HM}}), \tag{4.9}$$

which gives

$$\Phi_{\mathrm{HM}} = \pm \frac{1}{2} \arccos \left(1 - \frac{(1 - \rho_1\rho_2)^2}{2\rho_1\rho_2} \right). \tag{4.10}$$

With this we can express the FWHM linewidth in Fourier frequencies [63]

$$\Delta\nu_{\mathrm{FWHM}} = \frac{2\Phi_{\mathrm{HM}}c}{2\pi L}. \tag{4.11}$$

The ratio between FSR and FWHM is the so called Finesse $\mathcal{F}$ of a resonator which is another characteristic often used for describing optical
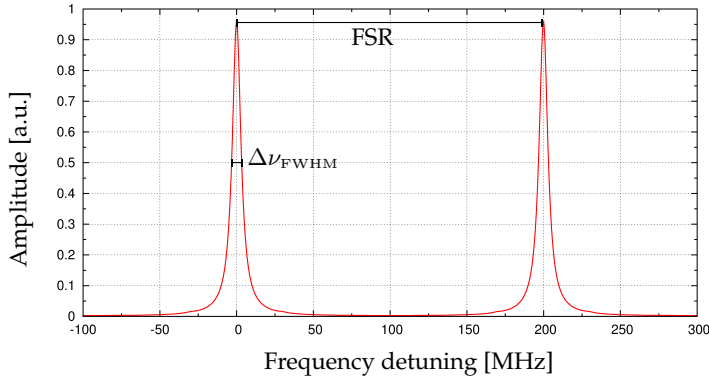
FIGURE 4.2: Transmitted power of a Fabry-Perot resonator scanned by laser frequency detuning from the fundamental frequency. We see the resonance featured Airy peaks, the FSR and the FWHM-linewidth ($\Delta\nu_{\mathrm{FWHM}}$).

cavities [63]

$$\mathcal{F} = \frac{FSR}{\Delta\nu_{\mathrm{FWHM}}}. \tag{4.12}$$

4.2 Coupled optical resonators

For the proposed coherent quantum noise cancellation scheme (see Ch. 6), a system of two coupled optical resonators is needed. The effects observed in different topologies of coupled cavities have been in the context of for gravitational wave detectors such as *resonant sideband extraction*[64], *twin signal recycling* [65] and the so called *Khalili-cavities* [66]. Analytical descriptions have been ascertained for coupled cavities in [67, 68]. Similar descriptions have been calculated for optical communication channels where coupled cavities are used as bandpass filters or delay lines [69, 70]. I will give an overview of these results with a slightly different focus regarding coupling strengths and tuning of the coupled optical system.

Analogous to the description of a two-mirror cavity in Sec. 4.1 we solve the input and output linear equations expressed by the scattering matrices describing the system. The notation for the input and output
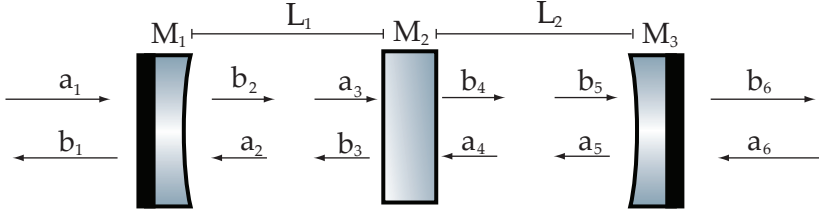
FIGURE 4.3: Model of a coupled three-mirror Fabry-Perot cavity.

fields is shown in Fig. 4.3. We can describe the system with a matrix equation [61]

$$\mathbf{x}_{\text{out}} = \mathbf{C}\mathbf{x}_{\text{in}} \tag{4.13}$$

where $\mathbf{x}_{\text{in}} = (a_1,a_2,b_2,b_3,a_3,a_4,b_4,b_5,a_5,a_6)$ is the input vector, the output vector $\mathbf{x}_{\text{out}} = (b_1,b_2,a_2,a_3,b_3,b_4,a_4,a_5,b_5,b_6)$ and the overall scattering matrix $\mathbf{C}$ containing the matrices for the mirrors and the cavity lengths is

$$\mathbf{C} = \begin{pmatrix} \mathbf{M}_1 & 0 & 0 & 0 & 0 \\ 0 & \mathbf{L}_1 & 0 & 0 & 0 \\ 0 & 0 & \mathbf{M}_2 & 0 & 0 \\ 0 & 0 & 0 & \mathbf{L}_2 & 0 \\ 0 & 0 & 0 & 0 & \mathbf{M}_3 \end{pmatrix} \tag{4.14}$$

We can derive the reflection $\rho_{3\text{m}}$ and transmission $\tau_{3\text{m}}$ coefficients for this system for a given input $a_1 = a_{\text{in}}$ and no input at the second input port $a_6 = 0$

$$\rho_{3\text{m}} = a_{\text{in}} \left(\rho_1 - e^{2i\Phi_1} (\rho_2 - e^{2i\Phi_2} \rho_3) - e^{2i\Phi_2} \rho_1 \rho_2 \rho_3 \right) d_{3\text{m}}, \tag{4.15}$$

and

$$\tau_{3\text{m}} = -a_{\text{in}} \left(i e^{i(\Phi_1 + \Phi_2)} \tau_1 \tau_2 \tau_3 \right) d_{3\text{m}}. \tag{4.16}$$

We have introduced the new resonance factor $d_{3\text{m}}$ for the complete system which depends on both intracavity phases Φ_1, Φ_2 and the reflectiv-

ities of the individual mirrors

$$d_{3m} = \frac{1}{1 - e^{2i\Phi_1}\rho_1\rho_2 - e^{2i\Phi_2}\rho_2\rho_3 + e^{2i(\Phi_1+\Phi_2)}\rho_1\rho_3}. \tag{4.17}$$

The solution for the intracavity fields of the coupled system yields

$$a_{int1} = a_{in}i\tau_1(1 - e^{2i\Phi_2}\rho_2\rho_3)d_{3m}, \tag{4.18}$$

and for the second cavity

$$a_{int2} = -a_{in}\left(e^{i\Phi_1}\tau_1\tau_2\right)d_{3m}. \tag{4.19}$$

For fixed values of Φ_2 we can treat the second cavity as a compound mirror with fixed reflectivity ρ_{23} and reduce the problem of a coupled system to a two-mirror-cavity problem [68]. The reflection coefficient of the three-mirror cavity can then be written as

$$\rho_{3m} = \frac{\rho_1 - \rho_{23}e^{2i\Phi_1}}{1 - \rho_1\rho_{23}e^{2i\Phi_1}} \tag{4.20}$$

which is similar to the description of a two-mirror cavity (see Eq. (4.5)). The reflectivity of the second cavity is a complex number depending on Φ_2 and has the form

$$\rho_{23} = \frac{\rho_2 - \rho_3e^{2i\Phi_2}}{1 - \rho_2\rho_3e^{2i\Phi_2}}. \tag{4.21}$$

The above description gives a fundamental understanding for the behavior of a system which consists of two coupled cavities. Due to the dependencies of the cavities on the individual reflectivities and the relative phases simple expressions for the FSR or resonance conditions are not straightforward to obtain, as opposed to the case for the two-mirror cavity. In the following we will discuss the behavior with simulations generated with the simulation tool *Finesse* [71] by A. Freise which uses the same formalism to simulate optical systems. The objective is here to obtain a deeper insight into the behavior of coupled resonators. The Finesse code used for the simulations can be found in Appendix 8.
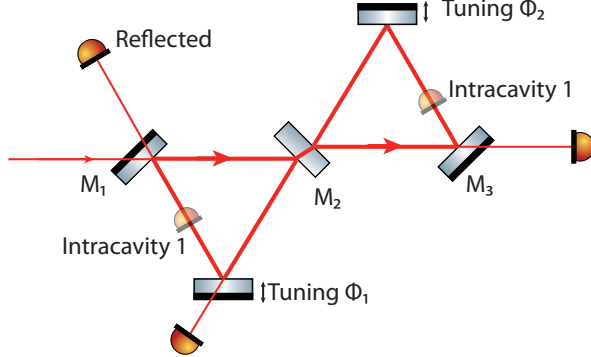
FIGURE 4.4: Schematic of the ring cavity for the Finesse simulations. We look at the intracavity fields and the reflected power of the cavity.

4.2.1 Resonance features

In this section we concentrate on the resonance behavior of the coupled cavity system with fixed reflectivities and variable tunings Φ_1 and Φ_2. For the simulation we used the values $\rho_1^2 = 0.9$, $\rho_2^2 = 0.8$ and $\rho_3^2 = 0.7$ for the reflectivities of the mirrors to ensure the results could be easily visualized. We have chosen the same values as in [68] to compare the results of our calculations. The modeled resonators are three-mirror ring resonators (see Fig. 4.4) and have an equal length of $1.5\,\mathrm{m}$ and therefore a FSR range of $\sim 200\,\mathrm{MHz}$ which is the same as for the coupled ring resonators we characterized in Sec. 7.3. As we have stated in Sec. 4.1 the formalism expands to 4×4-matrices for the mirror matrices but the resonance features do not change qualitatively.

We see the light enhancement of the intracavity fields for both individual cavities in Fig. 4.5. The resonance pattern for the first cavity is periodic in $\Phi_1 \bmod(\pi)$ and for the second cavity in $\Phi_2 \bmod(\pi)$. We see that for one cavity on antiresonance $\Phi_i = 90°$ the other cavity behaves like a single Fabry-Perot cavity. For both cavities on resonance $\Phi_i = 0°$ the internal light fields counteract each other and the build up of the field inside the cavities is minimal. This can be explained by the reflection coefficients of the two cavities being on resonance. From

(a) Intracavity 1
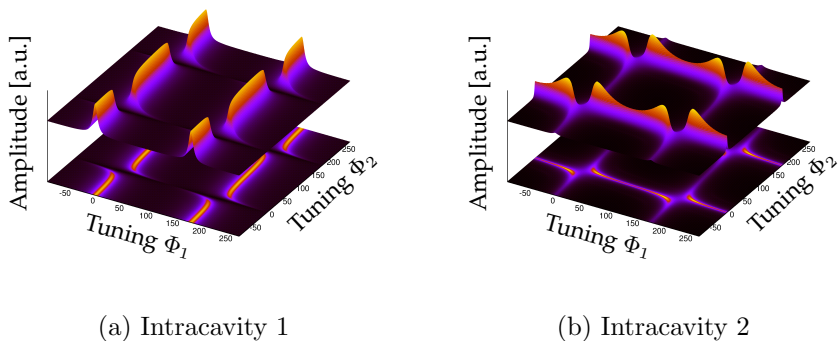
(b) Intracavity 2

FIGURE 4.5: Intracavity fields of the first cavity (a) and the second cavity (b) dependent on the tunings Φ_1 and Φ_2. The color coded map at the bottom will be used for further visualizations of resonance features of the coupled cavity.
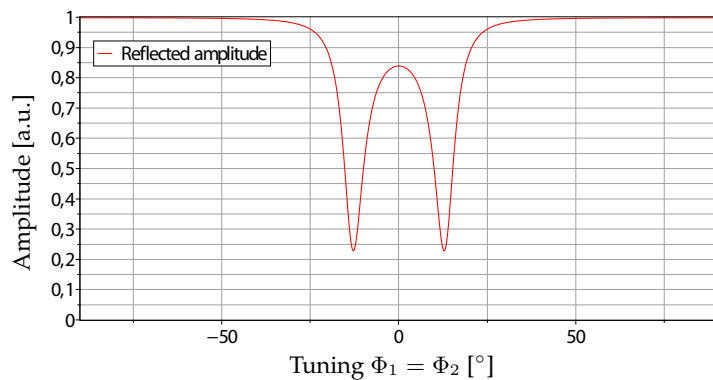

FIGURE 4.6: Frequency splitting of the resonance with tuning $\Phi_1 = \Phi_2$. The frequency distance of the resonance peaks depends on the reflectivity ρ_2 of the coupling mirror.
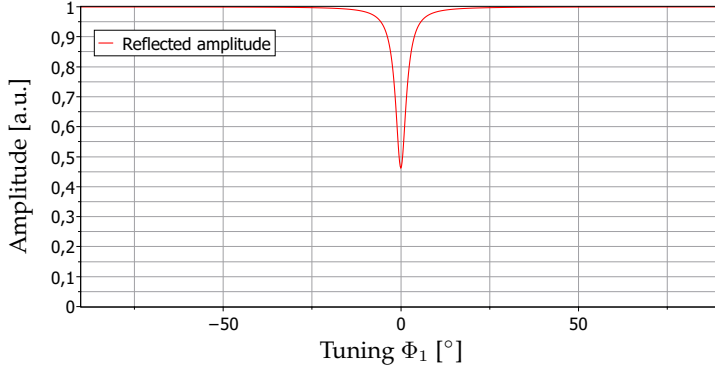
FIGURE 4.7: Reflected amplitude of a coupled cavity as a function of the tuning Φ_1. The second cavity is set to antiresonance $\Phi_2 = 90°$. We see a normal Airy-peak without any information about the free spectral range and the cavity linewidth.

Eq. (4.21) we can deduce that the reflection coefficient for one cavity on resonance has a minimum. For both cavities on resonance both cavities see the other as a 'bad' mirror which reduces the finesse and the build-up of the light field inside the cavities.

Another important feature which is used in techniques like the resonant sideband extraction scheme for Advanced Ligo and Virgo [64] can be seen when both tunings are changed simultaneously. Fig. 4.6 shows the resonance pattern for a scan of the reflected light field of the coupled cavity with $\Phi_1 = \Phi_2$. We see a splitting of resonances into a resonance doublet with a frequency splitting of Δf. This frequency splitting can be tuned by the parameters of the coupled resonators. The experimental scheme which is investigated in this work does not use the effect of the resonance doublet, therefore we refer to [68] for a more detailed analysis of these effects.

4.2.2 Free spectral range of a coupled cavity

As described in Sec. 4.1 one characteristic quantity of optical resonators is the FSR. For the two-mirror cavity we have deduced the FSR by cal-

culating the frequency distance between two neighboring resonances following Eq. (4.8). Here the FSR is only dependent on the length of the cavity. From the analytical description in Sec. 4.2 we know that we cannot define two neighboring resonances, as the resonance condition depends not only on the tuning of one cavity but is a function of the relative tunings and reflectivities of the coupled cavities.

To analyze the effective behavior of the coupled cavities on relative tunings and the coupling mirror we hold the cavities at fixed relative tunings and change the power reflectivity ρ_2^2 of the coupling mirror. To understand the resonance conditions for this setup we scan the laser frequency and display the intracavity field of the first cavity.

First we concentrate on the case where the second cavity is held at an antiresonance $\Phi_2 = 90°$. In Fig. 4.7 we see the scan of the first cavity and obtain the resonance condition $\Phi_1 = \text{mod}(\pi)$. We now raise the question of the length we have to consider to calculate the FSR of the coupled cavity. This length depends on the reflectivity of the coupling mirror ρ_2 between the two cavities as we can deduce from the extrema $\rho_2 = 1$ and $\rho_2 = 0$. For the case that the coupling mirror has a reflectivity of $\rho_2 = 1$ the light only travels inside the first cavity and the FSR is $c/2L_1$. The opposite case ($\rho_2 = 0$) yields a FSR of $c/2(L_1 + L_2)$ since the coupled cavity is effectively a *long* two-mirror cavity with the combined length ($L_1 + L_2$).

The effective behavior of the FSR of coupled cavities on antiresonance can be understood when scanning the laser wavelength over a span of multiple FSR's and simultaneously changing the reflectivity of the coupling mirror (see Fig. 4.8). With decreased reflectivity ρ_2 a second resonance peak builds up at half the FSR which is the combined FSR of the two cavities with length $L = 1.5\,\text{m}$ each. The resonance condition for the *long* cavity is $\Phi_1 = 0°$ and $\Phi_2 = 90°$. The combined FSR of the coupled cavity is therefore a combination of the FSR from the short cavity and the FSR of the long cavity weighted with the reflectivity of
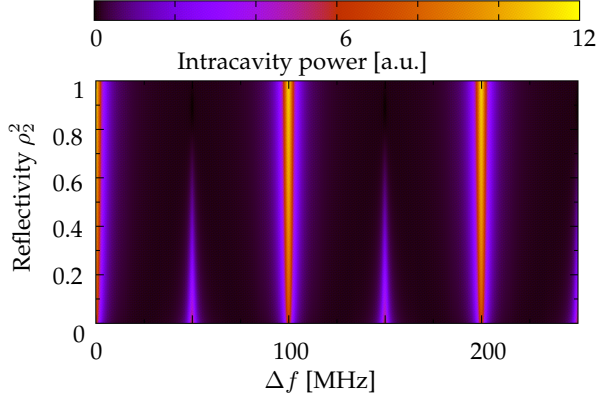
FIGURE 4.8: Intracavitiy field of the first cavity with detuned laser frequency Δf and reflectivity of the coupler between first and second cavity. The second cavity is held on antiresonance $\Phi_2 = 90°$ We can see the FSR of $\sim 200\,$MHz of the first cavity. With reduced reflectivity ρ_2 a second FSR at $\sim 100\,$MHz appears. This additional FSR arises from the cavity of combined lengths $L_1 + L_2$.

the coupling mirror. Our analysis dermines the effective length to be

$$L_{\text{eff}} = L_1 \rho_2^2 + (L_1 + L_2)(1 - \rho_2^2) \tag{4.22}$$

which is also confirmed by our experiments in Sec. 7.3 where we characterized the effective behavior of tunings and the reflectivity of a tunable coupling mirror.

This effect has no impact on concepts like *Khalili-cavities* and *resolved sideband extraction*, the schemes are calculated for cavities with $L_1 \gg L_2$ and the change in the FSR has a neglectable impact on the total FSR. For schemes with coupled resonators of the same length, like *twin-signal-recycling* or the coherent quantum noise cancellation scheme investigated in this work, these effects have to be taken into account.

When both cavities are on resonance ($\Phi_1 = \Phi_2 = 0°$) we again see in Fig. 4.10 the resonance splitting from Fig. 4.6 for the coupled cavities when tuning the laser frequency. The splitting grows in frequency with reduced reflectivity ρ_2 until a symmetric, periodic resonance feature is again reached for $\rho_2 = 0$. In this case we are not able to define a FSR
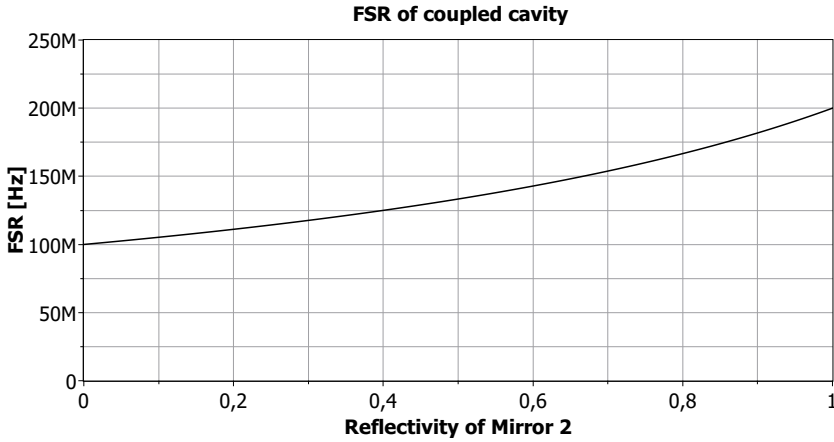
FIGURE 4.9: FSR of coupled cavity with equal lengths of 1.5 m and a relative
tuning $\Phi_2 = 90°$ as a function of the reflectivity ρ_2 of the coupling mirror.
The FSR can be tuned dynamically between the FSR for a single cavity with
length 1.5 m and the FSR of a cavity with an overall length of 3 m.
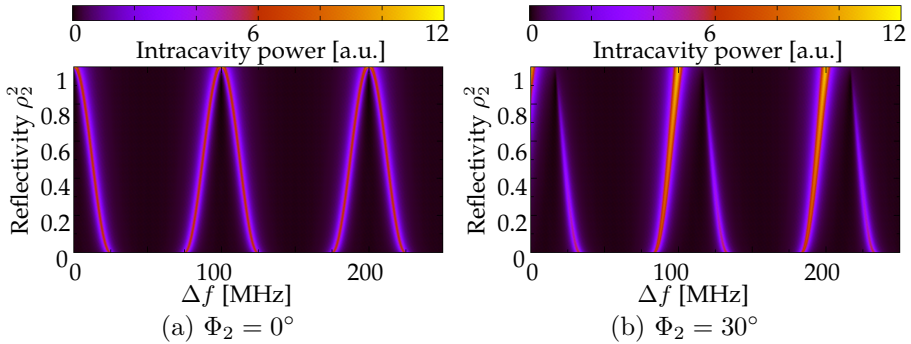
FIGURE 4.10: Intracavity field of the first cavity with detuned laser frequency
Δf and reflectivity of the coupler between first and second cavity. (a) The
second cavity is held on resonance $\Phi_2 = 0°$. We can see the resonance split-
ting due to the coupled cavities with reduced reflectivity ρ_2. (b) For a de-
tuning of the second cavity $\Phi_2 = 30°$ the resonance splitting becomes asym-
metric in amplitude. In addition, the frequency splitting becomes broader
for higher reflectivities than it is the case for the cavities with the same tun-
ing.

for the coupled cavity with $0 < \rho_2 < 1$ because of the unbalanced frequency distribution of the resonance peaks.

For detunings between $0°$ and $90°$ the resonance doublet becomes asymmetric in amplitude 4.10b. This effect is used for tuned resonant sideband extraction where distinct frequencies in the detection band are enhanced using the frequency splitting and the stronger resonance branch of the resonance doublet.

The simulations demonstrated in this section show that coupled cavities show different effects for changes in relative tuning and coupling strength ρ_2. The scheme which is analyzed in Ch. 6 calls for the use of detuned coupled cavities. Therefore we continue the analysis of coupled cavities experimentally in Sec. 7.3 to investigate possible stabilization techniques for different detunings.

Optomechanical oscillators

5.1 The classical mechanical oscillator

The quantum noise cancellation scheme [43], which is the main part of this work, consists of two parts: one optical and one mechanical. In Ch. 2 we performed the quantization of the electromagnetic field, this chapter will give a brief introduction to the classical mechanical harmonic oscillator and its quantization.

We start by describing the system's dynamics with Newton's second law

$$F = m\ddot{x}_{\mathrm{m}} = -kx_{\mathrm{m}}, \tag{5.1}$$

where F is a force, m the mass of the harmonic oscillator and k the spring constant. The position is denoted by x_{m} and the acceleration by $\ddot{x}_{\mathrm{m}}$. A simple solution for this equation of motion is

$$x_{\mathrm{m}}(t) = A\sin(\omega_{\mathrm{m}}t + \phi_{\mathrm{m}}), \tag{5.2}$$

where A is the amplitude and ϕ_m a phase, both of which are dependent on the initial conditions $x_m(0), \dot{x}_m(0)$

$$A_m = \sqrt{\frac{\dot{x}_m^2(0)}{\omega_m} + x_m^2(0)}, \tag{5.3}$$

$$\phi_m = \arctan\left(\omega_m \frac{x_m(0)}{\dot{x}_m(0)}\right). \tag{5.4}$$

The eigenfrequency ω_m of the system is

$$\omega_m = \sqrt{\frac{k}{m}}. \tag{5.5}$$

The total energy of the system which consists of potential and kinetic energy is then

$$E_{tot} = \frac{1}{2}m\omega_m^2 A^2 \tag{5.6}$$

Under realistic conditions the motion of the oscillator is influenced by the environment. We add a damping mechanism to the equations of motion

$$\ddot{x}_m + \gamma_m \dot{x}_m + \omega_m^2 x_m = 0 \tag{5.7}$$

where γ_m is the damping rate. Another important parameter is the mechanical quality factor, defined as

$$Q = \frac{\omega_m}{\gamma_m}, \tag{5.8}$$

which is a good measure for the performance of the mechanical oscillator. As damping is not the only environmental interaction with the oscillator we consider additional external forces driving the motion of the harmonic oscillator. The full equation of motion for the driven damped harmonic oscillator is then

$$\ddot{x}_m + \gamma_m \dot{x}_m + \omega_m^2 x_m = \frac{F_{ext}(t)}{m}. \tag{5.9}$$

5.2 Quantization of the mechanical harmonic oscillator

The quantization of the mechanical harmonic oscillator is fundamentally the same as for the electromagnetic field. We start with the Hamiltonian representation of the total energy of the system (see Eq. (5.6))

$$H = \frac{1}{2} \left(m\omega_{\mathrm{m}}^2 x_{\mathrm{m}}^2 + \frac{p_{\mathrm{m}}^2}{m} \right). \tag{5.10}$$

where x_{m} is the quantum mechanical position and $p_{\mathrm{m}} = m\dot{x}_{\mathrm{m}}$ the momentum. We replace the canonical variables with the dimensionless quantum operators

$$\hat{x}_{\mathrm{m}} = \sqrt{\frac{m\omega_{\mathrm{m}}}{\hbar}} x_{\mathrm{m}}, \tag{5.11}$$

$$\hat{p}_{\mathrm{m}} = \sqrt{\frac{1}{m\omega_{\mathrm{m}}\hbar}} p_{\mathrm{m}} \tag{5.12}$$

and rewrite the position and momentum operators with mechanical creation $\hat{b}^\dagger$ and annihilation $\hat{b}$ operators

$$\hat{x}_{\mathrm{m}} = \frac{1}{\sqrt{2}} (\hat{b} + \hat{b}^\dagger) \tag{5.13}$$

$$\hat{p}_{\mathrm{m}} = \frac{i}{\sqrt{2}} (\hat{b} - \hat{b}^\dagger). \tag{5.14}$$

The operators $\hat{b}$ and $\hat{b}^\dagger$ follow the commutation relation $[\hat{b}, \hat{b}^\dagger] = 1$ as in the electromagnetic case, and therefore the Hamilton operator can be expressed as

$$\hat{H} = \hbar\omega_{\mathrm{m}} \left(\hat{b}^\dagger \hat{b} + \frac{1}{2} \right). \tag{5.15}$$

Repeated application of the annihilation operator yields the ground state with the zero point energy

$$E_{\mathrm{zp}} = \frac{\hbar\omega_{\mathrm{m}}}{2}. \tag{5.16}$$

Furthermore, as was the case for the vacuum fluctuations of the vacuum state of the electromagnetic field, we find the zero point fluctua-

FIGURE 5.1: Optomechanical cavity: the light field ω_c couples to the mechanical oscillator ω_m via photon backaction.
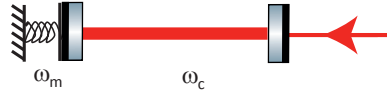
tion of the harmonic oscillator by calculating the variance of the position operator

$$\Delta_s x_{zp} = \sqrt{\langle \hat{x}_m^2 \rangle_0 - \langle \hat{x}_m \rangle_0^2} = \sqrt{\frac{\hbar}{m\omega_m}}. \tag{5.17}$$

5.3 Optomechanical resonators

Now we consider an optomechanical system consisting of a linear Fabry-Perot resonator and an optomechanical oscillator as an end mirror (see Fig. 5.1. The Hamiltonians for the single systems are given by Eq. (2.22) and Eq. (5.15). The coupled system gets an additional term due to the radiation pressure interaction of the light field with the optomechanical mirror. The resonance frequency of the cavity $\omega_c = 2\pi cn/L$ is coupled to the position of the mirror $\hat{x}_m$ via

$$\begin{aligned}
\omega_c(\hat{x}_m) &= \frac{2\pi cn}{L(\hat{x}_m)} = \frac{2\pi cn}{L - \hat{x}_m} = \frac{2\pi cn}{L} \frac{1}{1 - \frac{\hat{x}_m}{L}} \\
&= \omega_c \left(1 + \frac{\hat{x}_m}{L} + \mathcal{O}\left(\frac{\hat{x}_m}{L}\right)^2 \right) \\
&\approx \omega_c + \frac{\omega_c}{L} \hat{x}_m
\end{aligned} \tag{5.18}$$

This first order approximation produces an additional term in the Hamiltonian

$$H = \hbar(\omega_c - g_0 \hat{x}_m) \left(\hat{c}^\dagger \hat{c} + \frac{1}{2} \right), \tag{5.19}$$

which describes the interaction between the cavity field and the mechanical motion of the optomechanical mirror. The coupling term g_0 describes the change in resonance frequency of a resonator due to inter-

action with one single photon. In a cavity with length L this coupling is given by $g_0 = \frac{\omega_c}{L} x_{zp}$. The complete optomechanical system is then described by

$$
\begin{aligned}
H =& \hbar\omega_c \left(\hat{c}^\dagger \hat{c} + \frac{1}{2} \right) + \hbar\omega_m \left(\hat{b}^\dagger \hat{b} + \frac{1}{2} \right) \\
& - \hbar g_0 \hat{c}^\dagger \hat{c} \hat{x}_m + i\hbar E \left(\hat{c}^\dagger e^{-i\omega_L t} + \hat{c} e^{i\omega_L t} \right).
\end{aligned}
\tag{5.20}
$$

We also added a driving laser field term with laser frequency ω_L and field intensity $|E| = \sqrt{P\kappa_c/\hbar\omega_L}$ with a given input amplitude P and the cavity linewidth κ_c. We take the unitary transformation $U = e^{i\omega_L \hat{c}^\dagger \hat{c} t}$ into the rotating frame of the input laser frequency and the Hamiltonian operator becomes time invariant

$$
H = \hbar\Delta \left(\hat{c}^\dagger \hat{c} + \frac{1}{2} \right) + \hbar\omega_m \left(\hat{b}^\dagger \hat{b} + \frac{1}{2} \right) - \hbar g_0 \hat{c}^\dagger \hat{c} \hat{x}_m + i\hbar E \left(\hat{c}^\dagger + \hat{c} \right)
\tag{5.21}
$$

where $\Delta = \omega_c - \omega_L$ is the detuning between the input field and the cavity field.

We focus on the interaction term between the cavity field and mechanical oscillator

$$
H^{int} = \hbar g_0 \hat{c}^\dagger \hat{c} \hat{x}_m,
\tag{5.22}
$$

which describes the radiation pressure coupling in a third-order nonlinear process. The intensity of the light field couples to the amplitude of the mechanical oscillator and imprints a change of the cavity length. This is an intensity dependent phase change comparable to optical Kerr media where an intensity dependent refractive index causes a phase difference in the optical field.

For the treatment of quantum noise contributions to this coupling we linearize the system by splitting the cavity field into a real static part $\langle \hat{c} \rangle = \alpha_c$ and a fluctuation term $\delta\hat{c}$

$$
\begin{aligned}
H^{int} &= \hbar g_0 (\alpha_c + \delta\hat{c})^\dagger (\alpha_c + \delta\hat{c}) \hat{x}_m \tag{5.23} \\
&= \hbar g_0 \hat{x}_m \left(|\alpha_c|^2 + (\alpha_c \delta\hat{c}^\dagger + \alpha_c \delta\hat{c}) + \mathcal{O}(\delta\hat{c}^2) \right). \tag{5.24}
\end{aligned}
$$

We can eliminate static radiation pressure effects proportional to $|\alpha_c|^2$ with a controller stabilizing the cavity length. We assume $\alpha_c \gg \delta\hat{c}$ so that contributions of $\mathcal{O}(\delta\hat{c})^2$ can be neglected. The interaction Hamiltonian becomes

$$
\begin{aligned}
H^{int} &= \hbar\alpha_c g_0 \left(\delta\hat{c}^\dagger + \delta\hat{c}\right)\hat{x}_m \\
&= \frac{\hbar g}{2}\left(\delta\hat{c}^\dagger + \delta\hat{c}\right)\left(\hat{b} + \hat{b}^\dagger\right) \\
&= \frac{\hbar g}{2}\left(\delta\hat{c}^\dagger\hat{b} + \delta\hat{c}\hat{b}^\dagger\right) + \frac{\hbar g}{2}\left(\delta\hat{c}\hat{b} + \delta\hat{c}^\dagger\hat{b}^\dagger\right),
\end{aligned}
\tag{5.25}
$$

with the new coupling coefficient $g = \sqrt{2}\alpha_c g_0$. The Kerr-like interaction term from Eq. (5.22) is now replaced by two second-order terms. The first can be understood as a beamsplitter like interaction: one cavity photon is annihilated while one mechanical phonon is created, and vice versa. This interaction can be used for optomechanical cooling of the resonator. The average phonon number $\bar{n}_m = \frac{k_B T}{\hbar\omega_m}$ is higher than the average photon number $\bar{n}_c = \frac{k_B T}{\hbar\omega_c} = 0$ due to $\omega_c \gg \omega_m$. For the sideband resolved regime $\kappa_c/\omega_m \geq 1$ it is possible to cool the resonator to the ground state [72].

The second term of the interaction Hamiltonian has the form of a parametric effect. A phonon and a photon are created or annihilated at the same time. This can be understood as a squeezing operator, and we can produce ponderomotive squeezing, mechanical lasing or even entanglement of massive objects [73, 74, 75]. These effects are feasible in the strong coupling regime, when the coupling constant g is greater than the mechanical γ_m and optical κ_c losses of the system.

5.4 Equations of motion

With the linearized interaction Hamiltonian Eq. (5.25) put into the system Hamiltonian Eq. (5.21) we can derive the equations of motion for the system without detuning ($\Delta = 0$) via

$$
\dot{\hat{x}} = \frac{i}{\hbar}[H,\hat{x}], \qquad \dot{\hat{p}} = \frac{i}{\hbar}[H,\hat{p}]
\tag{5.26}
$$

If we drop the static driving field, the equations of motion become

$$\dot{\hat{x}}_\mathrm{c} = 0 \tag{5.27}$$

$$\dot{\hat{p}}_\mathrm{c} = g\hat{x}_\mathrm{m} \tag{5.28}$$

$$\dot{\hat{x}}_\mathrm{m} = \omega_\mathrm{m}\hat{p}_\mathrm{m} \tag{5.29}$$

$$\dot{\hat{p}}_\mathrm{m} = -\omega_\mathrm{m}\hat{x}_\mathrm{m} - g\hat{x}_\mathrm{c}. \tag{5.30}$$

The optomechanical system can be understood as a force detector where a force F couples to the phase quadrature of the mechanical resonator. This signal is masked by a thermal Langevin force F_T in the high-temperature limit and is assumed to be white. Additionally, we add a viscous damping factor γ_m to the equations of motion.

Losses are added by coupling vacuum noise into the loss channels of the resonator $\hat{x}_\mathrm{c}^\mathrm{in}$ and $\hat{p}_\mathrm{c}^\mathrm{in}$; another loss channel is the cavity decay rate described by the cavity linewidth κ_c. The overall equations of motion including losses, damping and thermal noise are

$$\dot{\hat{x}}_\mathrm{c} = -\frac{\kappa_\mathrm{c}}{2}\hat{x}_\mathrm{c} - \sqrt{\kappa_\mathrm{c}}\hat{x}_\mathrm{c}^\mathrm{in} \tag{5.31}$$

$$\dot{\hat{p}}_\mathrm{c} = -\frac{\kappa_\mathrm{c}}{2}\hat{p}_\mathrm{c} + g\hat{x}_\mathrm{m} - \sqrt{\kappa_\mathrm{c}}\hat{p}_\mathrm{c}^\mathrm{in} \tag{5.32}$$

$$\dot{\hat{x}}_\mathrm{m} = \omega_\mathrm{m}\hat{p}_\mathrm{m} \tag{5.33}$$

$$\dot{\hat{p}}_\mathrm{m} = -\omega_\mathrm{m}\hat{x}_\mathrm{m} - \gamma_\mathrm{m}\hat{p}_\mathrm{m} - g\hat{x}_\mathrm{c} + \sqrt{\gamma_\mathrm{m}}(f_T + F). \tag{5.34}$$

It is easy to see that a force (signal or radiation pressure) which is acting on the mirror couples into the impulse of the mechanical oscillator. The impulse changes the position of the mirror which has a direct coupling to the phase quadrature. We can measure the force in the output phase quadrature following the input-ouput formalism [50]

$$X^\mathrm{out} = X^\mathrm{in} + \sqrt{\kappa}X \tag{5.35}$$

and we obtain the noise spectral density for the phase quadrature

$$S_{XX}^2\delta(\omega - \omega') = \frac{1}{2}\left(\langle X(\omega)X(-\omega')\rangle + c.c.\right) \tag{5.36}$$

To derive the coupling into the output quadratures we solve the equations of motion in Fourier space using the transformation

$$x(\omega) = \frac{1}{\sqrt{2\pi}} \int x(t) e^{-i\omega t} \mathrm{d}t, \tag{5.37}$$

with the convenient fact that $\dot{x}(t) \to i\omega x(\omega)$. We define the mechanical susceptibility χ_m such that $\hat{x}_\mathrm{m} = \chi_\mathrm{m}\sqrt{\gamma_\mathrm{m}}(f_\mathrm{T} + F)$

$$\chi_\mathrm{m}(\omega) = \frac{\omega_\mathrm{m}}{\omega^2 - \omega_\mathrm{m}^2 + i\gamma_\mathrm{m}\omega}, \tag{5.38}$$

and the optical analog χ_c, which fulfills $\hat{x}_\mathrm{c} = \chi_\mathrm{c}\sqrt{\kappa_\mathrm{c}}\hat{x}_\mathrm{c}^\mathrm{in}$

$$\chi_\mathrm{c}(\omega) = \frac{1}{i\omega + \kappa_\mathrm{c}/2}. \tag{5.39}$$

Using the susceptibilities we can transfer the input noise contributions to the field quadratures of the system. These can then be measured in the output quadrature to obtain an overall spectral noise density of the system.

We have shown that the quantum mechanical optomechanical oscillator dynamics can be linearized into a formulation which looks like an optical beamsplitter and an optical down conversion process. These processes introduce noise in the output phase quadrature of the system due to amplitude fluctuations of the carrier light field. This aspect of the optomechanical oscillator is addressed by the proposal of Tsang [43] to set up an optical anti-noise path inside the optomechanical cavity to cancel out the quantum radiaton pressure noise coherently. With the tools obtained in the chapters Ch. 2 to Ch. 5 we will recapitulate the proposal by Tsang in Ch. 6 and calculate a set of parameters for a first proof-of-principle experiment in CQNC.

CHAPTER 6

A theoretical approach towards a coherent quantum noise cancellation experiment

We have mentioned different schemes to reduce or evade backaction noise in interferometric measurements in Ch. 1. In this chapter we recapitulate the coherent quantum noise cancellation (CQNC) scheme introduced by Tsang and Caves [43] and expand the description to develop an experimental realization of CQNC. The idea of the CQNC scheme is based on an all-optical setup where a second, auxiliary cavity is coupled to an optomechanical cavity, subject to quantum radiation pressure noise where both cavities are driven by the same amplitude noise (see Fig. 6.1). The optomechanical cavity will introduce backaction phase noise into the measurement. The ancilliary optical system will act like a mechanical oscillator with equal effective mass in magnitude as the optomechanical mirror but with an opposite sign. The displacement of the ancilliary system introduced by amplitude fluctuations will then be equal but opposite in sign to the phase shifts of the optomechanical system. The two oppositely directed phase shifts will cancel each other exactly.

We have investigated the theoretical approach in more detail regarding an all-optical realization of the CQNC scheme by Tsang and Caves [43].
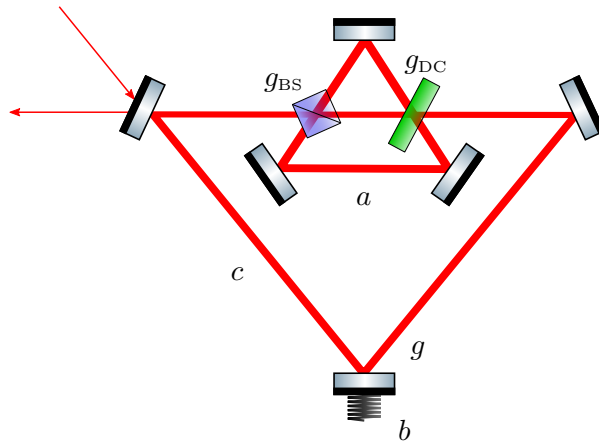
FIGURE 6.1: Theoretical CQNC Scheme by Tsang and Caves [43]. The me-
ter cavity c is coupled to the ancilla cavity a via a nonlinear medium and
a beamsplitter with the coupling strengths g_{DC} and g_{BS}. This cancels the
backaction noise introduced by the mechanical oscillator b with the optome-
chanical coupling strength g.

For ideal conditions the mechanical oscillator and the ancilla system
should be equally but oppositely susceptible to amplitude fluctuations
of light. In the paper by Tsang and Caves [43] the lossless case is consid-
ered, as well as the possibility of perfect matching of all experimental
parameters. It is unfortunately not possible to fulfill these conditions
exactly in a realistic experiment. We discuss the conditions for an ex-
periment under realistic assumptions in this chapter. We calculate the
parameters CQNC for the ideal case where the matching conditions
are met, assuming no losses, and compare these with the consequences
of imperfect matching of mechanical oscillator and ancilla system. We
present a set of experimental parameters for a first proof-of-principle
experiment showing the effects of CQNC. The results presented in this
chapter were published by Wimmer *et al.* in [76] and are the basis for
the experiments done in Ch. 7. The plots in this chapter were gener-
ated with Mathematica® code which was developed together with the
authors of the paper [76] and can be also found in [77].

6.1 Optomechanical force sensing

We consider an optomechanical oscillator as introduced in Ch. 5. Its position x_m and momentum p_m obey

$$\dot{x}_\mathrm{m} = \frac{p_\mathrm{m}}{m} \tag{6.1}$$

$$\dot{p}_\mathrm{m} = -m\omega_\mathrm{m}^2 x_\mathrm{m} - \gamma_\mathrm{m} p_\mathrm{m} + f_T + F(t). \tag{6.2}$$

The force $F(t)$ is to be detected by the oscillator. f_T is the thermal Langevin force which we assume to be white such that

$$\langle f_T(t) f_T(t') \rangle = 2\gamma_m k_B T \delta(t - t'). \tag{6.3}$$

We describe the system with dimensionless position and momentum variables $\hat{x}_\mathrm{m} = x_\mathrm{m}/x_{zp}$ and $\hat{p}_\mathrm{m} = p_\mathrm{m} x_{zp}/\hbar$ with $[\hat{x}_\mathrm{m}, \hat{p}_\mathrm{m}] = 1$ (compare Eq. (5.14), Eq. (5.13)) and the corresponding scaled force operators $\hat{f}_T = f_T/\sqrt{\hbar m \gamma_\mathrm{m} \omega_\mathrm{m}}$ and $\hat{F} = F/\sqrt{\hbar m \gamma_\mathrm{m} \omega_\mathrm{m}}$

$$\dot{\hat{x}}_\mathrm{m} = \omega_\mathrm{m} \hat{p}_\mathrm{m} \tag{6.4}$$

$$\dot{\hat{p}}_\mathrm{m} = \omega_\mathrm{m} \hat{x}_\mathrm{m} - \gamma_\mathrm{m} \hat{p}_\mathrm{m} + \sqrt{\gamma_\mathrm{m}}(\hat{f}_T + \hat{F}). \tag{6.5}$$

As shown in Ch. 5 the force on the optomechanical mirror inside an optical cavity can be sensed with an optical readout. The cavity is described with the quadrature operators $\hat{x}_\mathrm{c}$ and $\hat{p}_\mathrm{c}$ (see Eq. (2.23)). The force operator $\hat{F}(t)$ acts on the position operator of the mirror which couples into the phase operator of the carrier light field of the optical cavity $\hat{x}_\mathrm{c}$. This phase change can be detected by a homodyne detector measurement in reflection of the cavity. The Hamiltonian for the coupled system in the rotating frame of the carrier frequency is given by

$$H = \hbar\omega_\mathrm{m} \hat{b}^\dagger \hat{b} + \hbar g \hat{x}_\mathrm{c} \hat{x}_\mathrm{m} \tag{6.6}$$

and the corresponding equations of motion are

$$\dot{\hat{x}}_c = -\frac{\kappa_c}{2}\hat{x}_c - \sqrt{\kappa_c}\hat{x}_c^{in} \tag{6.7}$$

$$\dot{\hat{p}}_c = -\frac{\kappa_c}{2}\hat{p}_c + g\hat{x}_m - \sqrt{\kappa_c}\hat{p}_c^{in} \tag{6.8}$$

$$\dot{\hat{x}}_m = \omega_m\hat{p}_m \tag{6.9}$$

$$\dot{\hat{p}}_m = -\omega_m\hat{x}_m - \gamma_m\hat{p}_m - g\hat{x}_c + \sqrt{\gamma_m}(\hat{f}_T + \hat{F}). \tag{6.10}$$

This set of linear equations can be solved in Fourier space (see Eq. (5.37))
and gives the output phase quadrature of the cavity in frequency space

$$\hat{p}_c^{out} = e^{i\phi}\hat{p}_c^{in} + \sqrt{\gamma_m G}\chi_m[\hat{f}_T + \hat{F}] \\ + G\chi_m\hat{x}_c^{in}, \tag{6.11}$$

where $e^{i\phi} = (i\omega - \frac{\kappa_c}{2})/(i\omega + \frac{\kappa_c}{2})$. We introduced the effective measurement strength G for the case where $\kappa_c \gg \omega$

$$G = \frac{4g^2}{\kappa_c} = \left(\frac{2}{\pi}\right)^2 \frac{\omega_c \mathcal{F}_c P}{\omega_m m c^2}. \tag{6.12}$$

Here $\mathcal{F}_c = \pi c/\kappa_c L_c$ is the finesse of the meter cavity (see Eq. (4.12))
and P is the input power of the carrier light. The susceptibilities are
the ones given in Eq. (5.38). The four terms in Eq. (6.11) contributing to
the phase output quadrature are from left to right: the phase shot noise
of light, the thermal Brownian noise from Brownian motion, the signal
to be detected, and the backaction noise proportional to the amplitude
quadrature of the input field.

6.1.1 The standard quantum limit

We have introduced the standard quantum limit of interferometry in
Ch. 1. Analogously we can derive a standard quantum limit for the optomechanical cavity system. We consider the unbiased estimator $\bar{F}(\omega)$
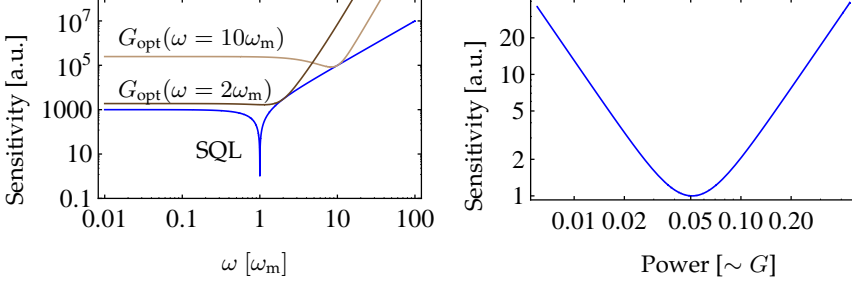
FIGURE 6.2: Two ways to display the standard quantum limit of a mechanical oscillator. (a) Noise spectral density: the standard quantum limit is the lower sensitivity bound for all optimal powers. Two exemplary noise curves for a given power are drawn. (b) Noise density for a fixed measurement frequency ω: the quantum noise is minimized for an optimal power level G_{opt} for the given measurement frequency.

for the force measurement given by

$$\bar{F} = \frac{1}{\sqrt{\gamma_{\text{m}} G} \, \chi_{\text{m}}} p_{\text{c}}^{\text{out}} = \hat{F} + \hat{F}^{\text{add}}. \tag{6.13}$$

The added noise $\hat{F}^{\text{add}}(\omega)$ to the force measurement at detection frequency ω is

$$\hat{F}^{\text{add}} = \hat{f}_T + \frac{e^{i\phi}}{\sqrt{\gamma_{\text{m}} G} \, \chi_{\text{m}}} p_{\text{c}}^{\text{in}} + \sqrt{\frac{G}{\gamma_{\text{m}}}} x_{\text{c}}^{\text{in}}. \tag{6.14}$$

The noise contributions to the added noise are the thermal Langevin force, shot noise in the phase quadrature, and backaction noise from amplitude noise.

The sensitivity of the force measurement in the phase quadrature is defined by the power spectral density of the added noise

$$S_F(\omega)\delta(\omega - \omega') = \frac{1}{2}\langle \hat{F}^{\text{add}}(\omega)\hat{F}^{\text{add}}(-\omega')\rangle + \text{c.c.}$$

We insert Eq. (6.14) into this and get the noise spectral density

$$S_F = \frac{k_B T}{\hbar \omega_{\text{m}}} + \frac{1}{2\gamma_{\text{m}} G |\chi_{\text{m}}|^2} + \frac{G}{2\gamma_{\text{m}}}. \tag{6.15}$$

Above we have introduced the scaled force operators. Therefore we
must multiply the dimensionless noise spectral density with the scaling factor such that we get the force noise spectral density
$S_F(\omega) = \hbar m \gamma_m \omega_m S_F(\omega)$ shown in Fig. 6.2. As we can see from Eq. (6.15),
the first term connected with Brownian motion is independent of the
measurement strength and gives a spectrally flat background. The second term which is due to phase noise has a contribution that is inversely proportional to the overall noise, while the amplitude noise
scales proportionally with the power.

We can derive an optimal value for G such that S_F is minimized and
we reach a lower bound for the achievable sensitivity called the *standard quantum limit* (SQL) of continuous force sensing

$$S_F(\omega) \geq \frac{1}{\gamma_m |\chi_m(\omega)|} \equiv S_{\mathrm{SQL}}(\omega). \qquad (6.16)$$

With this result we can calculate the optimal power G_{SQL} for any given
measurement frequency ω of the system

$$G_{\mathrm{SQL}}(\omega) = \frac{1}{|\chi_m(\omega)|}. \qquad (6.17)$$

6.2 Ideal CQNC

According to the proposal by Tsang ánd Caves [43] we add an antinoise
path to the optomechanical cavity by coupling a second cavity (ancilla
cavity) to the meter cavity using a beamsplitter and a down-conversion
process. The quadrature operators describing the ancilla cavity are $\hat{x}_a$,
$\hat{p}_a$ (see Eq. (2.23)). Tuned approriately the ancilla cavity can proviede
an interaction that acts as an antinoise process cancelling out the back-
action effects of the mechanical oscillator which we showed in Ch. 5.
The Hamiltonian of the system then becomes

$$H = -\Delta_a a^\dagger a + g \hat{x}_c \hat{x}_m + g_{\mathrm{BS}}(ac^\dagger + a^\dagger c) + g_{\mathrm{DC}}(ac + a^\dagger c^\dagger). \qquad (6.18)$$

We remain in the rotating frame at the resonance frequency of the me-
ter cavity ω_c. The detuning between ancilla cavity and meter cavity is
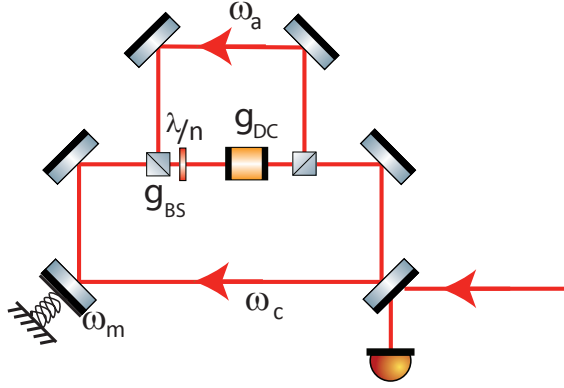
FIGURE 6.3: A more realistic experimental realization of CQNC. The meter cavity is coupled to the ancilla cavity via a down-conversion (DC) process and a polarizing beamsplitter (PBS) providing backaction cancellation.

given by $\Delta_a = \omega_c - \omega_a$. The last two terms of Eq. (6.18) describe the coupling of the ancilla cavity to the meter cavity with a passive beamsplitter coupling and an active down-conversion through an OPO process. A schematic of this cavity setup is shown in Fig. 6.3. The passive beamsplitter coupling strength is given by $g_{BS} = rc/L$ with r being the beamsplitter reflectivity and L being the (equal) length of ancilla and meter cavity. The nonlinear coupling strength is $g_{DC} = \Gamma lc/L$ [78] with the crystal length l and the gain parameter [79]

$$\Gamma = \sqrt{\frac{2\omega_1\omega_2 d_{\text{eff}}^2 I_{\text{pump}}}{n_1 n_2 n_3 \epsilon_0 c^3}}, \tag{6.19}$$

where ω_1 and ω_2 are the interacting light frequencies, d_{eff} is the nonlinear coefficient, I_{pump} is the pump intensity and n_i are the refractive indices of the respective light fields inside the crystal.

With the ancilla cavity the equations of motion expand to

$$\dot{x}_c = -\frac{\kappa_c}{2}\hat{x}_c + (g_{BS} - g_{DC})p_a - \sqrt{\kappa_c}\hat{x}_c^{in}, \tag{6.20}$$

$$\dot{p}_c = -\frac{\kappa_c}{2}\hat{p}_c - (g_{BS} + g_{DC})\hat{x}_a - g\hat{x}_m - \sqrt{\kappa_c}\hat{p}_c^{in}, \tag{6.21}$$

$$\dot{x}_a = -\frac{\kappa_a}{2}\hat{x}_a - \Delta\hat{p}_a + (g_{BS} - g_{DC})\hat{p}_c - \sqrt{\kappa_a}\hat{x}_a^{in}, \tag{6.22}$$

$$\dot{p}_a = -\frac{\kappa_a}{2}\hat{p}_a + \Delta\hat{x}_a - (g_{BS} + g_{DC})\hat{x}_c - \sqrt{\kappa_a}\hat{p}_a^{in}, \tag{6.23}$$

$$\dot{x}_m = \omega_m\hat{p}_m, \tag{6.24}$$

$$\dot{p}_m = -\omega_m\hat{x}_m - \gamma_m\hat{p}_m - g\hat{x}_c + \sqrt{\gamma_m}(f + F). \tag{6.25}$$

Here we introduced the decay rate κ_a of the ancilla cavity. For a coupling of the ancilla cavity to the meter cavity with ideally fulfilled matching conditions

$$g_{BS} = g_{DC} \qquad \text{and} \qquad g = g_{BS} + g_{DC}. \tag{6.26}$$

the amplitude quadrature of the meter cavity x_c couples *identically* to p_a and p_m *only* (and *not* to $\hat{x}_a$). The equations of motion for the phase quadrature of ancilla cavity and the mechanical oscillator then become

$$\dot{p}_a = -\frac{\kappa_a}{2}\hat{p}_a + \Delta\hat{x}_a - g\hat{x}_c \tag{6.27}$$

$$\dot{p}_m = -\omega_m\hat{x}_m - \gamma_m\hat{p}_m - g\hat{x}_c + \sqrt{2\gamma_m}(\hat{f} + \hat{F}), \tag{6.28}$$

while the backcoupling into the amplitude quadratures of ancilla and meter cavity is cancelled out.

We solve the equations of motion (Eq. (6.20) to Eq. (6.25)) to obtain the output phase quadrature

$$\hat{p}_c^{out} = e^{i\phi}\hat{p}_c^{in}$$
$$+ \sqrt{\gamma_m G}\chi_m[\hat{f}_T + \hat{F}] - \sqrt{2\kappa_a G}\chi_a\left[\frac{i\omega + \kappa_a/2}{-\Delta_a}\hat{x}_a^{in} + \hat{p}_a^{in}\right] \tag{6.29}$$
$$+ G\left[\chi_m + \chi_a\right]\hat{x}_c^{in}.$$

Here we have introduced the susceptibility of the ancilla cavity χ_a, defined similarly to the other susceptibilities in the system

$$\chi_a(\omega) = \frac{-\Delta_a}{(\omega^2 - \Delta_a^2 - \frac{\kappa_a^2}{4}) - i\omega\kappa_a}. \tag{6.30}$$

The addition of the ancilla cavity to the system has two effects on the measurement of the output phase:

Firstly the backaction term now depends on the difference between the mechanical susceptibility and that of the ancilla cavity. If we are able to tune the susceptibilities to be equal, we can interfere the backaction effects destructively, which increases the sensitivity of the force measurement.

Secondly the second new term is an additional noise term which contributes to shot noise of the ancilla cavity which is coupled to the phase quadrature of the meter cavity. The overall added noise of the system then becomes

$$\begin{aligned}
\hat{F}^{\text{add}} = \hat{f}_T &+ \frac{e^{i\phi}}{\sqrt{\gamma_m G}\,\chi_m}\hat{p}_c^{\text{in}} \\
&- \sqrt{\frac{2\kappa_a}{\gamma_m}}\frac{\chi_a}{\chi_m}\left[\frac{i\omega + \kappa_a/2}{-\Delta_a}\hat{x}_a^{\text{in}} + \hat{p}_a^{\text{in}}\right] \\
&+ \sqrt{\frac{G}{\gamma_m}}\frac{\chi_m + \chi_a}{\chi_m}\hat{x}_c^{\text{in}}.
\end{aligned} \tag{6.31}$$

The last term in Eq. (6.31) corresponding to backaction noise vanishes if the conditions are such that $\chi_m = -\chi_a$, or

$$\frac{\omega_m}{\omega^2 - \omega_m^2 - i\omega\gamma_m} = \frac{-\Delta_a}{\omega^2 - \Delta_a^2 - \frac{\kappa_a^2}{2} - i\omega\kappa_a}. \tag{6.32}$$

This leads to the following requirements for ideal backaction noise cancellation:

(*i*) The detuning between the ancilla and meter cavities must match the mechanical resonance frequency

$$\Delta_a = \omega_m. \tag{6.33a}$$

(*ii*) The ancilla cavity linewidth matches that of the mechanical oscilla-
tor

$$\kappa_{\mathrm{a}} = \gamma_{\mathrm{m}}. \tag{6.33b}$$

(*iii*) And the detuning is much larger than the cavity linewidth

$$|\Delta_{\mathrm{a}}| \gg \kappa_{\mathrm{a}}. \tag{6.33c}$$

Conditions (*i*) and (*ii*) together imply both the resolved sideband limit

$$\omega_{\mathrm{m}} \gg \kappa_{\mathrm{a}}, \tag{6.33d}$$

and a large mechanical quality factor,

$$Q_{\mathrm{m}} = \omega_{\mathrm{m}}/\gamma_{\mathrm{m}} \gg 1. \tag{6.33e}$$

While it is clear from experimental experience that these conditions
cannot be met perfectly, we assume (for now) ideal conditions such that
Eq. (6.32) is fulfilled and the backaction term in Eq. (6.31) vanishes. For
a solely quantum noise limited system the added noise consists only
of shot noise in the measured phase quadrature and shot noise intro-
duced through the ancilla cavity, and the power noise spectral density
then becomes

$$S_F = \frac{1}{2\gamma_{\mathrm{m}}G|\chi_{\mathrm{m}}|^2} + \frac{\kappa_{\mathrm{a}}|\chi_{\mathrm{a}}|^2}{\gamma_{\mathrm{m}}|\chi_{\mathrm{m}}|^2}\left[\frac{\omega^2 + (\kappa_{\mathrm{a}}/2)^2}{\Delta^2} + 1\right]. \tag{6.34}$$

The first term of S_F describing the shot noise contribution scales with
P^{-1} and is negligible for sufficiently large power. We can then derive a
lower bound for the sensitivity achievable with this coherent quantum
noise cancellation scheme:

$$S_F(\omega) \geq \frac{\omega^2 + \omega_{\mathrm{m}}^2 + \gamma_{\mathrm{m}}^2/4}{\omega_{\mathrm{m}}^2} \equiv S_{\mathrm{CQNC}}(\omega). \tag{6.35}$$

In Fig. 6.4a the noise power spectral density is drawn for optimal
values of G for any given measurement frequency. One can see that on
resonance no enhancement in sensitivity compared to the SQL can be
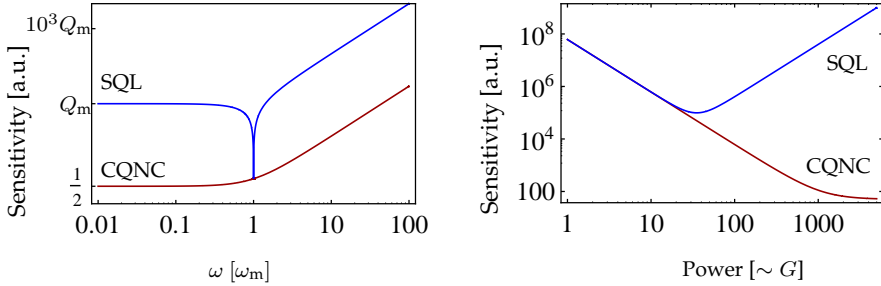
FIGURE 6.4: Sensitivity with ideal CQNC. (a) Noise spectral density: at frequencies off the mechanical resonance the quantum noise is reduced by a factor of $1/2Q_{\mathrm{m}}$ below the SQL. On resonance no improvement is possible. (b) Noise density for a fixed measurement frequency: above the optimal power level for the SQL the curve is not limited by backaction noise but reaches a plateau induced by the ancilla cavity. Plot parameters in Table 6.1.

achieved. Off resonance it is possible to increase the sensitivity proportional to Q_{m}^{-1}

$$S_{\mathrm{CQNC}} = \frac{1}{2Q_{\mathrm{m}}} S_{\mathrm{SQL}}. \tag{6.36}$$

The second plot (Fig. 6.4b) shows the noise density at a measurement frequency of $\omega = 10\,\omega_{\mathrm{m}}$. For powers above the optimal value G_{opt} of the SQL the sensitivity can be increased by means of the CQNC scheme.

6.3 Nonideal CQNC

In the previous section we have considered the ideal case where all requirements for CQNC are met ideally. Perfect CQNC requires the matching of coupling strengths of the meter cavity to the mechanical oscillator and the ancilla cavity (see Eq. (6.26)), and matching of their respective susceptibilities (see Eq. (6.33)). We have however already determined that these conditions cannot be realistically fulfilled. This raises the question what the tolerance is to violations of these conditions, and what the price is for a given mismatch. In particular matching the linewidth of the ancilla cavity to that of a high-quality mechanical oscillator appears to be very challenging, and can not be ful-
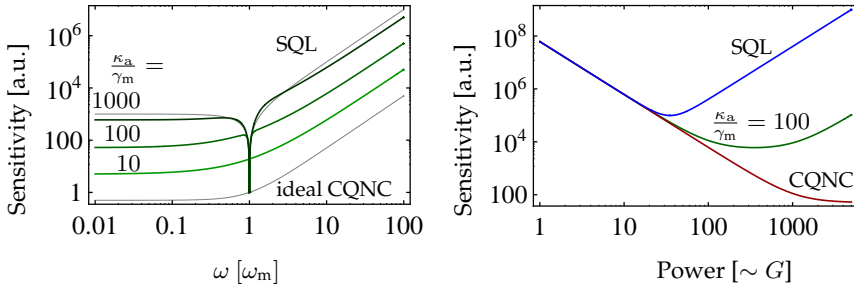
FIGURE 6.5: Ideal and nonideal CQNC. (a) Noise spectral density: The contribution of backaction noise rises with growing ratio of κ_a/γ_m. Thin gray lines are the SQL and ideal CQNC. (b) Noise density for a fixed measurement frequency: Like for the SQL we can find an optimal power for nonideal κ_a. This level is still below the level of SQL for $\kappa_a < \omega_m$. Plot parameters in Table 6.1.

filled without some compromise. After all, if the ultimate goal is to achieve backaction cancellation only within a certain frequency bandwidth, and not over the entire spectrum, it might in fact be advantageous to give up one of the conditions and impose Eq. (6.33) only for the relevant frequencies. The question is how robust these requirements are to violation, as it is clear that we cannot achieve perfect matchings of the coupling strengths of the mechanical oscillator and the ancilla cavity.

6.3.1 Nonideal ancilla cavity linewidth

The most challenging requirement for ideal CQNC is the matching of the ancilla cavity linewidth to that of the mechanical oscillator. As the gain in sensitivity is proportional to the quality factor of the mechanical oscillator we expect very low mechanical linewidths γ_m to be present in the optomechanical system. We know from Eq. (4.11) that the ancilla cavity linewidth depends on reflectivities, losses and the cavity length. The schematic in Fig 6.3 shows that additional intracavity optics are needed. These introduce unavoidable losses which limit the resulting cavity linewidth. For a tabletop experiment we must therefore assume

that $\kappa_a \gg \gamma_m$, and we get the corresponding power spectral density

$$
\begin{aligned}
S_F = {} & \frac{1}{2\gamma_m G |\chi_m|^2} + \frac{\kappa_a |\chi_a|^2}{\gamma_m |\chi_m|^2} \left[\frac{\omega^2 + (\kappa_a/2)^2}{\Delta^2} + 1 \right] \\
& + \frac{G}{2\gamma_m} \left| \frac{\chi_m + \chi_a}{\chi_m} \right|^2 .
\end{aligned}
\tag{6.37}
$$

We assume a cryogenic environment and neglect thermal noise contributions to be quantum noise limited. In contrast to ideal CQNC the difference of susceptibilities in the last term of Eq. (6.37) does not vanish anymore, which increases the noise due to imperfect matching of linewidths. Again we can derive a minimal spectral density achieved for optimal power,

$$
S_F = \frac{|\chi_m + \chi_a|}{\gamma_m |\chi_m|^2} + \frac{\kappa_a |\chi_a|^2}{\gamma_m |\chi_m|^2} \left[\frac{\omega^2 + (\kappa_a/2)^2}{\Delta^2} + 1 \right] .
$$

We have shown earlier that on resonance no noise reduction can be achieved even for ideal CQNC. For frequencies off resonance the second term (due to noise introduced by the ancilla cavity) dominates over the first term (measurement shot and backaction noise). The ratio between SQL and the nonideal added noise S_F yields

$$
S_F = \frac{\kappa_a}{2\omega_m} \times S_{\text{SQL}}
\tag{6.38}
$$

for the high-frequency limit. This results in the constraint $\kappa_a < 2\omega_m$ for the ancilla cavity linewidth. In the low-frequency limit the constraints to the ancilla cavity linewidth are more relaxed as the ratio between SQL and S_F is

$$
S_F = \frac{\kappa_a}{\gamma_m} \frac{(\gamma_m^2 + 4\omega_m^2)(\kappa_a + 2\omega_m)}{(\gamma_m + 2\omega_m)(\kappa_a^2 + 4\omega_m^2)} .
\tag{6.39}
$$

For $\kappa_a < \omega_m$ this converges to the values in Eq. (6.38) (see Fig. 6.6). For $\kappa_a \gg \omega_m$ the curve converges to the SQL for low frequencies while the added noise is increased in the high-frequency limit.
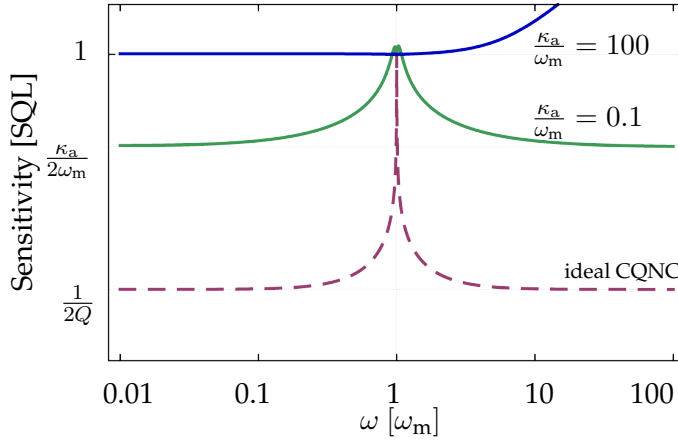
FIGURE 6.6: Noise spectral density normalized to the SQL. We see the ideal
CQNC noise reduction of $1/2Q$, the nonideal CQNC due to the ancilla cav-
ity linewidth of $\kappa_\mathrm{a} = 0.1\omega_\mathrm{m}$. The effect of CQNC vanishes in the low-
frequency limit for $\kappa_\mathrm{a} > \omega_\mathrm{m}$ and in the high-frequency limit the sensitivity
is worse than the SQL.

6.3.2 Imperfect matching of couplings

The other important restriction is the matching of the beamsplitter and
down-conversion coupling to that of the mechanical oscillator. It is
likely that a perfect match between these couplings is experimentally
not realizable and we have to take a certain mismatch into account.
If the conditions in Eq. (6.33) are not fulfilled, the equations of motion
will not reduce to the form of Eq. (6.27). The analytical solution of these
equations is not trivial anymore, and we discuss the results with plots
generated from the computationally solved equations.
The solution of the equations is done with the matrix-form

$$\dot{\vec{x}} = M\vec{x} + A\vec{x}_\mathrm{in}. \tag{6.40}$$

with the quadrature vectors for input-, output- and field-quadratures

$$
\vec{x} = \begin{pmatrix} \hat{x}_c \\ \hat{p}_c \\ \hat{x}_a \\ \hat{p}_a \\ \hat{x}_m \\ \hat{p}_m \end{pmatrix}, \quad \vec{x}_{\text{in}} = \begin{pmatrix} \hat{x}_c^{\text{in}} \\ \hat{p}_c^{\text{in}} \\ \hat{x}_a^{\text{in}} \\ \hat{p}_a^{\text{in}} \\ 0 \\ \hat{f} + \hat{F} \end{pmatrix}, \quad \vec{x}_{\text{out}} = \begin{pmatrix} x_c^{\text{out}} \\ p_c^{\text{out}} \\ x_a^{\text{out}} \\ p_a^{\text{out}} \\ x_m^{\text{out}} \\ p_m^{\text{out}} \end{pmatrix}, \quad (6.41)
$$

the noise matrix A

$$
A = \text{diag}(-\sqrt{\kappa_c}, -\sqrt{\kappa_c}, -\sqrt{\kappa_a}, -\sqrt{\kappa_a}, 0, \sqrt{\gamma_m}). \quad (6.42)
$$

and the matrix $\mathcal{M}$ for the equations of motion

$$
\mathcal{M} = \begin{pmatrix} -\kappa_c/2 & 0 & 0 & g_{\text{BS}} - g_{\text{DC}} & 0 & 0 \\ 0 & -\kappa_c/2 & -g_{\text{BS}} - g_{\text{DC}} & 0 & -g & 0 \\ 0 & g_{\text{BS}} - g_{\text{DC}} & -\kappa_a/2 & -\Delta & 0 & 0 \\ -g_{\text{BS}} - g_{\text{DC}} & 0 & +\Delta & -\kappa_a/2 & 0 & 0 \\ 0 & 0 & 0 & 0 & 0 & \omega_m \\ -g & 0 & 0 & 0 & -\omega_m & -\gamma_m \end{pmatrix}.
$$

$$(6.43)$$

Again we solve the system with the input-output formalism [50] after moving to Fourier space (see Eq. (5.37)). With $\vec{x}_{\text{out}} = \vec{x}_{\text{in}} - A\vec{x}$ and $i\omega\vec{x} = \mathcal{M}\vec{x} + A\vec{x}_{\text{in}}$ we get

$$
\vec{x}_{\text{out}} = P\vec{x}_{\text{in}} \quad (6.44)
$$

with the system matrix P

$$
P = \mathbb{1} - A\frac{1}{i\omega - \mathcal{M}}A. \quad (6.45)
$$

The resulting spectral noise density S_{out} is
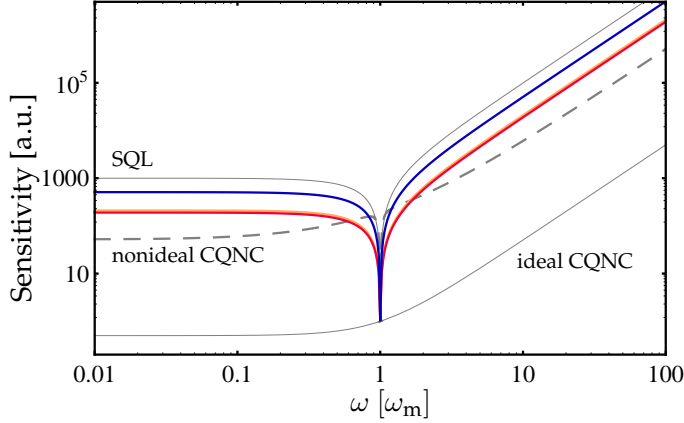
$$
S_{\text{out}} = PS_{\text{in}}P^T \quad (6.46)
$$

FIGURE 6.7: Sensitivity of CQNC with nonideal couplings with $\varepsilon_1 \neq 0$ respectively $g_{\mathrm{BS}} \neq g_{\mathrm{DC}}$ following Eq. (6.48) and Eq. (6.49). The curves are plotted for $\varepsilon_1 = \pm 0.1$ (orange) and $\varepsilon_1 = \pm 0.3$ (blue). The mismatch in couplings increases the noise of the nonideal CQNC for all frequencies with increased mismatch of the coupling strengths. The difference in the increased noise if $g_{\mathrm{BS}} > g_{\mathrm{DC}}$ or $g_{\mathrm{BS}} < g_{\mathrm{DC}}$ is negligible. Curves for SQL, ideal and nonideal CQNC are plotted in gray as an orientation. Parameters in Table 6.1

with the noise incoupling

$$S_{\mathrm{in}} = \frac{1}{2}\mathrm{diag}(1,1,1,1,0,2\bar{n}). \tag{6.47}$$

The measurement phase output quadrature is the $(2,2)$-element of S_{out}. We include the imperfect matching of couplings using

$$g_{\mathrm{BS}} = \frac{1}{2}g\left(1 + \varepsilon_1 + \varepsilon_2\right) \tag{6.48}$$

$$g_{\mathrm{DC}} = \frac{1}{2}g\left(1 + \varepsilon_1 - \varepsilon_2\right) \tag{6.49}$$

where ε_1 introduces a mismatch in the ratio $g_{\mathrm{BS}}/g_{\mathrm{DC}} = 1$ and ε_2 violates the condition $g_{\mathrm{BS}} + g_{\mathrm{DC}} = g$.

As a consequence of the results from the previous section we assume in addition to the imperfect couplings we are considering here a ratio of $\kappa_{\mathrm{a}}/\gamma_{\mathrm{m}}$ such that both conditions from Eq. (6.26) are violated. The resulting plots (see Fig. 6.7 and Fig. 6.7) show that for $\varepsilon_1 \neq 0$ the noise spectrum is increased for all frequencies. Stronger mismatches
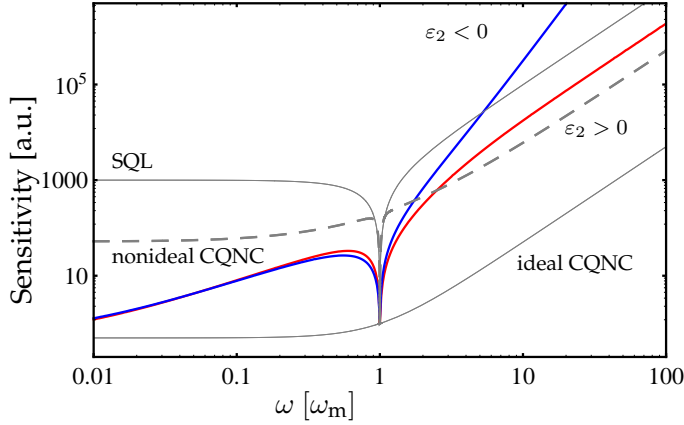
FIGURE 6.8: Sensitivity of CQNC with nonideal couplings with $\varepsilon_2 \neq 0$ respectively $g_{\text{BS}} + g_{\text{DC}} \neq g$ (see Eq. (6.48) and Eq. (6.49)). The curves are plotted for $\varepsilon_2 = \pm 0.3$. We see the dependance of the sensitivity to the sign of ε_2. For $\varepsilon_2 > 0$ (orange) we get a constant factor added to the overall noise. For $\varepsilon_2 < 0$ (blue) the overall noise is dominated by the mismatch for frequencies above the resonance. Curves for SQL, ideal and nonideal CQNC are plotted in gray as an orientation. Below the resonance the noniedeal case with mismatch approaches the value of ideal CQNC. Parameters in Table 6.1.

have a higher contribution to the noise. The increase in noise is not affected by the sign of ε_1.

For $\varepsilon_2 \neq 0$ we get a different behavior of the overall noise. Stronger mismatches give a higher noise contribution but the added noise is not constant in frequency. Below the resonance the noise converges towards the ideal CQNC sensitivity. For freqencies above the resonance the sensitivity depends on the sign of ε_2. A constant noise factor is added to the overall noise for $\varepsilon_2 > 0$. For $\varepsilon < 0$ the noise increases with increasing frequency and becomes the dominant noise source.

Fig. 6.9 shows the case where none of the three matching conditions is fulfilled. In the frequency regime below resonance the noise contribution from $\varepsilon_1 \neq 0$ is dominant. On resonance we are limited by the SQL. Above resonance the contribution from $\varepsilon_2 < 0$ is dominant and limits the sensitivity at high frequencies.
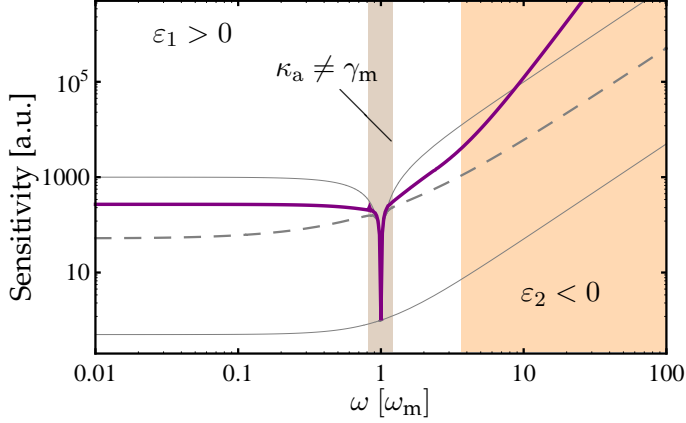
FIGURE 6.9: No matching condition is fulfilled. $\varepsilon_2 = 0.1$ limits the sensitivity
for the white area. Around the resonance frequency $\kappa_a = 100\gamma_m$ is limiting
and $\varepsilon_2 = -0.1$ dominates at high frequencies. Plot parameters in Table 6.1.

TABLE 6.1: Parameters used for generating the plots of this section.

ω	Fourier frequency	$10\,\omega_m$
g	Optomechanical coupling	ω_m
g_{BS}	Beamsplitter coupling	$g/2$
g_{DC}	Down-conversion coupling	$g/2$
κ_c	Meter cavity linewidth	$10\,\omega_m$
κ_a	Ancilla cavity linewidth	γ_m
Δ	Ancilla cavity detuning	$-\omega_m$
Q	Mechanical quality factor	1000
γ_m	Mechanical damping	$10^{-3}\,\omega_m$
ω_m	Mechanical resonance frequency	1

6.4 Experimental case study

In the preceding sections we have evaluated the effect of ideal CQNC as well as the effect of deviations to the ideal parameters. In this work we want to design a proof-of-principle experiment to Demonstrate the feasibility of CQNC. The matching conditions of the optical and optomechanical couplings can be translated into technical boundary conditions for the experiment. These boundary conditions lead us to the choice of the optomechanical oscillator, beamsplitter interaction and nonlinear crystal.

The proposed scheme calls for a nondegenerate nonlinear process and a beamsplitter coupling between the two cavities. This need limits the choice of technically suitable materials since the effect must be bidirectional for both elements. We can divide nondegenerate nonlinear processes into three different types.

The process can either be spatially nondegenerate, which could be realized using the walk-off inside a nonlinear medium. Using this technique the interaction length is limited and therefore limits the strength of the nonlinear process. In addition it is not possible to find a cavity geometry which realizes the backcoupling into the original cavity using the same process.

The second nondegenerate process makes use of the frequency nondegeneracy of squeezed fields. Frequency nondegenerate experiments with strong nonlinear coefficients have been shown by different groups [80, 81]. For our proposed scheme the limiting element is the beamsplitter. The interaction must not only be able to separate the different frequencies, but must couple the two cavities with each other. This is not possible with passive beamsplitters such as dichroic mirrors or comparable components.

This work concentrates on type-II processes with polarization nondegeneracy. When applied on the optical axis of a nonlinear medium no walk-off is present and the effect is bidirectional. For the beamsplitter coupling we can use conventional polarizing optics which couple the two cavities to each other. Since the two-mode field is frequency de-

generate we can achieve coupling for both the nonlinear and the beam-splitter interaction.

Recapitulating the requirements for CQNC we must match the suscep-tibilities and the strengths of the coupling processes in Eq. (6.26). The beamsplitter coupling is given by

$$g_{\mathrm{BS}} = \frac{rc}{L} \qquad (6.50)$$

with the reflectivity r in units of the rate photons are coupled from one resonator to the other. The length of the cavity is denoted with L and the speed of light with c. We have chosen a polarization non-degenerate process for the meter and ancilla cavity, therefore we use a PBS for the beamsplitter interaction. The reflectivity is tuned with a $\lambda/2$-waveplate. We assume that this combination sets a lower limit on the reflectivity at $0.5\,\%$, which must be controlled with an accuracy of $\pm 0.05\,\%$. This requirement is challenging but not restrictive. With these parameters the beamsplitter coefficient has a rate of $g_{\mathrm{BS}}/2\pi = 240\,\mathrm{kHz}$ m$/L$.

We have shown that the beamsplitter coupling gives a lower bound for the other couplings when to meet the matching conditions. We have to find a setup which reaches a strong rate of down-conversion coupling

$$g_{\mathrm{DC}} = \Gamma l \frac{c}{L}. \qquad (6.51)$$

If we have a sufficiently high nonlinear coefficient d_{eff} we can reach the given beamsplitter coupling by matching the pump light power. The sum of the down-conversion and beamsplitter coupling must match the optomechanical coupling g which depends on the oscillator's zero point fluctuation $x_{\mathrm{zp}} = \sqrt{\hbar/m\omega_{\mathrm{m}}}$ and can be balanced to a certain de-gree via the intracavity field amplitude $\alpha_{\mathrm{c}} = \sqrt{P/\hbar\omega_c\kappa_{\mathrm{c}}}$. The overall size of the coupling constants can be adjusted via the cavity length L. Regarding the matching of the susceptibilities of the mechanical oscil-

TABLE 6.2: Proposed set of parameters.

L	cavity length	m	1.5
r	beamsplitter reflectivity	%	0.5
$g_{\mathrm{BS}}/2\pi$	beamsplitter coupling	kHz	150
I_{pump}	pump intensity	W/cm^2	45
$g_{\mathrm{DC}}/2\pi$	down-conversion coupling	kHz	150
P	cavity input power	mW	100
$\kappa_{\mathrm{c}}/2\pi$	meter cavity linewidth	MHz	1
$\omega_{\mathrm{m}}/2\pi$	mechanical resonance	MHz	0.5
$\gamma_{\mathrm{m}}/2\pi$	mechanical damping	kHz	5
m	effective mass	kg	10^{-12}
$g/2\pi$	optomechanical coupling	kHz	300
$\kappa_{\mathrm{a}}/2\pi$	ancilla cavity linewidth	MHz	0.2

lator and the ancilla cavity we can write the following requirements

$$rc = \Gamma lc = \frac{1}{2}\omega_{\mathrm{c}}x_{\mathrm{zp}}\alpha_{\mathrm{c}}, \qquad (6.52)$$

$$\Delta = \omega_{\mathrm{m}}, \qquad (6.53)$$

while the condition $\kappa_{\mathrm{a}} = \gamma_{\mathrm{m}}$ can be relaxed to

$$\kappa_{\mathrm{a}} < \omega_{\mathrm{m}}. \qquad (6.54)$$

For the first proof-of-principle experiment of the proposed scheme we must find a suitable micromechanical oscillator with high zero point fluctuation, and a high resonance frequency to realize the resolved sideband limit. Additionally the oscillator needs a high reflectivity and a sufficiently large surface area for use as an end mirror of a cavity. The second task is the reduction of losses inside the ancilla cavity to achieve the resolved sideband limit for this as well. We give a set of challenging but feasible parameters in Table 6.2.

The projected quantum noise reduction for a CQNC experiment with this set of parameters is shown in Fig. 6.10. For this set of parameters we theoretically achieve noise reduction of 10 % at frequencies below the mechanical resonance of the oscillator. Above the resonance fre-
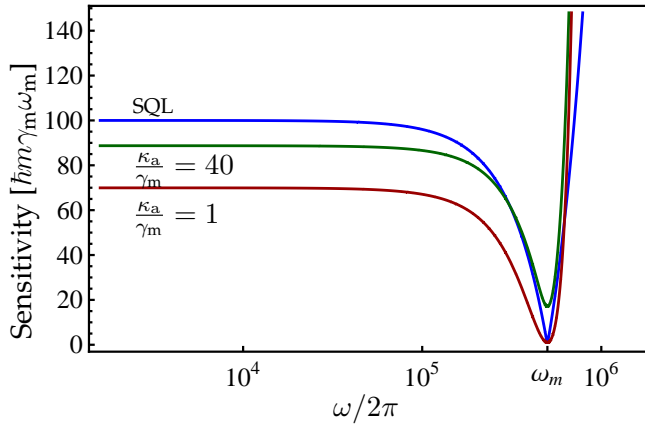
FIGURE 6.10: CQNC noise curve with parameters from Table 6.2. With this
set of parameters we obtain a noise reduction of 10% below the SQL for
frequencies below the resonance frequency.

quency the system will not be enhanced by CQNC and is shot noise
limited. To realize noise reduction at these frequencies with CQNC
the intracavity light power would have to be increased above a criti-
cal value where the optomechanical parameters of the system evolve
into unwanted bound conditions (optical spring) [23] or even chaotic
behavior [82]. This, together with the constraint that the ancilla cavity
linewidth must match the mechanical linewidth of the oscillator, is a
prohibitive argument against the use of CQNC in gravitational wave
detectors. Therefore we concentrate our experimental work on small,
lightweight oscillators with high frequencies to show the experimental
feasibility of CQNC.

For the experimental realization of CQNC we need a system which
is radiation pressure noise limited, and an optical ancilla cavity which
has the same susceptibility as the mechanical oscillator. The experimen-
tal part of this work concentrates on the first investigations of the opti-
cal part of the CQNC scheme. This includes the realization and charac-
terization of a two-mode squeezer, and an experimental analysis of the
effects in polarization-nondegenerate coupled optical cavities. Possible

optomechanical oscillators are currently being investigated, however this is beyond the scope of this thesis. When the parameters aproche those, required for the realization of CQNC, we will merge the optical and the optomechanical systems for the CQNC experiment.

CHAPTER 7

Experimental demonstration of coupled nonclassical systems

With the parameters from Sec. 6.4 we have calculated the parameters for a demonstration of CQNC of backaction noise on small lightweight mechanical oscillators in a tabletop experiment. For the design of an actual experiment we must consider additional parameters to achieve the desired effects. These include beam size, spatial positioning of the optical components, and modematching of the interfering beams. In this chapter we design an experiment which has the goal of demonstrating the matching of down-conversion and beamsplitter couplings (see Eq. (6.26)). In the first part of this chapter we present the choice of parameters for the CQNC experiment and the nonlinear coupling. The actual experimental setup and the measurements of the nondegenerate squeezed fields are shown in the second part. In the third part of the chapter we characterize two coupled cavities with varying coupling strengths and relative phase tunings. Also the possible stabilization of the coupled cavities with different modulation techniques is investigated.
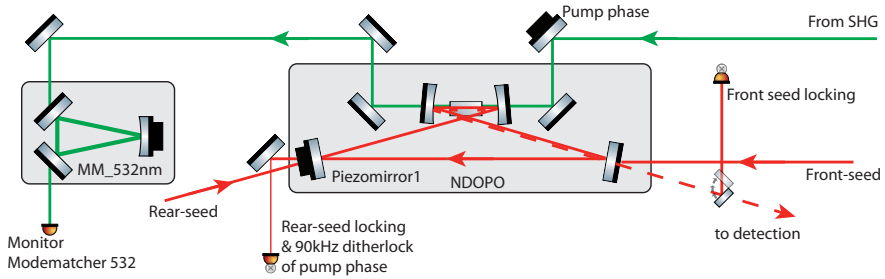
FIGURE 7.1: Schematic of the nondegenerate OPO resonator setup.

7.1 Parameters for the nondegenerate optical parametric oscillator

In this section we design the nondegenerate OPO (NDOPO) cavity. We use the parameters from Table 6.2 as boundary conditions for the cavity geometry as a starting point and add technical constraints to the cavity design. We consider two possible candidates for the nonlinear crystal and present the chosen crystal for the nondegenerate down-conversion process.

7.1.1 Parameters for the NDOPO cavity

The only fixed parameter for the cavity geometry we can take from table 6.2 is the cavity length of 1.5 m. This length is not chosen arbitrarily, we determined this length using the following constraints. The nonlinear process is enhanced with increased power density of the pump inside the crystal. As we cannot increase the pump power infinitely we must reduce the waist size inside the crystal to enhance the effect. This constraint leads to two possible designs for the NDOPO cavity: either a short linear cavity (as used in the squeezing experiment for GEO600 [83]), or a long bow-tie cavity design (similar to that used in the squeezed light source for Advanced LIGO [84]). The short linear cavity design is not suitable for the CQNC scheme because we must couple the meter to the ancilla cavity with an additional beamsplitter coupling, which is realized with a PBS and a $\lambda/2$-waveplate. For the

placement of these components we need space inside the cavity which
is not given for a short cavity design. In addition the light interacts
twice with the $\lambda/2$-waveplate in the linear cavity design, which in-
creases the lower limit for the beamsplitter coupling strength. Because
of these limitations we decided on a bow-tie design for the NDOPO
cavity, a schematic is shown in Fig. 7.1.

Another constraint which we considered was the linewidth of the an-
cilla cavity which must be smaller than the resonance frequency of the
mechanical oscillator (see Eq. (6.38)). Typical resonance frequencies of
possible candidates are between 100 kHz and a few MHz [23]. The
linewidth depends on the reflectivities of the mirrors, the reduction of
intracavity loss and the cavity length (see Eq. (4.11)). This implies that
a longer cavity length is preferred. Here the bow-tie cavity design is
again a good solution for maximizing of the cavity length for a given
space on the optical table.

The length of the cavity is related to another constraint which arises
from the stability criteria for cavities [85] and the achievable beam size
inside the crystal. A small beam waist can be achieved with strongly
curved mirrors or lenses inside the cavity. We wanted to minimize the
amount of intracavity optics (to minimize losses) therefore we could
only rely on curved mirrors for the generation of the beam waist which
set a limitation on the cavity geometry with regards to the cavity length,
waist size, radius of curvature and the diameter of the curved mirror.
The chosen cavity length is a trade-off between these different parame-
ters, which was verified using a simulation tool by Tobias Meier [86].

The overall cavity length is 1.51 m, which corresponds to a FSR of
197.4 MHz. The cavity is set up in a bow-tie design with two flat mir-
rors and two curved mirrors with a radius of curvature of 100 mm. The
distance between the flat mirrors was chosen to be 64 cm and the dis-
tance between the curved mirrors was 11 mm. This results in two beam
waists inside the cavity according to [85]: one large waist of 348 μm be-
tween the flat mirrors and a small waist with a size of 23 μm between
the curved mirrors. The crystal was centered at the position of the small
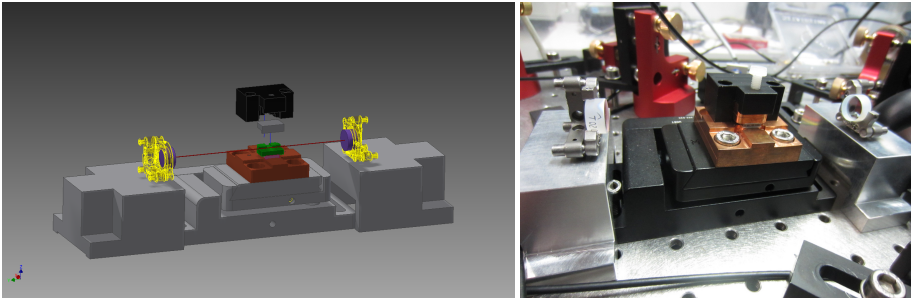waist using a standard five-axis aligner (Newport 9081) and a custom

FIGURE 7.2: CAD-drawing and photo of the implemented oven design.

oven design which is shown in Fig. 7.2. The crystal phasematching
temperature was controlled with a peltier element, a thermistor and a
servo controller designed by H. Vahlbruch [87].

The reflectivities of the mirrors were chosen as follows. The input
coupler had an input power reflectivity of 90 %. For the characteriza-
tion of the squeezed field the cavity needed to be locked with a rear
input beam. The second flat mirror had a reflectivity of 99.8 %. The
curved mirrors were HR coated for the fundamental wavelength of
1064 nm. All mirrors had AR-coatings for the pump wavelength of
532 nm.

7.1.2 Nonlinear crystal

In the experimental case study for the CQNC scheme (Sec. 6.4) we dis-
cussed the possible nondegenereate effects of nonlinear crystals. We
need a bidirectional effect for both the down-conversion and the beam-
splitter interactions. Our design makes use of polarization nondegen-
erate effects because bidirectional optics are commercially available for
both the beamsplitter and the down-conversion effect. The beamsplit-
ter interaction is hereby realized with a polarizing beamsplitter cube
or a calcite beam displacer, and the down-conversion process is gen-
erated with a type II process inside a nonlinear crystal. For a strong
nonlinear interaction we need a crystal with a high nonlinear coeffi-

cient d_{eff} for the type II interaction. The two crystals with the highest type II nonlinear coefficients suitable for our application are potassium niobate ($KNbO_3$ or KN) with $d_{\text{eff}} \cong 13.7\,\text{pm/V}$ and potassium titanyl phosphate ($KTiOPO_4$ or KTP) with $d_{\text{eff}} \cong 4.6\,\text{pm/V}$ [88].

Potassium niobate has a comparatively very high nonlinear coefficient for the type II interaction which would decrease the need for high pump powers for the NDOPO. Also, noncritical phasematching temperatures have been observed for wavelengths from 860 nm to 950 nm from room temperature up to 180 °C [89]. At these frequencies one can use the full nonlinear coefficient without walk-off and high nonlinear interactions are achievable. However, for the chosen wavelength of 1064 nm noncritical phasematching is not possible. To make use of type II interactions we therefore need a periodically poled KN crystal. We were not able to find a manufacturer which was able to produce crystals with the required poling period of 2.8 μm, which is needed for quasiphasematching at realistically achievable phasematching temperatures.

KTP is a widely used nonlinear crystal; the highest values for quantum noise reduction have been shown with periodically poled KTP (PPKTP) [57], which can be produced in good quality with low losses. The highest nonlinear coefficient of this material is along the z-axis where a type I interaction is obtained. For type II interactions one can use a noncritical phasematching temperature of 63 °C for a wavelength of 1080 nm [56]. Also, periodic poling can be applied with high precision to use different wavelengths and interactions in the KTP crystal with the reduced interaction strength of $2/\pi$ shown in Sec. 3.2.

The nonlinear crystal used in our experiment is a prototype PPKTP crystal with dimensions $1 \times 2 \times 10\,\text{mm}^3$ and a quasiphasematching period of 458 μm for the conversion of nondegenerate fields at 1064 nm to 532 nm. We calculated the period with the Sellmeier coefficients from [90, 91] and with the help from O. Pfister who has used a similar crystal in a recent experiment [92]. With this poling period we make use of the type II nonlinear coefficient along the optical x-axis of the crystal. We can produce either a second harmonic in p-polarization with a linearly polarized fundamental field under 45°, or use the opposite
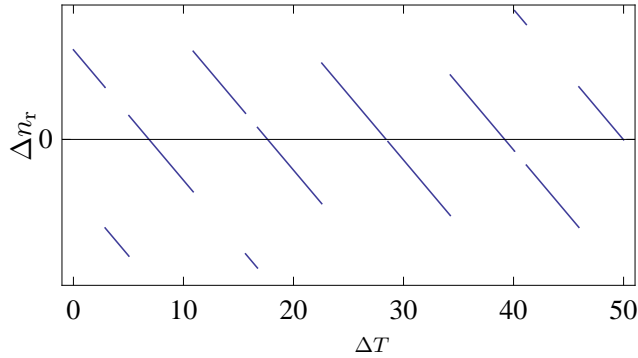
FIGURE 7.3: Relative refractive index $\Delta n_{\rm r}$ vs. relative phasematching temperature ΔT for the type II interaction of PPKTP. The interacting wavelengths are the fundamental wavelength at 1064 nm in p- and s-polarization, and the pump wavelength at 532 nm. T_0 is set to $20°$ C. Zero-crossings of the $\Delta n_{\rm r}$ indicate ideal phasematching temperatures.

effect to obtain a two-mode squeezed field which is nondegenerate in polarization. The effective nonlinear coefficient for this interaction is 2.92 pm/V. The temperature dependency of the phasematching behavior is shown in Fig. 7.3 where we see that the ideal phasematching temperature is $27°$ C.

This crystal is the best option available for the chosen parameters in order to realize the proof-of-principle experiment detailed in Sec. 6.4 and Sec. 7.1. The nonlinear effects generated in the experiment using this crystal are characterized in Sec. 7.2.6.

7.2 Experimental setup

A schematic of the experimental setup is shown in Fig. 7.4. For convenience we simplified the schematic by neglecting modematching lenses and most steering mirrors. The colored parts are explained in more detail in the following sections.

7.2.1 Laser preparation

The main laser source was a continuous wave nonplanar ring oscillator (NPRO) laser at 1064 nm with an output power of 2 W (Innolight
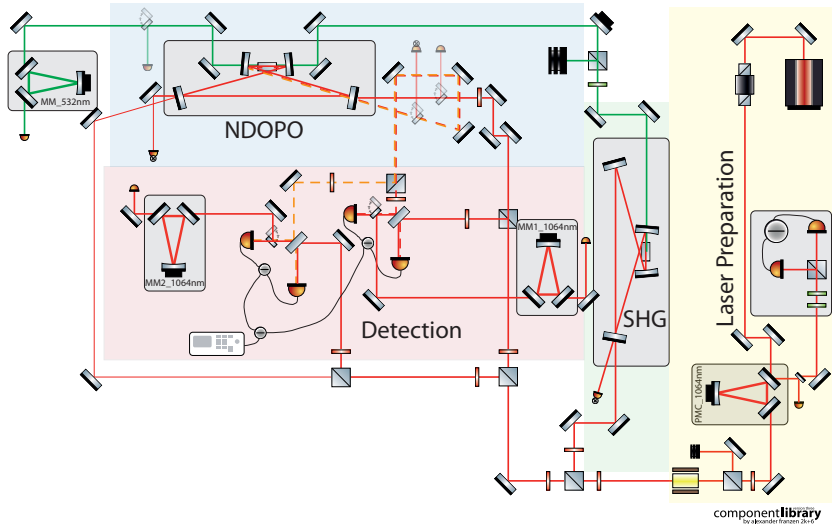
FIGURE 7.4: Simplified schematic of the experimental setup. The individual parts are explained in more detail in additional schematics (see Figures 7.1, 7.5, 7.6, 7.8)

Mephisto). We installed a Faraday isolator stage to protect the laser from backscattered light with an extinction ratio of 40 dBm. To reduce laser amplitude noise and spatial fluctuations the light was transmitted through an impedance matched modecleaning cavity [93]. The modecleaner additionally is a spatial reference for further modematchings of the experiment. The modecleaning resonator was locked with the modulation-free homodyne locking technique [94]. In transmission of the modecleaning cavity an electro-optic modulator generated Pound-Drever-Hall (PDH) phase modulation sidebands [95] at 30 MHz to provide error signals for the length control of the SHG and the OPO cavity. Later these sidebands were used for the characterization of the coupled resonator system described in Sec. 7.3.

7.2.2 Second harmonic generation

The nonlinear process in the NDOPO is linearly dependent on the pump power [55]. Therefore a stable SHG with high output power to gener-
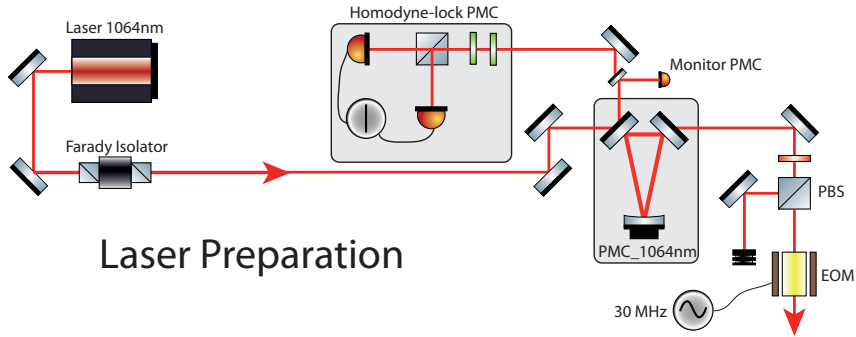
FIGURE 7.5: Setup of the laser preparation stage. The laser is protected with a Faraday isolator and spatially filtered with a modecleaning cavity. An electro-optical modulator imprints phase modulation sidebands at 30 MHz onto the carrier light.
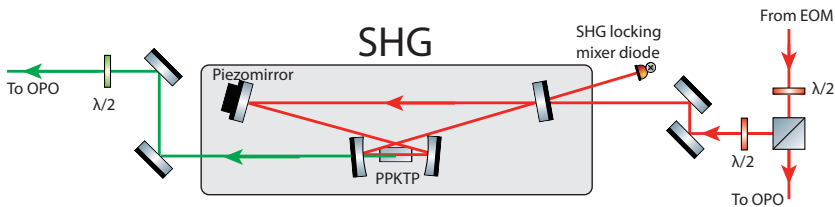

FIGURE 7.6: Setup of the bow-tie second harmonic generation resonator. The PPKTP crystal between the curved mirrors converts 1064 nm light into 532 nm light with an efficiency of 64 %.

ate a sufficiently strong down-conversion coupling inside the NDOPO is required. We developed an SHG resonator in a quasimonolithic bow-tie design. The simulations regarding stability and higher-order mode degeneration were calculated using the same simulation tool as for the NDOPO [86].

The quasimonolithic cavity consists of an input coupler with power reflectivity of 90 % at the fundamental wavelength of 1064 nm, one flat pump mirror with a HR coating for the fundamental wavelength and two curved pump mirrors with radius of curvature of 100 mm. All mirrors have an AR coating for the second harmonic wavelength of 532 nm. The length of the resonator is 70.4 cm where the distance between the

two flat mirrors is 23 cm and the distance between the curved mirrors is 11 cm. This results in two beam waists, one of 265 μm between the flat mirrors and a small waist of 40.8 μm between the curved mirrors. The nonlinear crystal is a PPKTP crystal with a periodic poling period of 9.01 μm. The crystal is coated with an AR coating for both the fundamental and the second harmonic wavelength. We control the crystal temperature with an integrated oven design consisting of a peltier element, two L-shaped copper plates holding the crystal. A cap made of Polyoxymethylene (POM) fixes the position of the crystal and shields the system against temperature fluctuations caused by air flow. The electronic design of the temperature controller is the same as for the NDOPO crystal temperature.

The resonator body is milled from a solid aluminum block on which the mirrors aree clamped from the outside. This quasimonolithic design has two advantages. The first is the long term spatial stability which is necessary for further pump alignment and modematching to the OPO cavity. The second is the successful suppression of mechanical resonances at ~ 600 Hz which were limiting the controller bandwidth in a prototype setup containing commercial mirror mounts. With the quasimonolithic design we can achieve a unity gain frequency of 5 kHz for the length control of the resonator. The cavity tuning is controlled with a ring piezo clamped between the flat pump mirror and the rigid resonator body. A CAD drawing and a photo of the implemented design is shown in Fig. 7.7.

The SHG has an output power of 450 mW at 532 nm with a fundamental input power of 700 mW. This is equivalent to a conversion efficiency of 64 %.

7.2.3 Pump beam alignment

For the optimization of the nonlinear coupling between the pump and the fundamental modes the pump field had to be aligned spatially to
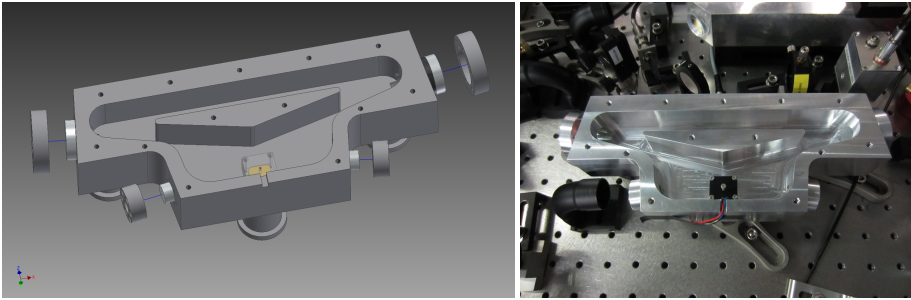
FIGURE 7.7: CAD-drawing and photograph of the experimental implementation of the second harmonic generation bow-tie cavity.

the intracavity field of the NDOPO. Since all cavity mirrors have an AR coating for the second harmonic the OPO-cavity cannot be used as a reference for the alignment of the pump field. Following the modematching rules of Gaussian beams the two fields are spatially overlapped at any point of propagation if they are modematched into the same cavity [85]. Therefore we included an additional modematching cavity behind the crystal (see Fig. 7.1). To achieve spatial overlap for the two light fields we locked the NDOPO cavity in SHG mode with a 45° linearly polarized beam at the input coupler. The generated 532 nm beam was then matched to the modematching cavity. Afterwards we blocked the NDOPO cavity and matched the pump field to the modematching cavity through the crystal. We could achieve an overlap of the fundamental and pump fields of 98 % at the modematcher and therefore inside the crystal.

7.2.4 Visibility of the homodyne detectors

The balanced homodyne detection scheme was introduced in Sec. 3.1. To detect the reduced vacuum noise the generated squeezed light was interfered with a local oscillator at a balanced beamsplitter. A measure of the spatial overlap of the two beams is the visibility of the balanced homodyne detector. The visibility can be measured with two fields of equal strength on the beamsplitter. The ratio between the intensities at
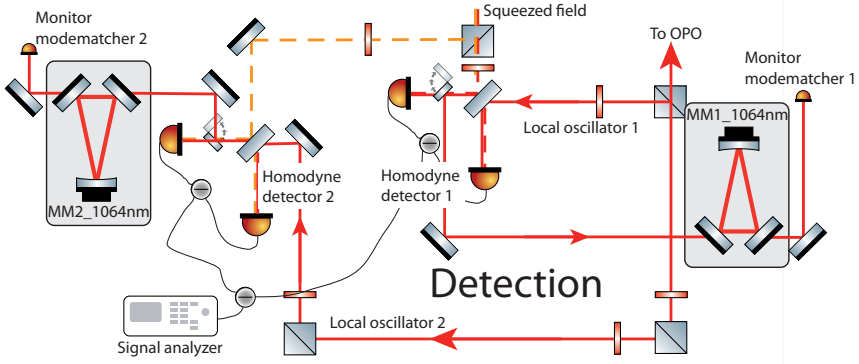
FIGURE 7.8: Setup of the homodyne detection. The squeezed fields (dashed) were interfered with the local oscillators on balanced beamsplitters. The spatial overlap of the two light fields was ensured with two modematching cavities. The detected photocurrents were subtracted and measured with a signal analyzer.

constructive and destructive interference gives the visibility

$$\eta_{\text{vis}} = \frac{U_{\max} - U_{\min}}{U_{\max} + U_{\min}}. \tag{7.1}$$

Nonperfect visibility adds as a loss channel into the measurement with its squared value [62]. Therefore an optimization of the visibility is important for the detection of squeezed states. We aligned the squeezed field with the local oscillator on a modematching cavity using a flip mirror behind the beamsplitter as a pickoff for the alignment path (see Fig. 7.8). The interference pattern of the two individual homodyne detectors is shown in Fig. 7.9. The measurement yielded a visibility of 97.9 % for the first homodyne detector and 97.2 % for the second homodyne detector.

7.2.5 Measurement procedure

The correlations inherent in nondegenerate squeezed states cannot be detected with a single homodyne detection. The two entangled modes must be separated on a PBS and then detected at individual balanced homodyne detectors. The individual photocurrents of the homodyne
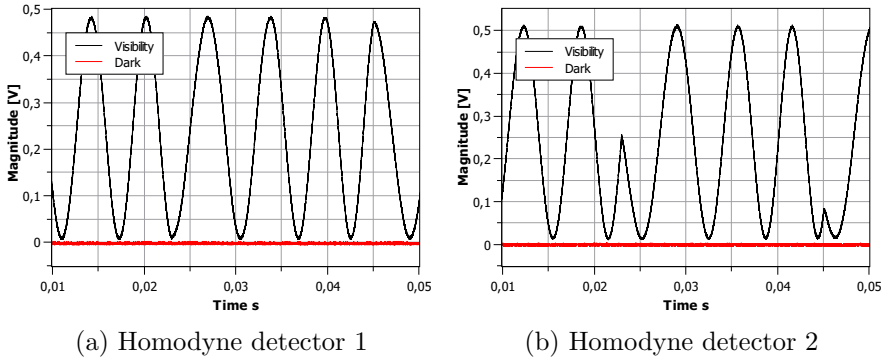
(a) Homodyne detector 1   (b) Homodyne detector 2

FIGURE 7.9: Visibility measurement of the two homodyne detectors. We were able to achieve a visibility for the first homodyne detector of 97.9 % and a visibility for the second detector of 97.2 %

detectors are subtracted afterwards to get the variances of the individual fields, and one can measure the squeezed and antisqueezed phase quadratures with a signal analyzer (see Sec. 3.4.2 and Sec. 3.4.3).

The resonant relaxation oscillation oscillation at 800 kHz is the dominant noise source of the unstabilized NPRO laser [96]. We did not implement a stabilization scheme to be shot noise limited at baseband frequencies (as done for the lasers in gravitational wave detectors). With a relatively small linewidth of the NDOPO cavity of 6 MHz the measurement is not shot noise limited within the zeroth FSR. To measure the maximum squeezing level the measurements were taken at the frequency of the first FSR $f = 197.4$ MHz. The detection of squeezed light at such high frequencies a homodyne detector design by M. Mehmet [97] is used. The light was detected by two InGaAs photodiodes (Fermionics FD70) with an active area of 70 μm. The photodiodes were arranged in a *back-to-back* design such that the photocurrents are directly subtracted after detection. The DC-part of the signal was split off via an RF-choke stage to get error signals for the local oscillator phase lock. The AC-signals were amplified by three Mar-6+ (Minicircuits) amplification stages. The added noise curves of both detectors are shown in Fig. 7.10. We have a dark noise clearance of 10 dB at 200 MHz. The
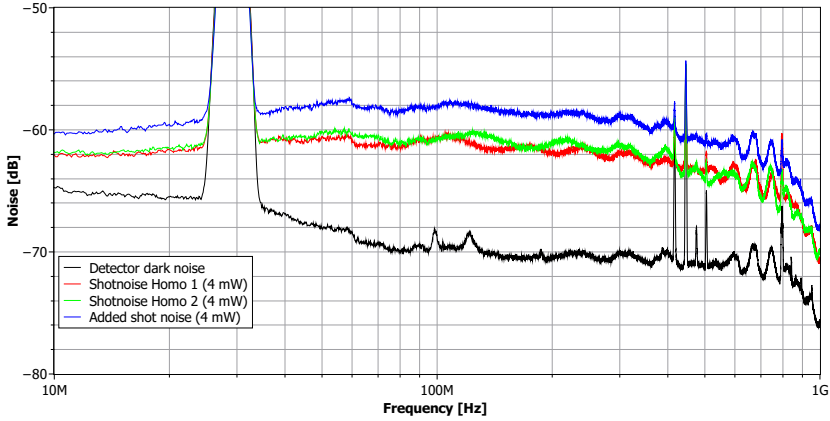
FIGURE 7.10: Power spectral density of the homodyne detectors from 10 MHz to 1 GHz. In black we see the added dark noise of the two detectors. In red and green the shot noise of 4 mW light on the individual detectors is shown. The blue curve shows the added shot noise of the two detectors. We see that the shot noise is uncorrelated because of the 3 dB splitting between the single detector noise and the added noise. The big peak at 30 MHz originates from the modulation sidebands for the stabilization of the cavity.

small difference in shot noise clearance of the two detectors for the detection frequency at 200 MHz can be tuned by adapting the local oscillator field towards equal shot noise clearance for both detectors at the detection frequency. The addition of the two shot noise contributions increases the noise by 3 dB. The shot noise at the two detectors is therefore uncorrelated. The addition and subtraction of the signals were achieved with a high-frequency splitter (Minicircuits ZFSCJ-2-1-S+). The spectrum was monitored with a spectrum analyzer (Agilent MXA-N9020A). Differences in the beam paths which cause loss of correlation [98] were compensated with unequal cable lengths.

7.2.6 Generation and detection of nondegenerate squeezed states in the first free spectral range

For the measurement of two-mode squeezed states the NDOPO-cavity was stabilized with an additional field from the rear of the cavity. This beam was copropagating with the generated squeezed field and was
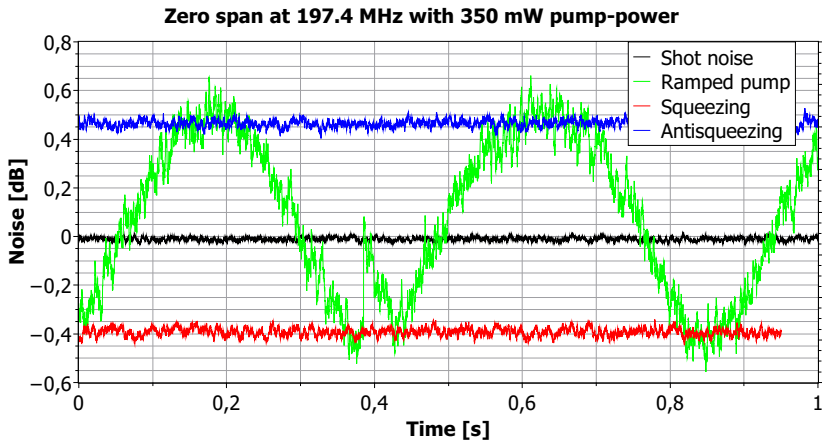
(a) Noise spectrum of a zero-span measurement at 197.4 MHz of the
NDOPO normalized to shot noise (black). We can see the reduced
quantum noise level of 0.4 dB (red) and the corresponding antisqueezed
shot noise with 0.5 dB (blue). The pump power was set to 350 mW.
The green curve shows the noise level alternating between squeezed
and antisqueezed shot noise with a swept pump phase.
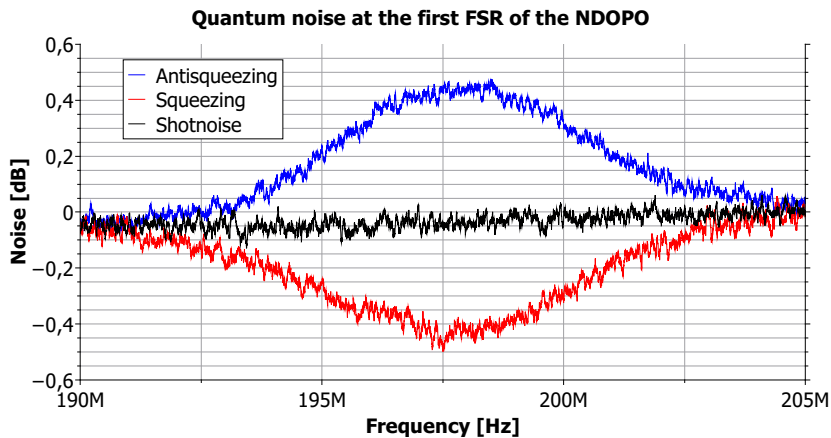
(b) Power spectral density at the frequency of the first FSR of the sta-
bilized NDOPO cavity normalized to shot noise (black). We see the
maximum of squeezed (red) and antisqueezed (blue) noise at the fre-
quency of the first FSR (197,4 MHz). The pump power was set to
350 mW. The rise in amplitude with increased frequency is a detector
artifact (compare Fig. 7.10).

FIGURE 7.11: Squeezing measurements of the NDOPO at the first FSR

additionally used to lock the pump phase and the local oscillators at the homodyne detectors.

The pump phase was stabilized with the dither locking technique [99]. The copropagating beam is affected by amplification and deamplification from the pump field and modulation sidebands on the pump field are transferred to the copropagating fundamental field which can then be detected with demodulation techniques. We imprinted a phase modulation of 90 kHz onto the pump light and detected these at the locking detector for the cavity lock in the rear locking port. We demodulated the signals using a Minicircuits ZAD 3+ mixer and obtained a sinusodial error signal for the pump phase lock.

The local oscillator phase was locked onto the phase quadrature of the signal field by use of a fringe stabilization technique [100]. The interference pattern of the local oscillator with the residual control beam of the cavity stabilization can be used to stabilize the detection to the phase quadrature. The phase quadrature corresponds to the *mid-fringe* [100] of the interference where we can use the zero crossing as an error signal without additional modulation and demodulation techniques.

In Fig. 7.11a we see a zero-span measurement of the stabilized squeezed and antisqueezed fields for a swept pump phase. The measurement frequency is set to the frequency of the first FSR at 97.4 MHz and the noise spectrum is taken over a time span of 1 s. The measurement was performed using 10 averages and yielded 0.4 dB of squeezing field and correlating antisqueezing of 0.5 dB. Fig. 7.11b shows a frequency scan around the first free spectral range of the cavity at 197.4 MHz. We see the cavity enhancement of the squeezed and antisqueezed fields inside the cavity linewidth.

The generation of squeezing was mainly limited by the small nonlinear coefficient. Increased pump power is a possible solution to achieve higher amounts of squeezing. High power densities of the pump wavelength inside the crystal induce an unwanted effect called *gray tracking* which generates loss inside the cavity [101], therefore we decided against the use of a stronger pump for the characterization of the NDOPO cavity. The simulations with the used amount of pump power

yielded an initial squeezing value of 0.9 dB. To reach the calculated
down-conversion coupling g_{DC} from Sec. 6.4 the nonlinear coefficient
and the currently available pump power were too small.

The reduced amount of measured squeezing can be explained by the
presence of loss in the experiment. The measured values for squeez-
ing and antisqueezing correspond to a loss of $\sim$45 %. The main loss
channel is the quantum efficiency of the photodiodes of 81.5 % [102].
The second individual loss contribution is the visibility of the homo-
dyne detection as already discussed. The measured visibility affects
the measurement with $\eta_{vis} = 5.8$ %.

A strong loss channel in our experiment were propagation losses. The
HR coatings of the steering mirrors are designed for s-polarization at
45° incident angle. The reflectivity for p-polarization is 99.8 %. As
our two-mode squeezed field contains both polarizations, one part of
the entangled field is affected by a higher loss contribution than the
other. Another propagation loss channel occurs in the polarization op-
tics which are used for the separation of the two entangled beams. Al-
though the optics are AR coated for the laser wavelength residual ab-
sorption and reflections at the transmitted optics introduce loss on the
squeezed light.

The last loss channel to mention is the nonideal AR coating of the glass
windows of the photodiodes and the reflectivity of the semiconductor
material. The windows have an AR coating which is chosen by the
manufacturer. The coating is optimized for 1550 nm and therfore in-
troduces significant loss to our experiment. We could not measure the
effect directly, therefore we are not able to give a value for this loss con-
tribution. For further characterizations we will remove the windows
from the diodes to eliminate this loss channel. The InGaAs chips had
no AR coating which is another loss channel we were not able to char-
acterize in this measurement.

In the future we will eliminate some of the loss channels for further
characterization of the experiment. This includes diodes with higher
quantum efficiency and AR coating on the chip, customized AR-coatings
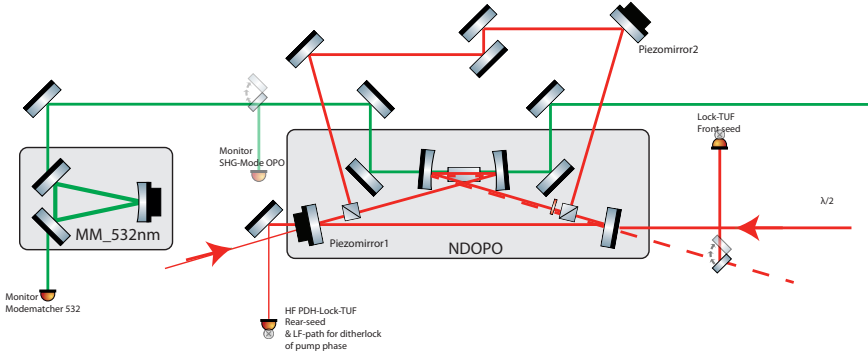for the optics and to minimize the amount of optical components be-

FIGURE 7.12: Experimental setup of the coupled resonators.

cause these will remain an issue for further measurements.

7.3 Coupled cavities

In the previous section we have demonstrated the feasibility of the generation of polarization nondegenerate squeezed states. The setup for the CQNC scheme demands the coupling of the nondegenerate field to an ancilla cavity via an additional beamsplitter process [43]. In our experiment we realize the beamsplitter coupling with a PBS and a $\lambda/2$-waveplate. This setup enables dynamical tuning of the reflectivity and thus the coupling strength $g_{\mathrm{BS}} = rc/L$ between the two cavities. In this section we characterize the effects which occur at different operating points of the beamsplitter coupling and the relative tuning of the coupled cavities. We compare our results with the simulations we have done, using the formalism from Sec. 4.2. For a demonstration of CQNC we need to lock the ancilla cavity to a detuning $\Delta_{\mathrm{a}} = \omega_{\mathrm{m}}$ (see Eq. (6.33)). We analyze the effects of the coupled cavities on modulation sidebands for the generation of error signals to stabilize cavities to specific operating points and detunings.

7.3.1 Experimental setup

For the demonstration of the beamsplitter coupling we adapted the
OPO-cavity which we used for the two-mode squeezing experiment.
A schematic is shown in Fig. 7.12. We denote the original cavity con-
taining the input/output coupler as *meter cavity*. We added the $\lambda/2$-
waveplate and the PBS inside the cavity to have a dynamical coupler
for the second cavity, which we further denote as *ancilla cavity*. The
ancilla cavity was designed to have the same length as the meter cav-
ity and consisted of four mirrors, the coupling PBS and an additional
PBS for the coupling back into the meter cavity. With this setup we en-
sured the identical beam-path of the meter and ancilla cavity through
the nonlinear crystal. Two mirrors were used as steering mirrors to
simplify the alignment procedure and to guarantee the optimal beam-
splitting angles for the PBS. The tuning Φ_2 of the ancilla cavity was
adjusted with a piezo-actuated mirror.

The mirrors of the ancilla cavity were HR coated for the fundamental
wavelength of 1064 nm. We measured a round trip loss of 1.8 % due to
the intracavity optics which corresponds to an ancilla cavity linewidth
of 737.2 kHz for a beamsplitter reflectivity of 0.5 % (see Table 6.2). This
measurement shows that the parameters for the ancilla cavity linewidth
are feasible when the AR coatings of the transmitted optics are opti-
mized for this experimental setup.

7.3.2 Simulations of modulations sidebands in coupled cavities

We simulated the resonance feature and the dependency of the FSR
as a function of the beamsplitter coupling in Sec. 4.2. To verify these
simulations experimentally we scan the tuning of the meter cavity for
different operating points of the ancilla cavity while monitoring the res-
onance pattern in reflection of the input-coupler. Phase modulation
sidebands serve as a reference to ascertain the actual frequency split-
ting of two neighboring resonances (see Fig. 7.13). We have shown that
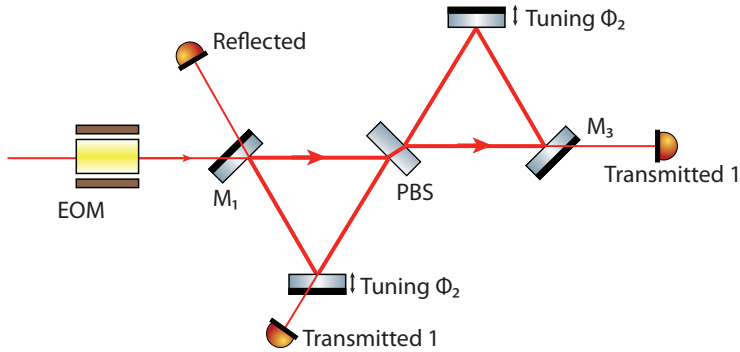for a tuning $\Phi_2 = 90°$ we can determine a variable tunable FSR for

FIGURE 7.13: Schematic of the ring cavity for the Finesse simulations. We phase modulate the carrier field with sidebands at 30 MHz and simulate the reflected power and the demodulated sidebands in reflection and transmission.

different couplings ρ_2. The plot in Fig. 7.14 shows simulations of the reflected power from a coupled cavity and the corresponding reflected sidebands at 30 MHz as a function of the tuning Φ_1 and the reflectivity of the PBS ρ_2. The upper sideband is colored in blue and the lower sideband in yellow. With the frequency reference given by the sidebands we can deduce the dynamic tuning of the FSR we calculated in Eq. (4.22).

For no detuning ($\Phi_1 = \Phi_2 = 0°$) the sidebands are affected by the resonance splitting of the coupled resonator (see Fig. 7.15). For high reflectivities of the intracavity coupler we see a resonance peak at $0°$ which has symmetric sidebands. For lower reflectivities ρ_2 the sidebands follow the individual resonance branches towards $90°$. Here the upper sideband intersects the lower sideband at a frequency splitting of twice the modulation frequency. This behavior suggests that generating usable error signals for the case of no detuning will be difficult to achieve (see Sec. 7.3.4).

Fig. 7.16 shows the reflected amplitude and the modulation sidebands with varying reflectivity ρ_2 for a detuned second cavity with $\Phi_2 = 30°$. For some value ranges of ρ_2 the sidebands have an unequal

(a) Intensity

(b) Sidebands

FIGURE 7.14: Behavior the reflected power and of 30 MHz phase modulation
sidebands in reflection of the coupled cavity versus tuning of the meter
cavity Φ_1. The ancilla cavity is held on anti-resonance $\Phi_2 = 90°$. (a) The
reflected power has a resonance at $\Phi_1 = 0°$ which is reduced in amplitude
with increased reflectivity ρ_2^2. (b) The blue branch is the upper sideband
and the yellow branch the lower sideband. We see the dynamical change
in free spectral range and linewidth due to the increased coupling between
the two cavities.

(a) Intensity

(b) Sidebands

FIGURE 7.15: Behavior the reflected power and of 30 MHz phase modulation
sidebands in reflection of the coupled cavity versus tuning of the meter
cavity Φ_1. The ancilla cavity is held on resonance $\Phi_2 = 0°$. (a) The reflected
power has a resonance at $\Phi_1 = 90°$ which becomes broader with increased
reflectivity ρ_2^2. For a reflectivity $\rho_2^2 = 1$ we get a sharp resonance at $\Phi_1 = 0°$.
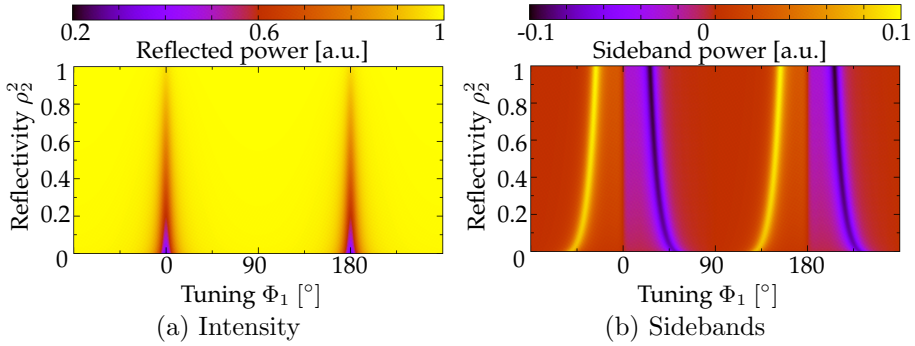(b) The sidebands (upper: blue, lower: yellow) cross at a reflectivity $\rho_2^2 =
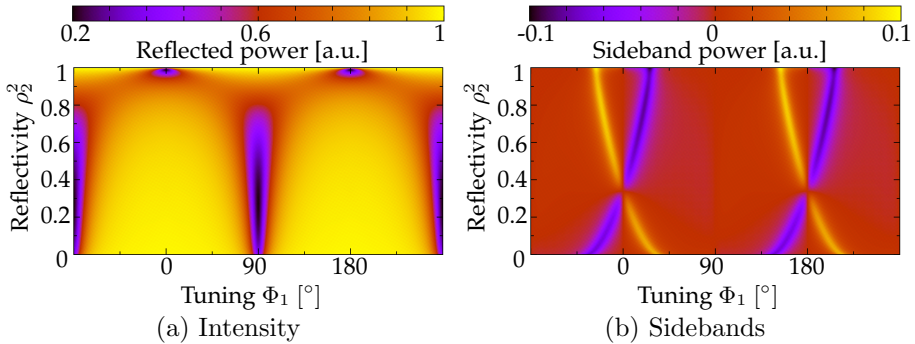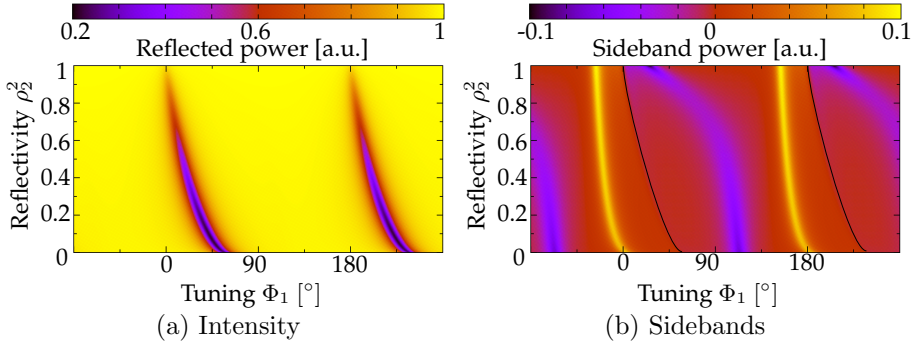0.3$.

FIGURE 7.16: Behavior the reflected power and of 30 MHz phase modulation sidebands in reflection of the coupled cavity versus tuning of the meter cavity Φ_1. The ancilla cavity is detuned by $\Phi_2 = 30°$. (a) The resonance peaks are deformed and shift from $\Phi_1 = 90°$ to $\Phi_1 = 0°$ with increased reflectivity ρ_2^2. (b) The sidebands (upper: blue, lower: yellow) are reflected asymmetrically by the detuned coupled cavities. The position of the resonance is drawn for orientation in black.

frequency spacing to the carrier. For the control of detuned cavities these effects must be investigated to generate error signals which give useful locking points. The relative detuning of the cavities with respect to each other has a great impact on the reflected modulation sidebands. Fig. 7.17 shows the asymmetric behavior of the reflected sidebands with respect to the relative detuning of the cavities. Even for a reflectivity of $\rho_2^2 = 0.8$ of the intracavity coupling mirror we see crossing sections of the upper and lower sideband of two neighboring resonance peaks. If we use the sidebands as a ruler for the axis this could be translated into a FSR which is smaller than the minimal FSR which results from $L_1 + L_2$. We have not yet found an analytical solution that could explain this effect, but further investigations to obtain a deeper understanding are ongoing. The equation for the tunable FSR Eq. (4.22) only holds for the ancilla cavity on antiresonance $\Phi_2 = 90°$
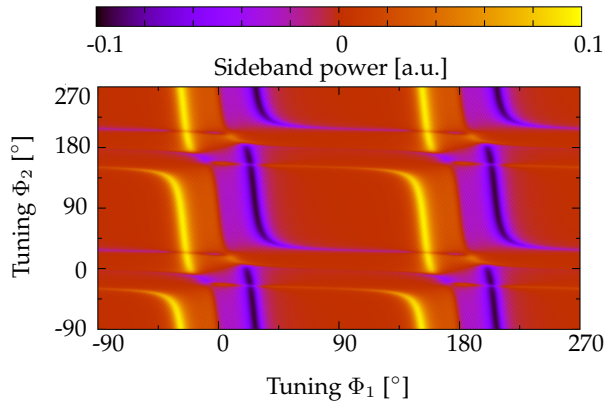
FIGURE 7.17: Reflected sidebands as a function of the relative detunings of the
two coupled cavities. For certain detunings the asymmetry in the reflected
sidebands leads to crossings of upper (blue) and lower (yellow) sideband
of two neighboring resonances.

7.3.3 Analysis of the polarization nondegenerate coupled cavitiy

In Sec. 4.2 we have analyzed the effect of the reflectivity ρ_2^2 of the coupling mirror between the two coupled cavities on the resonance features in reflection. For our setup this tunable coupling mirror is a PBS in conjuction with a $\lambda/2$ wavplate inside the coupled cavity (see Fig. 7.12 and Fig. 7.13). We could tune the reflectivity of this mirror between $0 < \rho_2 < 1$ with the $\lambda/2$-waveplate in the parallel path of ancilla and meter cavity located between the crystal and the PBS.

For the analysis of the coupled cavity we display the resonance feature and the PDH-sidebands at 30 MHz in reflection of the cavity (see Fig. 7.18). The sidebands give a frequency reference to calibrate the x-axis of the oscilloscope. We show the resonance pattern of the coupled cavity for a tuning Φ_1 of the meter cavity over one FSR with the ancilla cavity at a fixed detuning Φ_2. To generate the plots we held the ancilla cavity on anti-resonance ($\Phi_2 = 90°$) manually and tuned the PBS reflectivity with the $\lambda/2$-waveplate. We see that the reflectivity dynamically tunes the effective FSR between 100 MHz and 200 MHz while the resonance shape in reflection does not change its profile. The slight dif-
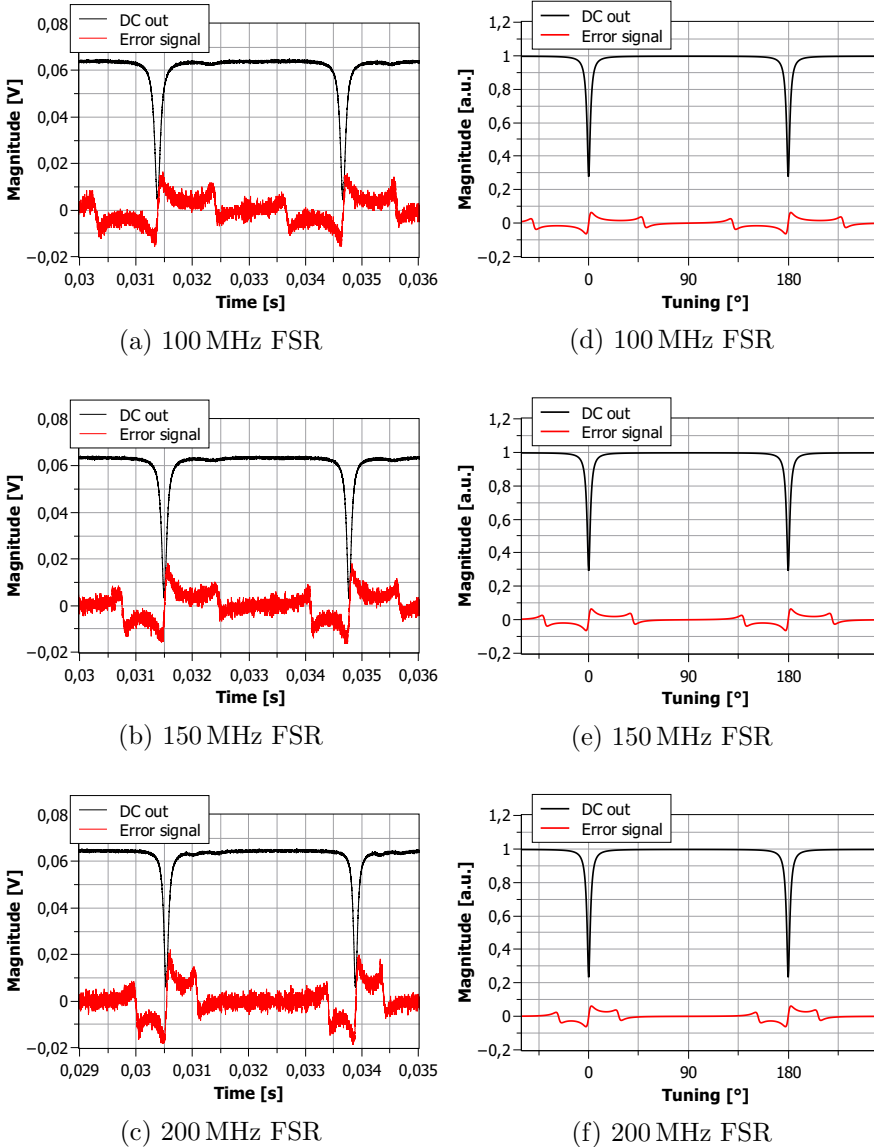
FIGURE 7.18: Measurement (left column (a),(b) and (c)) and a simulation (right column (d),(e) and (f)) of resonance pattern and error signal in reflection of the coupled cavity. We measure the uncalibrated photodiode signal on the oscilloscope as a function of time. The simulation is normalized to a laser power of 1 as a function of the tuning of the meter cavity. The cavity lengths L_1 and L_2 are equal for measurement and simulation. The coupling beamsplitter reflectivity is tuned from 0 (top row) to 1 (bottom row). The reflectivity in the middle row is set to $\rho_2^2 = 0.3$. The corresponding FSRs are given in the captions.
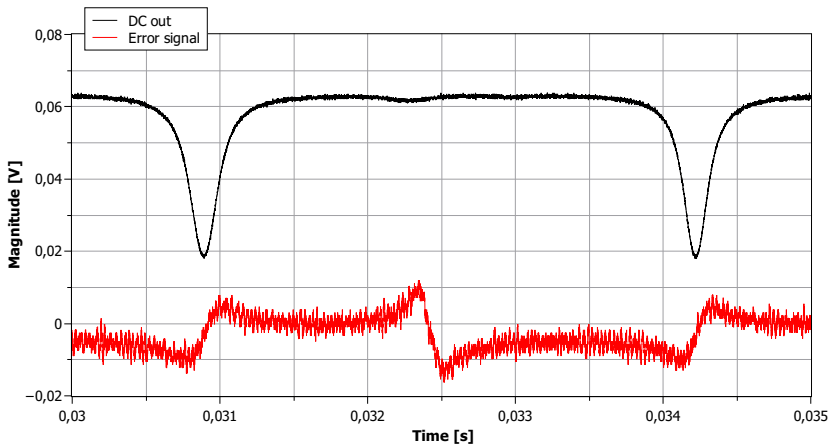
FIGURE 7.19: Crossing error signals due to detuned coupled cavities with
variable PBS reflectivity. If we take the 30 MHz sidebands as a frequency
reference to scale the x-axis, this implies an FSR of 60 MHz which would
correspond to an effective cavity length $L_{\text{eff}} > L_1 + L_2$. This behavior is not
yet understood and is under ongoing investigation.

ferences in amplitude can be explained by additional optics which are
passed in the *long* cavity, introducing losses.

For a detuning of $\Phi_2 = 0°$ we see the crossing of the sidebands due
to the resonance splitting of the cavities in Fig. 7.19. For the plotted case
the effective FSR would be at 60 MHz which gives an effective length
$L_{\text{eff}} = 4.99$ m which is longer than the combined length of the two cou-
pled cavities $L_1 + L_2 = 3$ m. The experiment shows the same behavior
as the simulations in Fig. 7.17 and needs to be further investigated in
future work.

7.3.4 Stabilization of the coupled cavities

To show the calculated effects from Sec. 6.4 we need to stabilize the
coupled cavities to different tunings Φ_2. For the control of the coupled
cavities to different relative detunings we need error signals for both
the meter and the ancilla cavity which are decoupled from each other.
An example for decoupled error signals is given in Fig. 7.20. The er-
ror signals are shown in the diagonal elements. Crosscouplings would

(a) Demodulation for Φ_1

(c) Demodulation for Φ_1

(b) Demodulation for Φ_2

(d) Demodulation for Φ_2
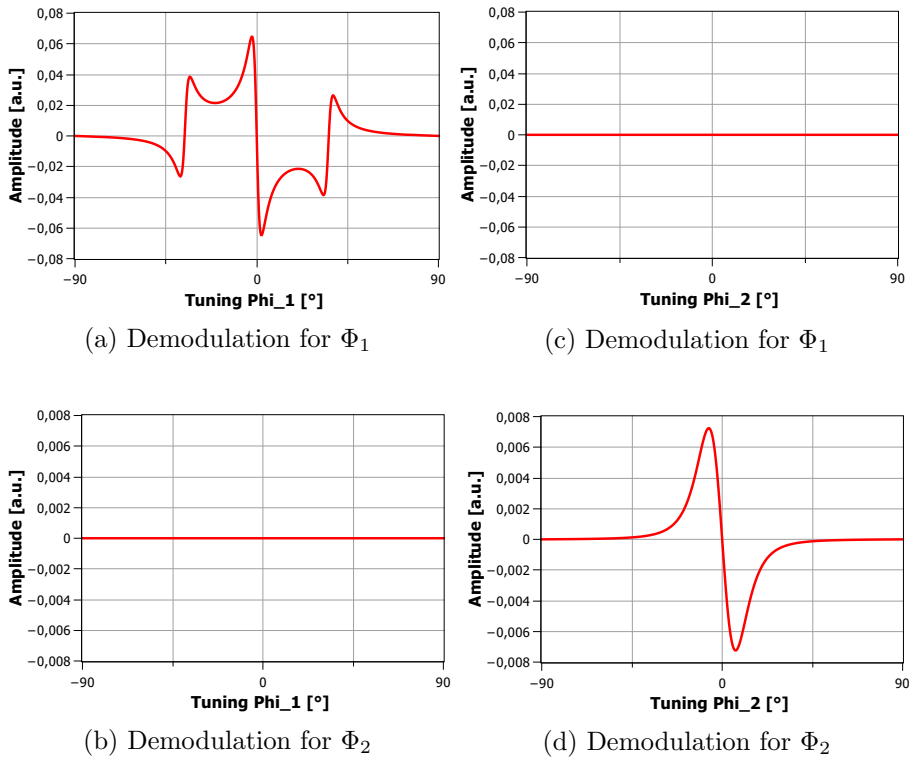
FIGURE 7.20: Example for an ideal control matrix with decoupled error signals. The tuning of Φ_1 has no impact on the demodulation for the error signal of the tuning Φ_2 and vice versa.

(a) Demodulation for Φ_1

(c) Demodulation for Φ_1

(b) Demodulation for Φ_2

(d) Demodulation for Φ_2
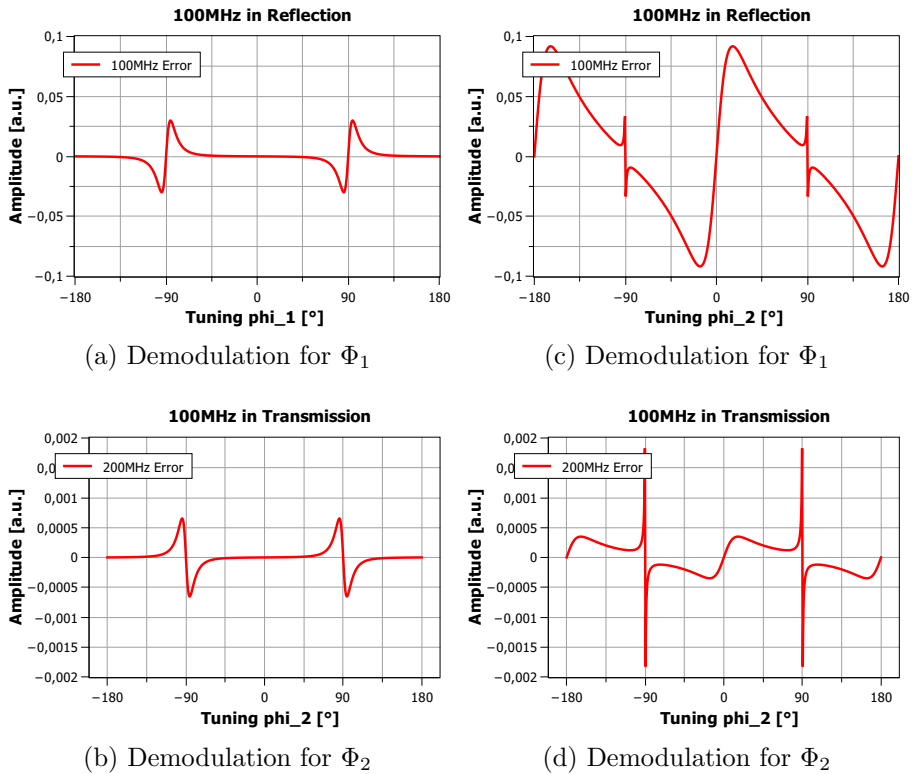
FIGURE 7.21: Example of a control matrix for the simulation of error signals in coupled cavities. The signals are generated in reflection of the incoupler and in transmission of one cavity mirror of the meter cavity. The modulation frequency is set to 100 MHz. We see that the offdiagonal element in (c) has a steeper slope than the actual error signals. This cross-coupling prohibits the stabilization to different operating points.

appear in the off-diagonal elements. We see that the tuning Φ_1 has no impact on the error signal for the tuning Φ_2 and vice versa because the off-diagonal elements vanish.

We analyzed the control matrix for the stabilization of the coupled cavities for different modulation frequencies and different output ports. Following the results from the stabilization of the *twin-signal-recycling* experiment [68] we simulated error signals with sidebands at the frequency of one FSR (200 MHz) of the cavities, at the FSR of the long combined cavity (100 MHz) and at the PDH frequency we used to sta-

bilize the NDOPO cavity without ancilla cavity (30 MHz). One exemplary control matrix is plotted in Fig. 7.21. Even if the slope of the off-diagonal error signal were smaller the system would be able to be stabilized in a hierarchical control scheme [68]. We can see that the slopes in one of the the off-diagonal elements is steeper than for the diagonal elements. This prohibits a stabilization of the coupled cavities with the modulation techniques available. The simulations were done for both cavities on resonance $\Phi_i = 0$. We also did simulations for detuned cavities but could not find decoupled error signals for controlling both cavity tunings. This shows that the system is not controllable with only one carrier frequency. To show the effects of CQNC in an experiment we must investigate other stabilization methods for the coupled cavities. A possible approach to stabilize the cavities independently uses an auxiliary laser at a different wavelength as suggested in [66] or similar to what is done for the arm cavities in Advanced Ligo [103]. This should be investigated in future work.

7.4 Conclusion

In this chapter we have demonstrated the generation of nondegenerate squeezed states in a setup designed for the use in a CQNC experiment. The generation of squeezed states was limited by the nonlinear coefficient of the prototype PPKTP crystal and the available pump power. Furthermore the detection of the squeezed states was limited by different loss channels. The effects which were observed were too small to be used for CQNC, but the knowledge obtained with the experiment can be used for the design of a more sophisticated experimental setup for the generation of nondegenerate squeezed fields.

In the second part of this chapter the behavior of coupled cavities was investigated. We demonstrated the dynamical tuning of the FSR which was calculated in Sec. 4.2 experimentally and analyzed the behavior of modulation sidebands in coupled cavities. The analysis showed that in contrast to other experiments [68, 26] we cannot generate error signals for the stabilization of the coupled cavity to different tunings with a sin-

gle carrier due to strong cross-couplings in the error signals generated
with the common modulation techniques and must to investigate other,
suitable stabilization techniques, such as the use of auxiliary lasers.

CHAPTER 8

Summary and Outlook

The purpose of this thesis was the theoretical and experimental investigation of a coherent quantum noise cancellation scheme proposed by M. Tsang and C. Caves [43]. Backaction noise will be limiting position measurements such as in interferometric gravitational wave detectors and force measurements in optomechanical quantum experiments with micromechanical oscillators in the near future. This scheme proposes a novel broadband cancellation of backaction noise. This cancellation is realized with an ancilla cavity, coupled to an optomechanical meter cavity via a down-conversion process and a beamsplitter. By adding experimentally realistic mismatches and imperfections to the ideal CQNC conditions of the original publication we developed a more detailed description of the theoretical scheme and calculated the achievable lower limits of noise reduction, and we investigated the robustness of the CQNC scheme against imperfections. These calculations showed that the scheme in this exact form is not applicable for the cancellation of backaction noise in gravitational wave detectors because quantum noise at frequencies higher than the resonance frequency of the mechanical oscillator can only theroretically be reduced by this technique. However CQNC is able to reduce backac-

tion noise in experiments with micromechanical oscillators. To show the noise reduction effects in a proof-of-principle experiment we calculated a possible set of parameters and investigated the possible down-conversion and beamsplitting processes to realize the necessary coupling strengths. This analysis led to the choice of polarization nondegenerate squeezed states and polarizing beamsplitters for use in the first experiment towards CQNC.

We reviewed the possible candidates for nonlinear crystals and designed a prototype PPKTP crystal to produce polarization nondegenerate squeezed states. We prepared the two-mode squeezed states in a bow-tie cavity design and were able to measure a quantum noise reduction of $0.4\,\mathrm{dB}$ at a measurement frequency of $197.4\,\mathrm{MHz}$ at the first FSR of the cavity. Type II squeezing at these high frequencies has, to the best of our knowledge, not been shown before.

The nonlinear effects observed in the nondegenerate subthreshold optical parametric oscillator were not strong enough to be used in a projected CQNC experiment. For future experiments we recommend the use of a different crystal with higher nonlinear coefficient d_{eff} (e.g. $KNbO_3$). Also, different laser wavelengths should be considered in order to make use of noncritical phasematching which has the advantage that the effective nonlinear coefficient is not reduced by a factor of $2/\pi$ as is the case in quasiphasematching.

The detection of the two-mode squeezed light was limited by losses inside the experiment, specifically imperfect HR and AR coatings and insufficient quantum efficiency of the photodiodes. For the design of future experiments these loss channels must be strongly reduced to exploit the full potential of the nondegenerate quantum noise reduction.

We investigated the coupling of the NDOPO cavity to an ancilla cavity following the experimental proposal for CQNC. The coupling was realized by means of a polarizing beamsplitter and a $\lambda/2$-waveplate. With this setup we could achieve an ancilla cavity linewidth which was within the range of the calculated set of parameters for a CQNC experiment. In addition we investigated the behavior of polarization-based coupled cavities to relative detunings of the cavities and the coupling

strength of the central beamsplitter. Apart from the use in a CQNC experiment we observed additional effects which occur in coupled cavities of equal length. We demonstrated dynamical tuning of the effective FSR of two coupled cavities depending on the beamsplitter reflectivity of the PBS. This behavior was observed when the ancilla cavity was held on antiresonance. The experimental results agreed with our simulations for coupled cavities. The analysis raised additional questions about the behavior of coupled cavities which appeared in the experiment and the simulations but could not yet be explained theoretically. For CQNC the coupled cavities have to be stabilized to different detunings depending on the mechanical resonance frequency of the mechanical oscillator. We simulated the behavior of coupled cavities for different modulation techniques and analyzed the possible error signals. Our analysis showed that the stabilization of coupled cavities is prevented by strong cross-couplings of the error signals if only one laser frequency input is used. For future experiments we recommend the investigation and deployment of stabilization schemes with an auxiliary laser frequency such as in [66, 103], or if necessary the development of an entirely new stabilization scheme.

As soon as the nonlinear effect in the NDOPO can be increased and the stabilization issues of the coupled system have been resolved we will in a first iteration show cancellation of artificial radiation pressure noise by merging the coupled optical system, consisting of NDOPO and ancilla cavity, with the cavity system containing the optomechanical oscillator. After demonstrating that CQNC is technically feasible we will move to cryogenic temperatures in order to detect quantum radiation pressure noise and in turn show coherent quantum noise cancellation.

Appendix

Finesse code

This is the Finesse code used for the simulation of the coupled cavities

```
###########################################
#   .kat file for investigating effects   #
#   observed in polarization coupled      #
#        cavities          #
###########################################


#————————Cavity1 input mirror CI1—————————
const RPCI1 0.9 #Power Reflection
const TPCI1 0.1 #Power Transmission

#————————Cavity1 End Mirror CE1————————————
const RPCE1 0.99   #Power Reflection
const TPCE1 0.01   #Power Transmission

#——————————PBS———————————————————————————
const RPPBS 0.80   #Power Reflection
const TPPBS 0.2   #Power Transmission

#————————Cavity2 Loss mirror CL2—————————
const RPCL2 1   #Power Reflection
const TPCL2 0   #Power Transmission

#————————Cavity2 End mirror CE2————————————
const RPCE2 0.9   #Power Reflection
const TPCE2 0.1   #Power Transmission

#——————————Cavity Lengths——————————————————
const L1C1 0.5   #Cavity1 Lengths
const L2C1 0.5
const L3C1 0.5
const L1C2 0.5   #Cavity2 Lengths in m
const L2C2 0.5
const L3C2 0.5

#——————————Modulation Frequencies—————————
```

```
const fmod1 3M
const fmod2 200M

#———————Input Optics———————————————
l laser 1 0 n1
s toeom1 0.1 n1 n2
mod eom1 $fmod1   0.1 2 pm n2 n3s
s toeom2 0.1 n3s n3s1
mod eom1 $fmod2   0.1 2 pm n3s1 n3
s tocav 0.1 n3 cavin1

#———————Cavity 1—————————————————
bs CI1 $RPCI1 $TPCI1 0 0 cavin1 nrefl n11 n16
s C1s1 $L1C1 n11 n12
bs PBS $RPPBS $TPPBS 0 0 n12 n13 n21 n26
s C1s2 $L2C1 n13 n14
bs CE1 $RPCE1 $TPCE1 0 0 n14 n15 ntrans ntrans2
s C1s3 $L3C1 n15 n16




#———————Cavity 2—————————————————
s C2s1 $L1C2 n21 n22
bs CL2 $RPCL2 $TPCL2 0 0 n22 n23 lossc2 dump
s C2s2 $L2C2 n23 n24
bs CE2 $RPCE2 $TPCE2 90 0 n24 n25 dump dump
s C2s3 $L3C2 n25 n26

#Cavity tracing as parametercheck
trace 2
cav c1 CE1 n14 CE1 n15
cav c2 PBS n21 PBS n26
#cav coupled CI1 n11 CI1 n16
cav coupled2 PBS n21 PBS n12

#———————Detection———————————————
#pd1 demod2 $fmod2 0 nrefl   #30 MHz in reflection of cavity
#pd1 demod1 $fmod1 0 ntrans  #100 MHz in reflection of cavity
pd CAV1–Refl nrefl     #DC diode in reflection
#pd CAV2–Loss lossc2    #DC diode in transmission of loss mirror Cavity2
#pd CAV2–Intra n22*     #intra cavity field Cavity2
#pd CAV1–Intra n14*     #intra cavity field Cavity2

#———————Scan parameters—————————
xaxis CE1 phi lin −90 90 1000
#xaxis laser f lin −100M 300M 1000

/*
func phifollow = 0+$x1
noplot phifollow
put CE2 phi $phifollow
*/

yaxis abs

/*
x2axis PBS R lin 1 0 1000
func Tprm = 1−$x2
```

```
noplot Tprm
put PBS T $Tprm


#x2axis CE2 phi lin −90 270 1000

GNUPLOT
set pm3d #at s hidden3d 100 solid
set nosurface
unset hidden3d
set isosamples 2,2
set colorbox v
set colorbox user origin .95,.1 size .04,.8
set style line 100 lt −1 lw 0
set palette rgbformulae 7,5,15
set view 0,0
unset grid
END
*/
```

Bibliography

[1] J. Kepler. *De cometis libelli tres: I. Astronomicus... II. Physicus... III Astrologicus...* Typis Andreae Apergeri, sumptibus Sebastiani Mylii bibliopoae augustani, 1619.

[2] J. C. Maxwell. *A treatise on electricity and magnetism (2 vols)*. 1873.

[3] J. C. Maxwell. "A Dynamical Theory of the Electromagnetic Field." In: *Proceedings of the Royal Society of . . .* (1863).

[4] A. Bartoli. "Il calorico raggiante e il secondo principio di termodinamica". In: *Il Nuovo Cimento (1876-1894)* 15.1 (1876), pp. 193–202.

[5] P. Lebedew. "Untersuchungen über die Druckkräfte des Lichtes". In: *Annalen der Physik* 311.11 (1901), pp. 433–458.

[6] H. Hertz. "Über einen Einfluss des ultravioletten Lichtes auf die electrische Entladung". In: *Annalen der Physik* 267.8 (1887), pp. 983–1000.

[7] A. Einstein. "Über einen die Erzeugung und Verwandlung des Lichtes betreffenden heuristischen Gesichtspunkt". In: *Annalen der Physik* 322.6 (1905), pp. 132–148.

[8] A. H. Compton. *Secondary radiations produced by x-rays*. National Research Council of the National Academy of Sciences, 1922.

[9] A. H. Compton. "A quantum theory of the scattering of X-rays by light elements". In: *Physical review* 21.5 (1923), p. 483.

[10] T. H. Maiman. "Stimulated Optical Radiation in Ruby". In: *Nature* 187.4736 (Aug. 1960), pp. 493–494. ISSN: 0028-0836.

[11] A. Ashkin. "Acceleration and Trapping of Particles by Radiation Pressure". In: *Physical Review Letters* 24.4 (Jan. 1970), pp. 156–159. ISSN: 0031-9007.

[12] T. W. Hänsch and A. L. Schawlow. "Cooling of gases by laser radiation". In: *Optics Communications* 13.1 (Jan. 1975), pp. 68–69. ISSN: 00304018.

[13] A. Ashkin and J. M. Dziedzic. "Observation of light scattering from nonspherical particles using optical levitation." EN. In: *Applied optics* 19.5 (Mar. 1980), pp. 660–8. ISSN: 0003-6935.

[14] M. E. Gertsenshtein and V. I. Pustovoit. "On the detection of low-frequency gravitational waves". In: *Soviet Journal of Experimental and Theoretical Physics* 16 (1963), p. 433.

[15] A. Einstein. "Die Grundlage der allgemeinen Relativitätstheorie". In: *Annalen der Physik* 354.7 (1916), pp. 769–822. ISSN: 00033804.

[16] A. Einstein. "Über Gravitationswellen". In: *Sitzungsberichte der Königlich Preußischen Akademie der Wissenschaften (Berlin), Seite 154-167.* (1918).

[17] R. Weiss. "Quarterly progress report". In: *MIT Research Lab of Electronics* 105 (1972), p. 54.

[18] G. E. Moss, L. R. Miller, and R. L. Forward. "Photon-noise-limited laser transducer for gravitational antenna." EN. In: *Applied optics* 10.11 (Nov. 1971), pp. 2495–8. ISSN: 0003-6935.

[19] V. B. Braginsky, Y. I. Vorontsov, and F. Y. Khalili. *Optimal quantum measurements in detctors of gravitation radiation*. 1978.

[20] C. Caves. "Quantum-mechanical noise in an interferometer". In: *Physical Review D* 23.8 (Apr. 1981), pp. 1693–1708. ISSN: 0556-2821.

[21] M. Wallquist, K. Hammerer, P. Rabl, M. Lukin, and P. Zoller. "Hybrid quantum devices and quantum engineering". en. In: *Physica Scripta* T137.T137 (Dec. 2009), p. 014001. ISSN: 0031-8949.

[22] Y.-D. Wang and A. A. Clerk. "Using interference for high fidelity quantum state transfer in optomechanics." In: *Physical review letters* 108.15 (Apr. 2012), p. 153603. ISSN: 1079-7114.

[23] M. Aspelmeyer, T. J. Kippenberg, and F. Marquardt. "Cavity optomechanics". In: *Reviews of Modern Physics* 86.4 (Dec. 2014), pp. 1391–1452. ISSN: 0034-6861.

[24] T. P. Purdy, R. W. Peterson, and C. A. Regal. "Observation of radiation pressure shot noise on a macroscopic object." In: *Science (New York, N.Y.)* 339.6121 (Feb. 2013), pp. 801–4. ISSN: 1095-9203.

[25] A. H. Safavi-Naeini, J. Chan, J. T. Hill, T. P. M. Alegre, A. Krause, and O. Painter. "Observation of quantum motion of a nanomechanical resonator." In: *Physical review letters* 108.3 (Jan. 2012), p. 033602. ISSN: 1079-7114.

[26] J. Aasi et al. "Advanced LIGO". en. In: *Classical and Quantum Gravity* 32.7 (Apr. 2015), p. 074001. ISSN: 0264-9381.

[27] F. Acernese et al. "Advanced Virgo: a second-generation interferometric gravitational wave detector". en. In: *Classical and Quantum Gravity* 32.2 (Jan. 2015), p. 024001. ISSN: 0264-9381.

[28] W. Heisenberg. "Über den anschaulichen Inhalt der quantentheoretischen Kinematik und Mechanik". In: *Zeitschrift für Physik* 43.3-4 (Mar. 1927), pp. 172–198. ISSN: 1434-6001.

[29] D. Meschede. *Optik, Licht und Laser*. Wiesbaden: Vieweg+Teubner, 2008. ISBN: 978-3-8351-0143-2.

[30] R. Bondurant and J. Shapiro. "Squeezed states in phase-sensing interferometers". In: *Physical Review D* 30.12 (Dec. 1984), pp. 2548–2556. ISSN: 0556-2821.

[31] W. G. Unruh. *Quantum Optics, Experimental Gravity, and Measurement Theory*. Boston, MA: Springer US, 1983. Chap. Quantum no. ISBN: 978-1-4613-3714-0.

[32] H. Kimble, Y. Levin, A. Matsko, K. Thorne, and S. Vyatchanin. "Conversion of conventional gravitational-wave interferometers into quantum nondemolition interferometers by modifying their input and/or output optics". In: *Physical Review D* 65.2 (Dec. 2001), p. 022002. ISSN: 0556-2821.

[33] R. Bondurant. "Reduction of radiation-pressure-induced fluctuations in interferometric gravity-wave detectors". In: *Physical Review A* 34.5 (Nov. 1986), pp. 3927–3931. ISSN: 0556-2791.

[34] A. F. Pace, M. J. Collett, and D. F. Walls. "Quantum limits in interferometric detection of gravitational radiation". In: *Physical Review A* 47.4 (Apr. 1993), pp. 3173–3189. ISSN: 1050-2947.

[35] T. Briant, M. Cerdonio, L. Conti, A. Heidmann, A. E. Lobo, and M. Pinard. "Optimal generalization of power filters for gravitational wave bursts from single to multiple detectors". In: *Physical Review D* 68.10 (Nov. 2003), p. 102005. ISSN: 0556-2821.

[36] T. Caniard, P. Verlot, T. Briant, P.-F. Cohadon, and A. Heidmann. "Observation of Back-Action Noise Cancellation in Interferometric and Weak Force Measurements". In: *Physical Review Letters* 99.11 (Sept. 2007), p. 110801. ISSN: 0031-9007.

[37] Y. Chen, S. L. Danilishin, F. Y. Khalili, and H. Müller-Ebhardt. "QND measurements for future gravitational-wave detectors". In: *General Relativity and Gravitation* 43.2 (Aug. 2010), pp. 671–694. ISSN: 0001-7701.

[38] V. B. Braginsky and F. J. Khalili. "Gravitational wave antenna with QND speed meter". In: *Physics Letters A* 147.5-6 (July 1990), pp. 251–256. ISSN: 03759601.

[39] S. L. Danilishin, C. Gräf, S. S. Leavey, J. Hennig, E. A. Houston, D. Pascucci, S. Steinlechner, J. Wright, and S. Hild. "Quantum noise of non-ideal Sagnac speed meter interferometer with asymmetries". en. In: *New Journal of Physics* 17.4 (Apr. 2015), p. 043031. ISSN: 1367-2630.

[40] S. Chelkowski, H. Vahlbruch, B. Hage, A. Franzen, N. Lastzka, K. Danzmann, and R. Schnabel. "Experimental characterization of frequency-dependent squeezed light". In: *Physical Review A* 71.1 (Jan. 2005), p. 013806. ISSN: 1050-2947.

[41] C. Mow-Lowry, B. Sheard, M. Gray, D. McClelland, and S. Whitcomb. "Experimental Demonstration of a Classical Analog to Quantum Noise Cancellation for Use in Gravitational Wave Detection". In: *Physical Review Letters* 92.16 (Apr. 2004), p. 161102. ISSN: 0031-9007.

[42] B. Sheard, M. Gray, C. Mow-Lowry, D. McClelland, and S. Whitcomb. "Observation and characterization of an optical spring". In: *Physical Review A* 69.5 (May 2004), p. 051801. ISSN: 1050-2947.

[43] M. Tsang and C. Caves. "Coherent Quantum-Noise Cancellation for Optomechanical Sensors". In: *Physical Review Letters* 105.12 (Sept. 2010). ISSN: 0031-9007.

[44] B. Julsgaard, A. Kozhekin, and E. S. Polzik. "Experimental long-lived entanglement of two macroscopic objects." In: *Nature* 413.6854 (Sept. 2001), pp. 400–3. ISSN: 0028-0836.

[45] K. Hammerer, M. Aspelmeyer, E. Polzik, and P. Zoller. "Establishing Einstein-Poldosky-Rosen Channels between Nanomechanics and Atomic Ensembles". In: *Physical Review Letters* 102.2 (Jan. 2009). ISSN: 0031-9007.

[46] W. Wasilewski, K. Jensen, H. Krauter, J. J. Renema, M. V. Balabas, and E. S. Polzik. "Quantum Noise Limited and Entanglement-Assisted Magnetometry". In: *Physical Review Letters* 104.13 (Mar. 2010). ISSN: 0031-9007.

[47] M. K. E. L. Planck. "Zur theorie des Gesetzes der Energieverteilung im Normalspektrum". In: *Verhandl. Dtsc. Phys. Ges.* 2 (1900), p. 237.

[48] A. Einstein. "Zur Quantentheorie der Strahlung". In: *Physikalische Zeitschrift* 18 (1917).

[49] R. J. Glauber. "Coherent and Incoherent States of the Radiation Field". In: *Physical Review* 131.6 (Sept. 1963), pp. 2766–2788. ISSN: 0031-899X.

[50] C. Gardiner and P. Zoller. *Quantum Noise: A Handbook of Markovian and Non-Markovian Quantum Stochastic Methods with Applications to Quantum Optics (Springer Series in Synergetics)*. Springer, 2004. ISBN: 3540223010.

[51] C. Gerry and P. Knight. *Introductory Quantum Optics*. Cambridge University Press, 2005, p. 317. ISBN: 052152735X.

[52] L. Landau and E. Lifshitz. *Course of Theoretical Physics: Vol.: 3: Quantum Mechanis: Non-Relativistic Theory*. Pergamon Press, 1965.

[53] W. Nolting. *Grundkurs Theoretische Physik 5/1*. Springer-Lehrbuch. Berlin, Heidelberg: Springer Berlin Heidelberg, 2013. ISBN: 978-3-642-25402-4.

[54] D. F. Walls. "Squeezed states of light". In: *Nature* 306.5939 (Nov. 1983), pp. 141–146. ISSN: 0028-0836.

[55] R. W. Boyd. *Nonlinear Optics*. Academic Press London, 2008. ISBN: 0080485960.

[56] V. G. Dmitriev, G. G. Gurzadyan, D. N. Nikogosyan, and H. K. V. Lotsch. *Handbook of Nonlinear Optical Crystals*. Vol. 64. Springer Series in Optical Sciences. Berlin, Heidelberg: Springer Berlin Heidelberg, 1999. ISBN: 978-3-642-08472-0.

[57] M. Mehmet, S. Ast, T. Eberle, S. Steinlechner, H. Vahlbruch, and R. Schnabel. "Squeezed light at 1550 nm with a quantum noise reduction of 12.3 dB." EN. In: *Optics express* 19.25 (Dec. 2011), pp. 25763–72. ISSN: 1094-4087.

[58] H.-A. Bachor and T. C. Ralph. "A Guide to Experiments in Quantum Optics, 2nd". In: *A Guide to Experiments in Quantum Optics, 2nd, Revised and Enlarged Edition, by Hans-A. Bachor, Timothy C. Ralph, pp. 434. ISBN 3-527-40393-0. Wiley-VCH, March 2004.* (2004), p. 434.

[59] B. Yurke. "Use of cavities in squeezed-state generation". In: *Physical Review A* 29.1 (Jan. 1984), pp. 408–410. ISSN: 0556-2791.

[60] H. Yuen and J. Shapiro. "Optical communication with two-photon coherent states–Part III: Quantum measurements realizable with photoemissive detectors". In: *IEEE Transactions on Information Theory* 26.1 (Jan. 1980), pp. 78–92. ISSN: 0018-9448.

[61] A. Siegman. *Lasers*. Mill Valley Calif.: University Science Books, 1986. ISBN: 9780935702118.

[62] P. K. Lam, T. C. Ralph, B. C. Buchler, D. E. McClelland, H.-A. Bachor, and J. Gao. "Optimization and transfer of vacuum squeezing from an optical parametric oscillator". en. In: *Journal of Optics B: Quantum and Semiclassical Optics* 1.4 (Aug. 1999), pp. 469–474. ISSN: 1464-4266.

[63] A. Freise and K. A. Strain. "Interferometer Techniques for Gravitational-Wave Detection". In: *Living Reviews in Relativity* 13 (2010). ISSN: 1433-8351.

[64] J. Mizuno, K. Strain, P. Nelson, J. Chen, R. Schilling, A. Rüdiger, W. Winkler, and K. Danzmann. "Resonant sideband extraction: a new configuration for interferometric gravitational wave detectors". In: *Physics Letters A* 175.5 (Apr. 1993), pp. 273–276. ISSN: 03759601.

[65] A. Thüring, R. Schnabel, H. Lück, and K. Danzmann. "Detuned Twin-Signal-Recycling for ultrahigh-precision interferometers". EN. In: *Optics Letters* 32.8 (Mar. 2007), p. 985. ISSN: 0146-9592.

[66] F. Khalili. "Reducing the mirrors coating noise in laser gravitational-wave antennae by means of double mirrors". In: *Physics Letters A* 334.1 (Jan. 2005), pp. 67–72. ISSN: 03759601.

[67] J. Mizuno. "Comparison of optical configurations for laser-interferometric gravitational-wave detectors". Phd-Thesis. Garching: Max-Planck-Institut für Quantenoptik, 1995.

[68] A. Thüring. "Investigations of coupled and Kerr non-linear optical resonators". PhD thesis. Leibniz Universität Hannover, 2009.

[69] B. Little, S. Chu, H. Haus, J. Foresi, and J.-P. Laine. "Microring resonator channel dropping filters". In: *Journal of Lightwave Technology* 15.6 (June 1997), pp. 998–1005. ISSN: 07338724.

[70] B. Little, T. Kaneko, and Y. Kokubun. "Cascaded microring resonators for crosstalk reduction and spectrum cleanup in add-drop filters". In: *IEEE Photonics Technology Letters* 11.11 (Nov. 1999), pp. 1423–1425. ISSN: 1041-1135.

[71] A. Freise. *Finesse (Frequency domain INterfErometer Simulation SoftwarE)*. 2009.

[72] T. J. Kippenberg and K. J. Vahala. "Cavity optomechanics: backaction at the mesoscale." en. In: *Science (New York, N.Y.)* 321.5893 (Aug. 2008), pp. 1172–6. ISSN: 1095-9203.

[73] A. H. Safavi-Naeini, S. Gröblacher, J. T. Hill, J. Chan, M. Aspelmeyer, and O. Painter. "Squeezed light from a silicon micromechanical resonator." en. In: *Nature* 500.7461 (Aug. 2013), pp. 185–9. ISSN: 1476-4687.

[74] T. Czerniuk, C. Brüggemann, J. Tepper, S. Brodbeck, C. Schneider, M. Kamp, S. Höfling, B. A. Glavin, D. R. Yakovlev, A. V. Akimov, and M. Bayer. "Lasing from active optomechanical resonators." en. In: *Nature communications* 5 (Jan. 2014), p. 4038. ISSN: 2041-1723.

[75] R. Schnabel. "Einstein-Podolsky-Rosen-entangled motion of two massive objects". In: *Physical Review A* 92.1 (July 2015), p. 012126. ISSN: 1050-2947.

[76] M. H. Wimmer, D. Steinmeyer, K. Hammerer, and M. Heurs. "Coherent cancellation of backaction noise in optomechanical force measurements". In: *Physical Review A* 89.5 (May 2014), p. 053836. ISSN: 1050-2947.

[77] D. Steinmeyer. "Towards coherent noise cancellation". Master Thesis. Leibniz Universität Hannover, 2014.

[78] W. H. Louisell, A. Yariv, and A. E. Siegman. "Quantum Fluctuations and Noise in Parametric Processes. I." In: *Physical Review* 124.6 (Dec. 1961), pp. 1646–1654. ISSN: 0031-899X.

[79] R. L. Byer. *Nonlinear Infrared Generation*. Vol. 16. Topics in Applied Physics. Berlin, Heidelberg: Springer Berlin Heidelberg, 1977. ISBN: 978-3-540-07945-3.

[80]   Y. Yu and H. Wang. "Two-color continuous-variable entangle-
        ment generated in nondegenerate optical parametric oscillator".
        In: *Optics Communications* 285.8 (Apr. 2012), pp. 2223–2226. ISSN:
        00304018.

[81]   A. Samblowski, C. Laukötter, N. Grosse, P. Lam, and R. Schn-
        abel. "Two Color Entanglement". In: *American Institute of Physics
        Conference Series*. Ed. by T. Ralph and P. Lam. Vol. 1363. Amer-
        ican Institute of Physics Conference Series. 2011, pp. 219–222.
        arXiv: 1011.5766 [quant-ph].

[82]   L. Bakemeier, A. Alvermann, and H. Fehske. "Route to chaos in
        optomechanics". In: *Physical Review Letters* 114.1 (2015), pp. 1–5.
        ISSN: 10797114. arXiv: 1407.5529.

[83]   H. Vahlbruch, A. Khalaidovski, N. Lastzka, C. Gräf, K. Danz-
        mann, and R. Schnabel. "The GEO 600 squeezed light source".
        en. In: *Classical and Quantum Gravity* 27.8 (Apr. 2010), p. 084027.
        ISSN: 0264-9381.

[84]   J. Aasi et al. "Enhanced sensitivity of the LIGO gravitational
        wave detector by using squeezed states of light". In: *Nature Pho-
        tonics* 7.8 (July 2013), pp. 613–619. ISSN: 1749-4885.

[85]   H. Kogelnik and T. Li. "Laser Beams and Resonators". In: *Pro-
        ceedings of the IEEE* 54.10 (1966), pp. 1312–1329. ISSN: 15582256.

[86]   T. Meier. "C++ Program". In: *Personal Communication* (2010).

[87]   H. Vahlbruch. "Temperature controller V10". In: *Personal Com-
        munication* (2011).

[88]   D. N. Nikogosyan. *Nonlinear Optical Crystals: A Complete Survey*.
        New York: Springer-Verlag, 2005. ISBN: 0-387-22022-4.

[89]   P. Günter. "Near-infrared noncritically phase-matched second-
        harmonic generation in KNbO3". In: *Applied Physics Letters* 34.10
        (Aug. 1979), p. 650. ISSN: 00036951.

[90]   K. Kato and E. Takaoka. "Sellmeier and thermo-optic disper-
        sion formulas for KTP". EN. In: *Applied Optics* 41.24 (Aug. 2002),
        p. 5040. ISSN: 0003-6935.

[91]   S. Emanueli and A. Arie. "Temperature-Dependent Dispersion
        Equations for KTiOPO4 and KTiOAsO4". EN. In: *Applied Optics*
        42.33 (Nov. 2003), p. 6661. ISSN: 0003-6935.

[92]   R. Bloomer, M. Pysher, and O. Pfister. "Nonlocal restoration of two-mode squeezing in the presence of strong optical loss". en. In: *New Journal of Physics* 13.6 (June 2011), p. 063014. ISSN: 1367-2630.

[93]   B. Willke, N. Uehara, E. K. Gustafson, R. L. Byer, P. J. King, S. U. Seel, and R. L. Savage. "Spatial and temporal filtering of a 10-W Nd:YAG laser with a Fabry-Perot ring-cavity premode cleaner". EN. In: *Optics Letters* 23.21 (Nov. 1998), p. 1704. ISSN: 0146-9592.

[94]   M. Heurs, I. R. Petersen, M. R. James, and E. H. Huntington. "Homodyne locking of a squeezer". EN. In: *Optics Letters* 34.16 (Aug. 2009), p. 2465. ISSN: 0146-9592.

[95]   R. W. P. Drever, J. L. Hall, F. V. Kowalski, J. Hough, G. M. Ford, A. J. Munley, and H. Ward. "Laser phase and frequency stabilization using an optical resonator". In: *Applied Physics B Photophysics and Laser Chemistry* 31.2 (June 1983), pp. 97–105. ISSN: 0721-7269.

[96]   Innolight. "Mephisto s". In: *Datasheet* (2014).

[97]   M. Mehmet. "High bandwidth diode". In: *Personal Communication* (2015).

[98]   S. Ast. "New approaches in squeezed light generation - Quantum states of light with GHz squeezing bandwidth and squeezed light generation via the cascaded Kerr effect". PhD thesis. Leibniz Universität Hannover, 2015.

[99]   F. Herzog, K. Kudielka, D. Erni, and W. Bachtold. "Optical Phase Locking by Local Oscillator Phase Dithering". English. In: *IEEE Journal of Quantum Electronics* 42.10 (Oct. 2006), pp. 973–985. ISSN: 0018-9197.

[100] P. R. Saulson. *Fundamentals of interferometric gravitational wave detectors*. World scientific, 1994.

[101] T. A. Driscoll, P. E. Perkins, H. J. Hoffman, and R. E. Stone. "Efficient second-harmonic generation in KTP crystals". EN. In: *Journal of the Optical Society of America B* 3.5 (May 1986), p. 683. ISSN: 0740-3224.

[102] Fermionics. "Highspeed InGaAs Photodiode". In: *Datasheet FD70* ().

[103] A. Staley, D. Martynov, R. Abbott, R. X. Adhikari, K. Arai, S. Ballmer, L. Barsotti, A. F. Brooks, R. T. DeRosa, S. Dwyer, A. Effler, M. Evans, P. Fritschel, V. V. Frolov, C. Gray, C. J. Guido, R. Gustafson, M. Heintze, D. Hoak, K. Izumi, K. Kawabe, E. J. King, J. S. Kissel, K. Kokeyama, M. Landry, D. E. McClelland, J. Miller, A. Mullavey, B. O'Reilly, J. G. Rollins, J. R. Sanders, R. M. S. Schofield, D. Sigg, B. J. J. Slagmolen, N. D. Smith-Lefebvre, G. Vajente, R. L. Ward, and C. Wipf. "Achieving resonance in the Advanced LIGO gravitational-wave interferometer". en. In: *Classical and Quantum Gravity* 31.24 (Dec. 2014), p. 245010. ISSN: 0264-9381.

Acknowledgements

First of all, I want to thank Prof. Dr. Karsten Danzmann for this great institute, it is a unique place with its scientific and always friendly environment.

I want to thank Prof. Dr. Michèle Heurs for her confidence to take this adventure with a a new group and me being a part of it. Without her guidance and help this work would not be as it is now. I am glad to have had such a dedicated advisor.

Almost none of my research was achieved alone. I want to thank Prof. Dr. Klemens Hammerer for the fruitful theoretical discussions. Henning and Moritz for their experimental expertise and help in the lab. Andreas Weidner for his patience with my electronic circuits and Phillip Schauzu for his ideas and mechanical designs. Also thanks to all the other colleagues at the institute for their help.

For proofreading my thesis I want to thank Kai, Daniel, Klemens, Moritz and Timo.

Great thanks to the colleagues of the quantum control group Daniel, Bernd, Kai and espacially my office mates Timo and Dirk, I will never forget these awesome years I had with you.

Finally I want to thank my family for their loving support and encouragement over the past years.

Very special thanks to Carolin, Emil and Greta. I love you.

Curriculum vitae

Personal data

Name:	Maximilian Wimmer
Address:	Kollenrodtstraße 4, 30161 Hannover
Nationality:	German
Date of birth:	28.05.1985
Place of birth:	Essen
Family status:	Married & 2 children

Academic career

10/2010 – 06/2016	PhD Thesis at Leibniz-Universität Hannover
	Institute for gravitational physics
	AG Heurs - Quantum Control
	Coupled nonclassical systems for
	coherent backaction noise cancellation
10/2004 – 07/2010	Diploma studies at Leibniz-Universität Hannover
	Diploma thesis Institute for Gravititonal Physics
	AG Schnabel- (All reflective interferometry)
	Interferometrie mit gittergekoppelten Armresonatoren
10/2008 – 04/2009	Erasmus Semester, Universidade de Lisboa

Education

06/1997 – 06/2004	Gymnasium Munster
06/1995 – 06/1997	Orientierungsstufe Munster
06/1991 – 06/1995	Grundschule Breloh

List of publications

2016

1. Aasi, J., . . . , **M. H. Wimmer**, . . . , et al.. Search of the Orion spur for continuous gravitational waves using a loosely coherent algorithm on data from LIGO interferometers. *Phys. Rev.*, **D93**(4),042006.

2. Abbott B. P., . . . , **M. H. Wimmer**, . . . , et al.. All-sky search for long duration gravitational wave transients with initial LIGO. *Phys. Rev.*, **D93**(4),042005.

3. Abbott B. P., . . . , **M. H. Wimmer**, . . . , et al.. Observation of Gravitational Waves from a Binary Black Hole Merger. *Phys. Rev. Lett.*, **116**(6),061102.

4. Abbott B. P., . . . , **M. H. Wimmer**, . . . , et al.. Astrophysical Implications of the Binary Black-Hole Merger GW150914. *Astrophys. J.*, **818**(2),L22.

5. Abbott B. P., . . . , **M. H. Wimmer**, . . . , et al.. Localization and broadband follow-up of the gravitational-wave transient GW150914. *eprint arXiv:*, 1602.08492, (astro-ph.HE).

6. Abbott B. P., . . . , **M. H. Wimmer**, . . . , et al.. GW150914: Implications for the stochastic gravitational wave background from binary black holes. *eprint arXiv:*, 1602.03847, (gr-qc).

7. Abbott B. P., ..., **M. H. Wimmer**, ..., et al.. Calibration of the Advanced LIGO detectors for the discovery of the binary black-hole merger GW150914. *eprint arXiv:*, 1602.03845, (gr-qc).

8. Abbott B. P., ..., **M. H. Wimmer**, ..., et al.. Characterization of transient noise in Advanced LIGO relevant to gravitational wave signal GW150914. *eprint arXiv:*, 1602.03844, (gr-qc).

9. Abbott B. P., ..., **M. H. Wimmer**, ..., et al.. Observing gravitational-wave transient GW150914 with minimal assumptions. *eprint arXiv:*, 1602.03843, (gr-qc).

10. Abbott B. P., ..., **M. H. Wimmer**, ..., et al.. The Rate of Binary Black Hole Mergers Inferred from Advanced LIGO Observations Surrounding GW150914. *eprint arXiv:*, 1602.03842, (astro-ph.HE).

11. Abbott B. P., ..., **M. H. Wimmer**, ..., et al.. Tests of general relativity with GW150914. *eprint arXiv:*, 1602.03841, (gr-qc).

12. Abbott B. P., ..., **M. H. Wimmer**, ..., et al.. Properties of the binary black hole merger GW150914. *eprint arXiv:*, 1602.03840, (gr-qc).

13. Abbott B. P., ..., **M. H. Wimmer**, ..., et al.. GW150914: First results from the search for binary black hole coalescence with Advanced LIGO. *eprint arXiv:*, 1602.03839, (gr-qc).

14. Abbott B. P., ..., **M. H. Wimmer**, ..., et al.. GW150914: The Advanced LIGO Detectors in the Era of First Discoveries. *eprint arXiv:*, 1602.03838, (gr-qc).

15. Adrian-Martinez, S., ..., **M. H. Wimmer**, ..., et al.. High-energy Neutrino follow-up search of Gravitational Wave Event GW150914 with ANTARES and IceCube. *eprint arXiv:*, 1602.05411, (astro-ph.HE).

16. Aasi, J., ..., **M. H. Wimmer**, ..., et al.. First low frequency all-sky search for continuous gravitational wave signals. *Phys. Rev.*, **D93**(4),042007.

2015

1. T. Denker, D. Schütte, **M. H. Wimmer**, T. A. Wheatley, E. H. Huntington, and M. Heurs. Utilizing weak pump depletion to stabilize squeezed vacuum states. *Opt. Express*, **23**(13),16517.

2. Aasi, J., ..., **M. H. Wimmer**, ..., et al.. Advanced LIGO. *Class. Quant. Grav.*, **32**,074001.

3. Aasi, J., ..., **M. H. Wimmer**, ..., et al.. Directed search for gravitational waves from Scorpius X-1 with initial LIGO data. *Phys. Rev.*, **D91**(6),062008.

4. Aasi, J., ..., **M. H. Wimmer**, ..., et al.. Characterization of the LIGO detectors during their sixth science run. *Class. Quant. Grav.*, **32**(11),115012.

5. Aasi, J., ..., **M. H. Wimmer**, ..., et al.. Searches for continuous gravitational waves from nine young supernova remnants. *Astrophys J.*, **813**(1),39.

6. Aasi, J., ..., **M. H. Wimmer**, ..., et al.. Narrow-band search of continuous gravitational-wave signals from Crab and Vela pulsars in Virgo VSR4 data. *Phys. Rev.*, **D91**(2),022004.

7. Aasi, J., ..., **M. H. Wimmer**, ..., et al.. Searching for stochastic gravitational waves using data from the two colocated LIGO Hanford detectors. *Phys. Rev.*, **D91**(2),022003.

2014

1. **M. H. Wimmer**, D. Steinmeyer, K. Hammerer and M. Heurs. Coherent Cancellation of Backaction Noise in optomechanical Force Measurements. *Phys. Rev.*, **A89**(5),053836.

2. Aartsen, M. G., ..., **M. H. Wimmer**, ..., et al.. Multimessenger search for sources of gravitational waves and high-energy neu-

trinos: Initial results for LIGO-Virgo and IceCube. *Phys. Rev.*, **D90**(10),102002.

3. Aasi, J., ..., **M. H. Wimmer**, ..., et al.. Application of a Hough search for continuous gravitational waves on data from the fifth LIGO science run. *Class. Quant. Grav.*, **31**,085014.

4. Aasi, J., ..., **M. H. Wimmer**, ..., et al.. Gravitational waves from known pulsars: results from the initial detector era. *Astrophys. J.*, **785**,119.

5. Aasi, J., ..., **M. H. Wimmer**, ..., et al.. First Searches for Optical Counterparts to Gravitational-wave Candidate Events. *Astrophys. J. Suppl.*, **211**,7.

6. Aasi, J., ..., **M. H. Wimmer**, ..., et al.. Constraints on cosmic strings from the LIGO-Virgo gravitational-wave detectors. *Phys. Rev. Lett.*, **122**,131101.

7. Aasi, J., ..., **M. H. Wimmer**, ..., et al.. Search for gravitational wave ringdowns from perturbed intermediate mass black holes in LIGO-Virgo data from 2005-2010. *Phys. Rev.*, **D89**(10),102006.

8. Aasi, J., ..., **M. H. Wimmer**, ..., et al.. Methods and results of a search for gravitational waves associated with gamma-ray bursts using the GEO600, LIGO, and Virgo detectors. *Phys. Rev.*, **D89**(12),122004.

9. Aasi, J., ..., **M. H. Wimmer**, ..., et al.. First all-sky search for continuous gravitational waves from unknown sources in binary systems. *Phys. Rev.*, **D90**(6),062010.

10. Aasi, J., ..., **M. H. Wimmer**, ..., et al.. Search for gravitational waves associated with γ-ray bursts detected by the Interplanetary Network. *Phys. Rev. Lett.*, **113**(1),011102.

11. Aasi, J., ..., **M. H. Wimmer**, ..., et al.. Search for gravitational radiation from intermediate mass black hole binaries in data from the second LIGO-Virgo joint science run. *Phys. Rev.*, **D89**(12),122003.

12. Aasi, J., . . . , **M. H. Wimmer**, . . . , et al.. Implementation of an *F*-statistic all-sky search for continuous gravitational waves in Virgo VSR1 data. *Class. Quant. Grav.*, **31**,165014.

13. Aasi, J., . . . , **M. H. Wimmer**, . . . , et al.. The NINJA-2 project: Detecting and characterizing gravitational waveforms modelled using numerical binary black hole simulations. *Class. Quant. Grav.*, **31**,115004.

14. Aasi, J., . . . , **M. H. Wimmer**, . . . , et al.. Improved Upper Limits on the Stochastic Gravitational-Wave Background from 2009-2010 LIGO and Virgo Data. *Phys. Rev. Lett.*, **113**(23),231101.

15. Acernese F., . . . , **M. H. Wimmer**, . . . , et al.. Concepts and research for future detectors. *Gen. Rel. Grav.*, **46**(5),1700.

2013

1. Aasi, J., . . . , **M. H. Wimmer**, . . . , et al.. Directed search for continuous gravitational waves from the Galactic center. *Phys. Rev.*, **D88**(10),102002.

2. Aasi, J., . . . , **M. H. Wimmer**, . . . , et al.. Search for long-lived gravitational-wave transients coincident with long gamma-ray bursts. *Phys. Rev.*, **D88**(12),122004.

3. Aasi, J., . . . , **M. H. Wimmer**, . . . , et al.. Prospects for Observing and Localizing Gravitational-Wave Transients with Advanced LIGO and Advanced Virgo. *eprint arXiv:*, 1304.0670, (gr-qc).

4. Aasi, J., . . . , **M. H. Wimmer**, . . . , et al.. Enhanced sensitivity of the LIGO gravitational wave detector by using squeezed states of light. *Nature Photon.*, 7, 613-619.

5. Aasi, J., . . . , **M. H. Wimmer**, . . . , et al.. Parameter estimation for compact binary coalescence signals with the first generation gravitational-wave detector network. *Phys. Rev.*, **D88**(6),062001.

6. Adrìan-Martìnez, S. ..., **M. H. Wimmer**, ..., et al.. A first search for coincident gravitational waves and high energy neutrinos using LIGO, Virgo and ANTARES data from 2007. *Journal of Cosmology and Astropart. phys.*, **6**1-39.

7. Aasi, J., ..., **M. H. Wimmer**, ..., et al.. Einstein@Home all-sky search for periodic gravitational waves in LIGO S5 data. *Phys. Rev.*, **D87**(4),042001.

8. Aasi, J., ..., **M. H. Wimmer**, ..., et al.. Search for gravitational waves from binary black hole inspiral, merger, and ringdown in LIGO-Virgo data from 2009-2010. *Phys. Rev.*, **D87**(2),022002.

2012

1. M. Britzger, **M. H. Wimmer**, A. Khaleidovski, D. Friedrich, S. Kroker, F. Brückner, E.B. Kley, A. Tünnermann, K. Danzmann, R. Schnabel. Michelson interferometer with diffractively-coupled arm resonators in second-order Littrow configuration. *Optics Express* **20**(23),25400-25408

2. Evans, P. A., ..., **M. H. Wimmer**, ..., et al.. Swift follow-up observations of candidate gravitational-wave transient events. *Astrophys. Journ.*, **203**(2),28.

3. Aasi, J., ..., **M. H. Wimmer**, ..., et al.. The characterization of Virgo data and its impact on gravitational-wave searches. *Class. and Quant. Gravity*, **29**(15),155002.